FEDERAL UNIVERSITY OF ITAJUBÁ - UNIFEI
POSTGRADUATE PROGRAM IN
MATERIALS SCIENCE AND ENGINEERING

Preparation and Characterization of thermoelectric materials.

João Ider Silva Júnior

Itajubá, July 22, 2022

FEDERAL UNIVERSITY OF ITAJUBÁ - UNIFEI
POSTGRADUATE PROGRAM IN
MATERIALS SCIENCE AND ENGINEERING

João Ider Silva Júnior

Preparation and Characterization of thermoelectric materials.

Thesis presented for obtaining a PhD degree in the Postgraduate Program in Materials Science and Engineering of the Federal University of Itajubá

Concentration Area: Non-Metals

Supervisor: Rero Marques Rubinger
Co-supervisor: Adhimar Flavio Oliveira

July 22, 2022
Itajubá

FEDERAL UNIVERSITY OF ITAJUBÁ - UNIFEI
POSTGRADUATE PROGRAM IN
MATERIALS SCIENCE AND ENGINEERING

Preparation and Characterization of thermoelectric materials.

João Ider Silva Júnior

Dissertation approved by the examining board in July 22, 2022, granting the author the title of **Doctor of Materials Science and Engineering.**

Examination Board:
Prof. Dr. Alan Bendasoli Pavan (UNIFEI)
Prof. Dr. Antônio Carlos Ancelotti Júnior (UNIFEI)
Prof. Dr. Vander Alkmin dos Santos Ribeiro (FEPI)
Prof. Dr. Wagner Souza Machado (UFSJ)

Itajubá
2022

João Ider Silva Júnior

Preparation and Characterization of thermoelectric materials

Thesis presented for obtaining a PhD degree in the Post-graduate Program in Materials Science and Engineering of the Federal University of Itajubá

Approved Work. Itajubá, July 22, 2022:

Prof. Dr. Rero Marques Rubinger
Supervisor

Prof. Dr. Adhimar Flavio Oliveira
Co-supervisor

**Prof. Dr. Alan Bendasoli Pavan
(UNIFEI)**

**Prof. Dr. Antônio Carlos Ancelotti
Júnior (UNIFEI)**

**Prof. Dr. Vander Alkmin dos Santos
Ribeiro (FEPI)**

**Prof. Dr. Wagner Souza Machado
(UFSJ)**

Itajubá

July 22, 2022

Acknowledgments

"The heavens declare the glory of God; and the firmament sheweth his handywork."

(Psalm 19:1)

Abstract

This work presents a complete study of thermoelectric materials. It starts with a study of a Solar Concentrator and the development of a Genetic Algorithm and Cross-Entropy for analyzing experimental data. Contains a study on thermoelectric devices, from a new experimental setup. It also counts on the development and manufacture of an entire equipment for measuring thermoelectric materials, both bulks and thin films. It ends with the preparation of a specific thermoelectric material, the MoS_2, and the use of all the apparatus previously developed for its study.

Key-words: Self-adaptative Differential Evolution. Thermoelectric Materials. Figure of Merit. Thermoelectric device characterization.

List of Figures

List of Tables

List of abbreviations and acronyms

List of symbols

Contents

1 Introduction

Science has a increasingly multidisciplinary. The need to act on several fronts to study phenomenon of nature is increasing. This is necessary to the study in of condensed matter physics, sub-field semiconductors and particular thermoelectric materials.

Complete analysis of materials requires the preparation of the sample with the choice of process for this, that involves both Physics and Chemistry. This process takes place with the use of some equipment, that involves engineering. After the construction of the equipment, the choice of the process, and the preparation of the sample, comes the measurements and obtaining data. Data analysis requires Mathematics and Computation, and, in our case, an algorithm that mimics Biology. All these elements were brought together to carry out this work to develop knowledge of thermoelectric materials.

Thermoelectric materials belong to a topic of great importance and have many applications. As a result, in this work, we propose to carry out a complete study of them. This study involves the development of a computational tool, an evolutionary algorithm, which aims to analyze the experimental data. An experimental apparatus was also made for the analysis of thermoelectric generating devices, the TEG (*Thermoelectric Generator*). After that, entire equipment was developed for the thermoelectric characterization of materials, in bulk or thin films, and software for control.

Other equipment work was also be carried out, with the adaptation of an oven for sample preparation, both bulk and thin films. And, finally, the preparation and characterization of a thermoelectric material. We initially worked with the Molybdenum disulfide, MoS_2, powder for pellet production. And, even further, the growth of thin films from MoS_2.

These subjects were developed in separate works, thus showing the versatility and effectiveness of the developed methods, and presented in separate chapters. The first work carried out was using the developed computational tool.

Starting with the computational tool, we have the GA (*Genetic Algorithm*). They are a particular type of evolutionary algorithms that use approaches derived from evolutionary biologies such as heredity, mutation, natural selection, and recombination. They are inspired by the Darwinian principle of the evolution of species and by [1] genetics. They are probabilistic algorithms that provide a parallel and adaptive search engine based on the principle of survival of the fittest and reproduction.

The principles of nature that GA are inspired by are simple. According to Charles Darwin's theory, the principle of selection favors the fittest individuals with the longest

life and, therefore, with the greatest probability of reproduction. Individuals with more descendants are more likely to perpetuate their genetic codes in future generations. Such genetic codes constitute the identity of each individual and are represented on chromosomes.

These principles are imitated in the construction of computational algorithms that seek a better solution for a given problem, through the evolution of populations of solutions encoded through artificial chromosomes.

They are like a computer simulation where a fixed amount of possible solutions, called a population, is evolved in search of better, more adapted solutions. This evolution starts from a randomly created population and goes through several mutations, or processes, through its generations. At each new generation, the new set of solutions is evaluated, and its adaptation to the environment is verified (in this case, the adaptation to some previously established mathematical criterion, called an objective function). The most adapted ones are then selected for the next generation, recombined, mutated, and form a new population. This new population is then used as input for the next iteration of the algorithm so that the evolution, the process, continues.

The meta-heuristic method called DE (*Differential Evolution*) was proposed by Storn and Price [2]. Initially, the DE algorithm was applied to solve systems of continuous variables [2] and soon proved to be efficient for a wide range of problems [3, 4, 5, 6]. Later, it was updated to, no longer depend on control parameters, becaming self-adaptive [7], receiving the name of SADE (*Self-Adaptative Differential Algorithm*). With this procedure, it is possible to find the global minimum of multimodal nonlinear functions in a light and efficient way that is popularly used to solve engineering problems [8].

This method was used to obtain the best fitting parameters of experiments described in the Chapters 2 and 4 showing their great efficiency and robustness, being able to be applied to different problems, and will be applied to the works carried out in the Chapter 5. Another work was also carried out using this algorithm, which is presented in Annex B.

This very powerful algorithm will be used to study semiconductors. We will study semiconductors with interesting thermoelectric properties. The thermoelectric effect is the direct conversion of temperature gradient into electrical voltage and vice versa. The potential differences related to temperature gradient between the extremes of the material are what characterizes the thermoelectric effect [10, 11]. Thus, these can be used to generate energy and recover waste heat, and as coolers or heaters [12, 13]. However, due to their low efficiency, the applicability of thermoelectric devices has been limited [12, 13, 14, 15, 16].

Generally speaking, these devices are used in applications where reliability and

robustness are more important than efficiency, such as satellites and space probes (on Voyager 1/2 and the Mars Curiosity rover, for example) and in oil and gas pipelines (to power monitoring and control systems). Other occasions in which thermoelectric devices are preferred are in situations where portability or size or shape are limiting factors. For example, in the cooling of small regions in integrated circuits, in mini-refrigerators for domestic use (for bottles or beverage cans), or the thermal control of seats in some car models.

Despite being known for almost two centuries (the Seebeck effect was discovered in 1823), not much is known about the thermoelectric properties of new materials. One of the obvious reasons for this is that they did not exist until recently. Another is that only recently have the means (computational capacity) been available to perform the necessary calculations to study the thermoelectric properties of these new materials [14] and even experimental techniques to measure thermoelectric effects in some types of nanostructures, such as molecular junctions, in which the first measurement was made only in 2007 [17].

The basic principles of thermoelectric devices have not changed much since the 1960s with the use of bismuth telluride and its alloys. Since that time, there have been significant advances in materials for use in a thermoelectric generation, but at all temperatures, energy conversion efficiency falls far short of an ideal thermodynamic machine.

The use of semiconductors as thermoelectric materials was responsible for the reinvigoration of research in thermoelectricity in the 1950s. This is directly linked to the investigations of Goldsmid [18] and Ioffe [19] who consider both thermodynamics approaches as solid-state. They extended previous development into the microscopic area and opened the door to materials and applications engineering. Ioffe introduced the figure of merit as the primary parameter, which brings together the different transport, enabling an efficient way to classify the various thermoelectric materials

In 1821, the German physicist Thomas Johann Seebeck was the first to discover the effect that bears his name. Seebeck observed that a compass needle was deflected from its position when it was placed in the vicinity of a closed circuit, where the circuit was simply formed by a link of two different metals whose junctions were held at different temperatures. Initially, Seebeck believed that the temperature difference induced magnetism in the materials, but he soon realized that it was the thermoelectric force that generated an electric current that, under Ampère's law, deflected the needle. This observation provides direct evidence that an electrical current flowed through the closed circuit, promoted by the temperature difference.

The temperature difference causes, in the material, the diffusion of charge carriers (electrons or holes) from the hot junction to the cold junction. A configuration of moving charge carriers migrates to the cold side and leaves behind immobile cores of opposite charge on the hot side, thus giving rise to a thermoelectric voltage. Accumulation of

charge carriers on the cold side eventually ceases when an equal amount of charge carriers drift back to the hot side as a result of an electric field created by the separation of charges.

At this point, the material reaches an equilibrium state and only an increase in temperature difference may increase the number of charge carriers on the cold side and thus increase the thermoelectric voltage. An EMF (*Electromotive Force*) is generated between two different materials such as metals or semiconductors.

This leads to a direct current flowing through the materials through their junctions when they are held at different temperatures. The parameter associated with this effect is the so-called Seebeck coefficient S, which indicates the material's behavior in terms of the voltage generated in it when subjected to a temperature gradient.

In 1851, Gustav Magnus discovered that the voltage in the Seebeck effect does not depend on the temperature distribution across the metals between their junctions. This indicates that thermal energy is a function of the state. This is the physical basis for the thermocouple which is used as a sensor in temperature measurements.

In 1834, French watchmaker and physicist Jean Charles Athanase Peltier observed that an electrical current could either produce heating or cooling of a junction of two dissimilar metals. In 1838 Lens showed that depending on the flow of electric current, heat could either be removed from the junction until the water freezes or by reversing the current, promote the melting of ice.

The rate at which heat is absorbed or generated at the junction is proportionally linear concerning the applied electrical current, in contrast to irreversible Joule heating, which is quadratic concerning current. This is the main effect that refers to thermoelectric refrigeration or heat pumping.

Another very important parameter of materials, with an electrical character, is called resistivity ρ. It is defined as the electric field rate parallel to the current density i in the absence of a thermal gradient. In an isotropic conductor, the electrical conductivity σ is reciprocal to ρ, but there are situations in which the electric field and current may not be aligned and $\sigma \neq 1/\rho$. The application of a magnetic field in a given direction makes all materials anisotropic to some extent.

Electrical resistance is a property that has been extensively measured in materials, although it is simple, it presents special problems when it comes to electrical resistance measurements in thermoelectric materials. The electrical resistance R, of a piece of metal wire, is obtained by passing an electrical current known to the material and observing the electrical potential difference at its terminals. The electrical conductivity depends on the length of the conductor l and its cross-sectional area A. $\sigma = l/AR$ is somewhat difficult to find for a semiconductor because there is often a resistance associated with the contact.

The conventional way to overcome this problem involves the use of voltage measurement contacts inserted into the sample.

Thermal conductivity, represented by the letter κ, is the ability of the material to transfer heat when subjected to a temperature gradient across different points of its extension. In solids, it is highly dependent on the temperature and the atomic structure of the material.

At room temperature, thermal conduction by charge carriers occurs predominantly in metals. Thermal conductivity in thermoelectric materials consists of conductance via electrons and phonons.

The efficiency achieved in thermoelectric machines is limited by the thermal and electrical properties of the semiconductor materials in which thermal energy transport and electrical energy conversion take place. The elementary theory of thermoelectric machines is such that after optimizing the geometry of the thermoelements the coefficients of the thermal and electrical properties of the material can be combined into a simple efficiency parameter. This parameter is called the thermoelectric merit figure, represented by Z. It is used to assess the usefulness of a semiconductor for use in thermal machines or devices.

One of the main targets of research and development of thermoelectric materials is to manufacture semiconductors that present values of Z as high as possible at the temperatures at which the devices consisting of these semiconductors will be applied.

In general, semiconductor materials have better Z values when compared to metals. In a first analysis, it can be said that the reason for this is due to the Wiedemann-Franz Law, which establishes that the ratio between κ and σ is the same for all metals at a given temperature.

The figure of merit Z is given in terms of ρ, S and κ, according to the following equation:

$$Z = \frac{S^2}{\rho\kappa} \tag{1.1}$$

There is great difficulty in optimizing its value since in simple materials, the increase in the Seebeck coefficient leads to a decrease in electrical conductivity and the increase in electrical conductivity leads to a comparable increase in thermal conductivity.

For a thermoelectric module to have an efficiency comparable to mechanical systems equivalent to the dimensional merit figure ZT, which is Z multiplied by the temperature T, it must be approximately equal to 3, at room temperature [20, 21].

Many measurements are made on materials to obtain the figure of merit Z of the material. These measures logically involve measurements of the Seebeck S coefficient, the resistivity ρ and the thermal conductivity κ.

Among these measures, three stand out for their practicality and efficiency.

To measure the resistivity ρ, a widely used method is the so-called 4-point method. It consists of using 4 pins, which are in contact with the sample, linearly. The two external pins are used to apply the voltage to the material (and where the current is measured) and the two internal ones where the voltage is measured. Not measuring voltage values at the same points where it is applied corrects contact resistance and voltage drop effects.

The measure of the Seebeck coefficient S comes from the generation of a temperature gradient in the sample. This difference in temperature between the tips generates a potential difference. With accurate measurements of both quantities, we were able to obtain this characteristic of the sample.

The thermal conductivity measurement κ is made by the Kohlrausch method. It consists of heating the center of the sample while the tips are kept at lower and equal temperatures. In this process, the temperatures and the potential difference generated in the material between the center and the tips are measured.

The calculations require the value of the thermal conductivity σ, and, therefore, it is a measurement that must be taken together with a measurement of this magnitude. In our case, the 4-point one is described above.

These measurements are extremely effective and accurate and can be performed on a single device. With this, the value of the important thermoelectric quantity of materials is obtained, the figure of merit. The three methods described above can be applied both for measurements in bulk format materials or thin films.

TEM (*Temoelectric Modules*) uses solid-state thermoelectric material that generates a temperature gradient through electrical energy (Peltier effect). During operation, electrical current flows through the thermoelectric module to generate a temperature difference, transferring heat from the cold side to the hot one. Currently, a single TEM is capable of generating a temperature gradient of up to 70 K.

Heat is absorbed in the cold side of a TEM, which has the same role as the conventional system evaporator. The source of electricity has the same function as the compressor in the conventional system, providing energy to move electrons through the system. In the hot side, which behaves like the condenser in the conventional system, heat is dissipated into the hot reservoir. Finally, following the same analogy, electrons play the role of the refrigerant in the conventional system.

Unlike other refrigeration systems, thermoelectric systems have no moving parts. Its solid-state guarantees high reliability and durability. Such systems can reach cooling temperatures of up to -1000 °C, using cascaded thermoelectric modules. They also allow temperature control with precision up to ± 0.01 °C in a steady state. Another feature of thermoelectric systems is the possibility of heating or cooling only changing the direction

of the current.

The technology involved in these devices is entirely solid-state, as these elements are composed of n-type and p-type semiconductors, which makes thermoelectric systems simple when compared to conventional energy conversion systems [22, 23].

In the thermoelectric cooler, the Peltier effect occurs, in this case, the electrons in the n-type semiconductor and the holes in the p-type semiconductor remove heat from the metal-semiconductor junctions, which leads to their cooling. If a temperature difference is maintained between the two ends of the materials, the high thermal energy from the electrons and holes will diffuse to the cold side, creating a potential difference, which can be used to generate external power, in this case, the thermoelectric effect involved is Seebeck and there is a thermoelectric generator [23, 24]

There are great advantages in using these devices, as they are light, compact, silent, do not pollute the environment, and have great durability, for these reasons they are applied in space air, for example, by NASA in Voyager I and II and the Cassini mission to Saturn [20]. Despite the advantages presented, there are still problems in the applicability of these systems, as they have low efficiency when compared to the mechanical equivalents [22].

With the growth in the production of new devices, such as ultra-fast and flexible electronic devices, more efficient solar panels, micrometric transistors and safer medical devices, a new field in research into more efficient materials has started, with many reduced dimensions of the order of nanometers, especially two-dimensional semiconductor materials, formed by a simple layer of atoms or molecules.

With advances in graphene research since 2004 [25], other materials 2D (*Two Dimensional*) were synthesized in the most varied classes and have received great attention in research in materials sciences. In 2D materials, electrons and phonons are confined in a layer, which makes these materials have unique properties, different from their bulk counterparts [26].

Graphene, as the main reference for two-dimensional specimens, has high electrical mobility, excellent thermal conductivity, and excellent mechanical strength, however, its applicability in the semiconductor device industry is limited by its zero energy gap [27]. When it comes to technology, one of the most special characteristics of a solid is the energy gap, which is defined as the interval between the top of the valence band and the bottom of the material's conduction band. To engineer graphene's energy gap, complex techniques are required that greatly increase its production cost. A less expensive alternative to this engineering would be to produce graphene-like semiconductor materials.

Graphene is a conductor, boron nitride (BN) is an insulating material, and also dichogenates which are semiconductor materials (MoS_2, WS_2, $MoSe_2$ WSe_2, phospho-

rene, etc.) [28]. MoS_2 was one of the first two-dimensional semiconductor materials to be isolated [29] and presented new characteristics due to the reduction of the material's dimensionality, such as the change in the indirect energy gap (material three-dimensional), to direct (monolayer) [30].

The production of 2D molybdenum structures is widespread in the literature. Several routes for the production of quality monolayers can be taken, however, three processes are the most mentioned: microcleavage of a molybdenite crystal, chemical exfoliation, and CVD (*Chemical Vapor Deposition*). Microcleavage, as with graphene, produces the best crystalline quality samples, since the monolayer is removed directly from a natural crystal, but the production process is random and poorly reproducible. Chemical exfoliation has low cost and a high potential for scale production, however, chemical processes involving toxic agents. Chemical vapor deposition is a technique capable of producing large monolayer films of good quality and good reproducibility [31].

Molybdenum (Mo) is part of the family of transition metals, which are located in block B (group 3-12) in the periodic table. According to IUPAC (*International Union of Pure and Applied Chemistry*), a transition metal is defined as an element whose atom has the incompleted sublevel, or which can form cations with an incomplete sublevel. Molybdenum has a metallic color at room temperature.

The most common oxidation states of molybdenum are Mo^{+2}, Mo^{+3}, Mo^{+4}, Mo^{+5}, and Mo^{+6}, molybdenum can be classified as a good electrical conductor. Today there are many applications for molybdenum such as metallic alloys with high mechanical and corrosive resistance; catalyst in industries (for sulfur removal); filaments of electrical components.

In the field of these alternative materials, the ones that stand out the most are the TMD (*Transition Metal Dichalcogenides*). They are represented by the nomenclature MX_2, which refers to the possible combinations of the components of the periodic table, where M = transition metal (Ti, Zr, Hf, V, Nb, Ta, Mo, W, Tc, Re, Co, Rh, Ir, Ni, Pd, Pt) and X = Calcogenide (S, Se, Te) [1]. MX_2 forms a large family of materials that have various physical properties, such as semiconductors, semimetals, topological insulators and superconductors. Among these materials, MoS_2, WS_2, $MoSe_2$, WSe_2 and $MoTe_2$, they are semiconductors and arouse a special interest, since their gaps can be adjusted according to the number of layers, making them, therefore, excellent candidates for applications in nanodevices [27].

A material with the wide application is graphene [32, 33, 34], and its discovery enabled the rise of a new class of 2D materials, called dichalcogenated transition metals (TMD) [35], where the bulk configuration is already well known in materials science.

In numbers, the TMD are around 60, but only a third of them assume monolayer

structures. Most of these crystals are synthetic, but there are natural crystals [36]. TMD monolayers have been studied due to their diversity of band structure, the easy fabrication of heterostructures and the great potential for applications in electronic devices due to their optical and electrical performance [26].

The monolayers of TMD have distinct properties from the bulk form, such properties can transit between metals, semiconductors [37] and insulators [38] and meet new applications in electronics and photonics, since it made it possible to obtain semiconductors on an atomic scale, the so-called 2D [39, 40] semiconductors. Among these semiconductors, molybdenum disulfide monolayers present optical and electrical characteristics of interest in research [41, 42, 43, 44]. 'MoS$_2$ monolayer' is defined as MoS$_2$ layers in the order of 0.65 to 0.70 nm thick [29, 30, 41, 45].

Depending on the arrangement of the sulfur layers, it is possible to obtain three distinct geometries for the MoS$_2$: the 2H (*Trigonal Prismatic*) geometry, with hexagonal symmetry, two layers per repeated unit and trigonal prismatic coordination; 3R (*Trigonal Prismatic*), with rhombohedral symmetry, three layers per repeated unit and trigonal prismatic coordination and; 1T (*Octahedral*), with tetragonal symmetry, one layer per repetitive unit and octahedral coordination [27, 46, 47].

Among the possible geometries, the 2H-MoS$_2$ is the most researched in the last decade because it is naturally found in the form of the molybdenite mineral [46, 48]. The first article mentioned in the 2H-MoS$_2$ was published by Linus Pauling in his doctorate at the California Institute of Technology - Caltech [49].

Among so many possibilities of TMD, MoS$_2$ presents a justifiable advantage for research due to its versatility in applications. This material has anti-friction mechanical properties and can replace liquid lubricants that present environmental and unhealthy problems [50, 51]. It can be used as an additive in common greases, reducing wear and friction coefficient, in addition to being used as an additive in mineral and synthetic oils used in industrial plants. Its use in HDT (*Hydrotreating*) to remove S, O, N, and metals from fuels is also possible [46].

It is promising in the manufacture of phototransistors [38, 52], transistors [27] and cathodes for lithium batteries [46], featuring high mobility and high current gain. MoS$_2$ can also be used in solar cells [53] and light emitting devices [54, 55]. Recently, MoS$_2$ was obtained in the form of nanotubes [56, 57, 58] and nanospheres [59, 60], opening a wide variety of new applications in the market. It was also discovered that, by unifying conductive graphene with semiconductor lamellae of MoS$_2$, it is possible to create a 'flash' type material, widely used in pen drives and external hard drives [61]. MoS$_2$ is also a strong candidate for applications in spinelectronic components [62, 63].

In addition to the great versatility of this material, its natural abundance and af-

fordable prices [37, 64, 65, 66] make the material attractive for research and applications. Another great advantage of the MoS_2 would be the improved photoluminescence in the monolayers [37, 64, 65, 66], an area of research interest, allowing its use as a monolayer in composites for photocatalytic and electrocatalytic reactions in evolution reactions hydrogen [65]. Through the work of Zhu and co-authors [67], there are interactions of the monolayers of MoS_2 with the DNA (*Deoxyribonucleic Acid*), allowing applications in the biomedical area due to the FL (*Fermi Level*) of the monolayers.

According to Lee and coauthors, the photoelectric probe on the MoS_2 monolayer shows a direct gap E_g of 1.8 eV [29, 52], which explains the FL of the monolayers. For two and three monolayers of the same material there is a decrease in the direct gap to 1.65 and 1.35 eV, respectively [52]. In the bulk structure, MoS_2 presents 1.2 eV of indirect gap E_g' [68].

The study of TMD monolayers is of considerable relevance given its current status in the field of research, as there are still two decades of study on this material in the form of a monolayer. Thus, the development of TMD mentions the initial milestone for obtaining monolayers in 2D: the synthesis of graphene.

Graphene, obtained through the process of exfoliating graphite, was known for 150 years [46]. On the other hand, the first mention of the molybdenum disulfide exfoliation process in the bulk structure was described in 1986 by a group of researchers from Canada [46, 69, 70].

If there is a change in the transition metal family, the electromagnetic properties of the material may change significantly [35]. TMD has a range of possible properties, where the possibility of the material presenting conductive, semiconducting, or insulating properties is observed, depending on the chemical elements belonging to the material [35, 37].

In bulk, a known application is in pellets. In this process, the powder of the desired material is taken, and this powder goes through a physical and chemical process. In the case of MoS_2 pellet, the most used process starts with drying the powder at a certain temperature. After that, the pressing is done in a specific press, usually hydraulic, with the desired size of the insert. In the end, the pellet is taken to an oven under controlled temperature and atmosphere and sintered. This insert provides us with information about the material, and structural, chemical, and thermoelectric measurements can be performed.

Another excellent type of thermoelectric material, with many applications, is in thin-film format. There would be great material savings if thermoelectric modules could be made shorter while maintaining the dimensions of their cross-sections as those of commercial products. Aggravating problems in heat transfer appear when the length of

the elements of a thermocouple is less than something around 100 μm and there are also difficulties associated with electrical resistance in its contacts, but this did not prevent the fabrication and use of thermoelectric micro-modules.

For many purposes, the thermal and electrical fluxes are expected to be perpendicular to the surface of the films, but there are devices in which the fluxes are parallel. In this case, heat losses from the substrate have to be taken into account.

So, in order to study thermoelectric materials and develop the necessary tools for this purpose, we developed the following works.

In Chapter 1 we characterize a solar concentrator using thermoelectric generators through a computational method called Genetic Algorithms. In Chapter 2 we deepen our analysis of the solar concentrator, and we develop another computational tool, this time using the cross-entropy method.

The generators used in the solar concentrator of the previous chapters have another version, which we chose to study for a future application. For this, in the Chapter 3, we developed an equipment to analyze them and using Genetic Algorithms to analyze the data.

In Chapter 4 we developed equipment to carry out the thermoelectric characterization of materials, together with the necessary software for control.

In Chapter 5 we show our work in progress. There, we grew MoS_2 samples and are performing the thermoelectric characterization of the pellets produced.

References

1   GOLDBERG, D. E. *Genetic algorithms*. [S.l.]: Pearson Education India, 2006. 19

2   STORN, R.; PRICE, K. *Journal of Global Optimization*, Springer Science and Business Media LLC, v. 11, n. 4, p. 341–359, 1997. Disponível em: <https://doi.org/10.1023/a:1008202821328>. 20

3   RAMLI, M. A.; BOUCHEKARA, H.; ALGHAMDI, A. S. Optimal sizing of PV/wind/diesel hybrid microgrid system using multi-objective self-adaptive differential evolution algorithm. *Renewable Energy*, Elsevier BV, v. 121, p. 400–411, jun. 2018. Disponível em: <https://doi.org/10.1016/j.renene.2018.01.058>. 20

4   BEIRAMI, H.; SHABESTARI, A. Z.; ZERAFAT, M. M. Optimal PID plus fuzzy controller design for a PEM fuel cell air feed system using the self-adaptive differential evolution algorithm. *International Journal of Hydrogen Energy*, Elsevier BV, v. 40, n. 30, p. 9422–9434, ago. 2015. Disponível em: <https://doi.org/10.1016/j.ijhydene.2015.05.114>. 20

5   SUN, C.-H. et al. Comparison of dynamic differential evolution and self-adaptive dynamic differential evolution for buried metallic cylinder. *Research in Nondestructive Evaluation*, Informa UK Limited, v. 24, n. 1, p. 35–50, jan. 2013. Disponível em: <https://doi.org/10.1080/09349847.2012.699607>. 20

6   NANDI, S.; REDDY, M. J. Comparative performance evaluation of self-adaptive differential evolution with GA, SCE and DE algorithms for the automatic calibration of a computationally intensive distributed hydrological model. *H2Open Journal*, IWA Publishing, v. 3, n. 1, p. 306–327, jan. 2020. Disponível em: <https://doi.org/10.2166/h2oj.2020.030>. 20

7   DAS, S.; MULLICK, S. S.; SUGANTHAN, P. Recent advances in differential evolution – an updated survey. *Swarm and Evolutionary Computation*, v. 27, p. 1–30, 2016. ISSN 2210-6502. Disponível em: <https://www.sciencedirect.com/science/article/pii/S2210650216000146>. 20

8   ELSAYED, S.; SARKER, R. Differential evolution framework for big data optimization. *Memetic Computing*, Springer Science and Business Media LLC, v. 8, n. 1, p. 17–33, jan. 2016. Disponível em: <https://doi.org/10.1007/s12293-015-0174-x>. 20

9   KITTEL, C. *Introduction to Solid State Physics*. 6th. ed. New York: John Wiley & Sons, Inc., 1986.

10 W, A. et al. *Solid State Physics*. Holt, Rinehart and Winston, 1976. (HRW international editions). ISBN 9780030839931. Disponível em: <https://books.google.com.br/books?id=1C9HAQAAIAAJ>. 20

11 LUNDSTROM, M. *Fundamentals of Carrier Transport*. Cambridge University Press, 2000. Disponível em: <https://doi.org/10.1017/cbo9780511618611>. 20

12 BELL, L. E. Cooling, heating, generating power, and recovering waste heat with thermoelectric systems. *Science*, American Association for the Advancement of Science (AAAS), v. 321, n. 5895, p. 1457–1461, set. 2008. Disponível em: <https://doi.org/10.1126/science.1158899>. 20

13 DISALVO, F. J. Thermoelectric cooling and power generation. *Science*, American Association for the Advancement of Science (AAAS), v. 285, n. 5428, p. 703–706, jul. 1999. Disponível em: <https://doi.org/10.1126/science.285.5428.703>. 20

14 MAHAN, G.; SALES, B.; SHARP, J. Thermoelectric materials: New approaches to an old problem. *Physics Today*, AIP Publishing, v. 50, n. 3, p. 42–47, mar. 1997. Disponível em: <https://doi.org/10.1063/1.881752>. 20, 21

15 HARMAN, T. C. Quantum dot superlattice thermoelectric materials and devices. *Science*, American Association for the Advancement of Science (AAAS), v. 297, n. 5590, p. 2229–2232, set. 2002. Disponível em: <https://doi.org/10.1126/science.1072886>. 20

16 MAHAN, G. D.; SOFO, J. O. The best thermoelectric. *Proceedings of the National Academy of Sciences*, Proceedings of the National Academy of Sciences, v. 93, n. 15, p. 7436–7439, jul. 1996. Disponível em: <https://doi.org/10.1073/pnas.93.15.7436>. 20

17 REDDY, P. et al. Thermoelectricity in molecular junctions. *Science*, American Association for the Advancement of Science (AAAS), v. 315, n. 5818, p. 1568–1571, mar. 2007. Disponível em: <https://doi.org/10.1126/science.1137149>. 21

18 GOLDSMID, H. J.; DOUGLAS, R. W. The use of semiconductors in thermoelectric refrigeration. *British Journal of Applied Physics*, IOP Publishing, v. 5, n. 11, p. 386–390, nov. 1954. Disponível em: <https://doi.org/10.1088/0508-3443/5/11/303>. 21

19 IOFFE, A. F. et al. Semiconductor thermoelements and thermoelectric cooling. *Physics Today*, AIP Publishing, v. 12, n. 5, p. 42–42, maio 1959. Disponível em: <https://doi.org/10.1063/1.3060810>. 21

20 SALES, B. C. THERMOELECTRIC MATERIALS: Smaller is cooler. *Science*, American Association for the Advancement of Science (AAAS), v. 295, n. 5558, p. 1248–1249, fev. 2002. Disponível em: <https://doi.org/10.1126/science.1069895>. 23, 25

21 GELBSTEIN, Y.; DASHEVSKY, Z.; DARIEL, M. High performance n-type PbTe-based materials for thermoelectric applications. *Physica B: Condensed Matter*, Elsevier BV, v. 363, n. 1-4, p. 196–205, jun. 2005. Disponível em: <https://doi.org/10.1016/j.physb.2005.03.022>. 23

22 HEREMANS, J. Low-dimensional thermoelectricity. *Acta Physica Polonica A*, Institute of Physics, Polish Academy of Sciences, v. 108, n. 4, p. 609–634, out. 2005. Disponível em: <https://doi.org/10.12693/aphyspola.108.609>. 25

23 HILLHOUSE, H. W.; TUOMINEN, M. T. Modeling the thermoelectric transport properties of nanowires embedded in oriented microporous and mesoporous films. *Microporous and Mesoporous Materials*, Elsevier BV, v. 47, n. 1, p. 39–50, set. 2001. Disponível em: <https://doi.org/10.1016/s1387-1811(01)00289-x>. 25

24 CHEN, G.; SHAKOURI, A. Heat transfer in nanostructures for solid-state energy conversion. *Journal of Heat Transfer*, ASME International, v. 124, n. 2, p. 242–252, nov. 2001. Disponível em: <https://doi.org/10.1115/1.1448331>. 25

25 WANG, S.; WANG, X.; WARNER, J. H. All chemical vapor deposition growth of MoS2:h-BN vertical van der waals heterostructures. *ACS Nano*, American Chemical Society (ACS), v. 9, n. 5, p. 5246–5254, abr. 2015. Disponível em: <https://doi.org/10.1021/acsnano.5b00655>. 25

26 LI, X.; ZHU, H. Two-dimensional MoS2: Properties, preparation, and applications. *Journal of Materiomics*, Elsevier BV, v. 1, n. 1, p. 33–44, mar. 2015. Disponível em: <https://doi.org/10.1016/j.jmat.2015.03.003>. 25, 27

27 WANG, Q. H. et al. Electronics and optoelectronics of two-dimensional transition metal dichalcogenides. *Nature Nanotechnology*, Springer Science and Business Media LLC, v. 7, n. 11, p. 699–712, nov. 2012. Disponível em: <https://doi.org/10.1038/nnano.2012.193>. 25, 26, 27

28 LUO, S. et al. Photoresponse properties of large-area MoS2 atomic layer synthesized by vapor phase deposition. *Journal of Applied Physics*, AIP Publishing, v. 116, n. 16, p. 164304, out. 2014. Disponível em: <https://doi.org/10.1063/1.4898861>. 26

29 RADISAVLJEVIC, B. et al. Single-layer MoS2 transistors. *Nature Nanotechnology*, Springer Science and Business Media LLC, v. 6, n. 3, p. 147–150, jan. 2011. Disponível em: <https://doi.org/10.1038/nnano.2010.279>. 26, 27, 28

30 GHATAK, S.; PAL, A. N.; GHOSH, A. Nature of electronic states in atomically thin MoS2 field-effect transistors. *ACS Nano*, American Chemical Society (ACS), v. 5, n. 10, p. 7707–7712, set. 2011. Disponível em: <https://doi.org/10.1021/nn202852j>. 26, 27

31 WANG, S.; AN, C.; YUAN, J. Synthetic fabrication of nanoscale MoS2-based transition metal sulfides. *Materials*, MDPI AG, v. 3, n. 1, p. 401–433, jan. 2010. Disponível em: <https://doi.org/10.3390/ma3010401>. 26

32 YIN, J. et al. Generating electricity by moving a droplet of ionic liquid along graphene. *Nature Nanotechnology*, Springer Science and Business Media LLC, v. 9, n. 5, p. 378–383, abr. 2014. Disponível em: <https://doi.org/10.1038/nnano.2014.56>. 26

33 TRAVERSI, F. et al. Detecting the translocation of DNA through a nanopore using graphene nanoribbons. *Nature Nanotechnology*, Springer Science and Business Media LLC, v. 8, n. 12, p. 939–945, nov. 2013. Disponível em: <https://doi.org/10.1038/nnano.2013.240>. 26

34 TU, Y. et al. Destructive extraction of phospholipids from escherichia coli membranes by graphene nanosheets. *Nature Nanotechnology*, Springer Science and Business Media LLC, v. 8, n. 8, p. 594–601, jul. 2013. Disponível em: <https://doi.org/10.1038/nnano.2013.125>. 26

35 MANZELI, S. et al. 2d transition metal dichalcogenides. *Nature Reviews Materials*, Springer Science and Business Media LLC, v. 2, n. 8, jun. 2017. Disponível em: <https://doi.org/10.1038/natrevmats.2017.33>. 26, 28

36 BERNARDS, D. A.; MALLIARAS, G. G.; OWENS, R. M. (Ed.). *Organic Semiconductors in Sensor Applications*. Springer Berlin Heidelberg, 2008. Disponível em: <https://doi.org/10.1007/978-3-540-76314-7>. 27

37 CHHOWALLA, M. et al. The chemistry of two-dimensional layered transition metal dichalcogenide nanosheets. *Nature Chemistry*, Springer Science and Business Media LLC, v. 5, n. 4, p. 263–275, mar. 2013. Disponível em: <https://doi.org/10.1038/nchem.1589>. 27, 28

38 ZHANG, Q. et al. A highly sensitive, highly transparent, gel-gated MoS2 phototransistor on biodegradable nanopaper. *Nanoscale*, Royal Society of Chemistry (RSC), v. 8, n. 29, p. 14237–14242, 2016. Disponível em: <https://doi.org/10.1039/c6nr01534d>. 27

39 PONRAJ, J. S. et al. Photonics and optoelectronics of two-dimensional materials beyond graphene. *Nanotechnology*, IOP Publishing, v. 27, n. 46, p. 462001, out. 2016. Disponível em: <https://doi.org/10.1088/0957-4484/27/46/462001>. 27

40 CHOI, W. et al. Recent development of two-dimensional transition metal dichalcogenides and their applications. *Materials Today*, Elsevier BV, v. 20, n. 3, p. 116–130, abr. 2017. Disponível em: <https://doi.org/10.1016/j.mattod.2016.10.002>. 27

41 SPLENDIANI, A. et al. Emerging photoluminescence in monolayer MoS2. *Nano Letters*, American Chemical Society (ACS), v. 10, n. 4, p. 1271–1275, mar. 2010. Disponível em: <https://doi.org/10.1021/nl903868w>. 27

42 EDA, G. et al. Photoluminescence from chemically exfoliated MoS2. *Nano Letters*, American Chemical Society (ACS), v. 11, n. 12, p. 5111–5116, dez. 2011. Disponível em: <https://doi.org/10.1021/nl201874w>. 27

43 HSU, W.-T. et al. Second harmonic generation from artificially stacked transition metal dichalcogenide twisted bilayers. *ACS Nano*, American Chemical Society (ACS), v. 8, n. 3, p. 2951–2958, fev. 2014. Disponível em: <https://doi.org/10.1021/nn500228r>. 27

44 RASMUSSEN, F. A.; THYGESEN, K. S. Computational 2d materials database: Electronic structure of transition-metal dichalcogenides and oxides. *The Journal of Physical Chemistry C*, American Chemical Society (ACS), v. 119, n. 23, p. 13169–13183, jun. 2015. Disponível em: <https://doi.org/10.1021/acs.jpcc.5b02950>. 27

45 YOON, Y.; GANAPATHI, K.; SALAHUDDIN, S. How good can monolayer MoS2transistors be? *Nano Letters*, American Chemical Society (ACS), v. 11, n. 9, p. 3768–3773, set. 2011. Disponível em: <https://doi.org/10.1021/nl2018178>. 27

46 WYPYCH, F. MOLYBDENUM DISULFIDE, a MULTIFUNCTIONAL AND REMARKABLE MATERIAL: TWELVE YEARS ON. *Química Nova*, GN1 Genesis Network, 2014. Disponível em: <https://doi.org/10.5935/0100-4042.20140150>. 27, 28

47 YAN, S. et al. Enhancement of magnetism by structural phase transition in MoS2. *Applied Physics Letters*, AIP Publishing, v. 106, n. 1, p. 012408, jan. 2015. Disponível em: <https://doi.org/10.1063/1.4905656>. 27

48 ZHAO, M. et al. Atomically phase-matched second-harmonic generation in a 2d crystal. *Light: Science & Applications*, Springer Science and Business Media LLC, v. 5, n. 8, p. e16131–e16131, mar. 2016. Disponível em: <https://doi.org/10.1038/lsa.2016.131>. 27

49 DICKINSON, R. G.; PAULING, L. THE CRYSTAL STRUCTURE OF MOLYBDENITE. *Journal of the American Chemical Society*, American Chemical Society (ACS), v. 45, n. 6, p. 1466–1471, jun. 1923. Disponível em: <https://doi.org/10.1021/ja01659a020>. 27

50 SAVAN, A. et al. Modern solid lubrication: Recent developments and applications of MoS2. *Lubrication Science*, Wiley, v. 12, n. 2, p. 185–203, fev. 2000. Disponível em: <https://doi.org/10.1002/ls.3010120206>. 27

51 HAO, R. et al. Property self-optimization during wear of MoS2. *ACS Applied Materials & Interfaces*, American Chemical Society (ACS), v. 9, n. 2, p. 1953–1958, jan. 2017. Disponível em: <https://doi.org/10.1021/acsami.6b13802>. 27

52 LEE, H. S. et al. MoS2 nanosheet phototransistors with thickness-modulated optical energy gap. *Nano Letters*, American Chemical Society (ACS), v. 12, n. 7, p. 3695–3700, jun. 2012. Disponível em: <https://doi.org/10.1021/nl301485q>. 27, 28

53 SUNDARAM, R. S. et al. Electroluminescence in single layer MoS2. *Nano Letters*, American Chemical Society (ACS), v. 13, n. 4, p. 1416–1421, mar. 2013. Disponível em: <https://doi.org/10.1021/nl400516a>. 27

54 FENG, J. et al. Strain-engineered artificial atom as a broad-spectrum solar energy funnel. *Nature Photonics*, Springer Science and Business Media LLC, v. 6, n. 12, p. 866–872, nov. 2012. Disponível em: <https://doi.org/10.1038/nphoton.2012.285>. 27

55 FONTANA, M. et al. Electron-hole transport and photovoltaic effect in gated MoS2 schottky junctions. *Scientific Reports*, Springer Science and Business Media LLC, v. 3, n. 1, abr. 2013. Disponível em: <https://doi.org/10.1038/srep01634>. 27

56 REMSKAR, M. et al. MoS2 AND WS2 NANOTUBES ALLOYED WITH GOLD AND SILVER. *Surface Review and Letters*, World Scientific Pub Co Pte Lt, v. 06, n. 06, p. 1283–1287, dez. 1999. Disponível em: <https://doi.org/10.1142/s0218625x9900144x>. 27

57 ROTHSCHILD, A.; SLOAN, J.; TENNE, R. Growth of WS2nanotubes phases. *Journal of the American Chemical Society*, American Chemical Society (ACS), v. 122, n. 21, p. 5169–5179, maio 2000. Disponível em: <https://doi.org/10.1021/ja994118v>. 27

58 TENNE, R. Fullerene-like materials and nanotubes from inorganic compounds with a layered (2-d) structure. *Colloids and Surfaces A: Physicochemical and Engineering Aspects*, Elsevier BV, v. 208, n. 1-3, p. 83–92, ago. 2002. Disponível em: <https://doi.org/10.1016/s0927-7757(02)00104-8>. 27

59 FELDMAN, Y. et al. Bulk synthesis of inorganic fullerene-like MS2(m = mo, w) from the respective trioxides and the reaction mechanism. *Journal of the American Chemical Society*, American Chemical Society (ACS), v. 118, n. 23, p. 5362–5367, jan. 1996. Disponível em: <https://doi.org/10.1021/ja9602408>. 27

60 ZAK, A. et al. Alkali metal intercalated fullerene-like MS2 (m = w, mo) nanoparticles and their properties. *Journal of the American Chemical Society*, American Chemical Society (ACS), v. 124, n. 17, p. 4747–4758, abr. 2002. Disponível em: <https://doi.org/10.1021/ja012060q>. 27

61 BERTOLAZZI, S.; KRASNOZHON, D.; KIS, A. Nonvolatile memory cells based on MoS2/graphene heterostructures. *ACS Nano*, American Chemical Society (ACS), v. 7, n. 4, p. 3246–3252, mar. 2013. Disponível em: <https://doi.org/10.1021/nn3059136>. 27

62 KLINOVAJA, J.; LOSS, D. Spintronics in MoS2monolayer quantum wires. *Physical Review B*, American Physical Society (APS), v. 88, n. 7, ago. 2013. Disponível em: <https://doi.org/10.1103/physrevb.88.075404>. 27

63 HAN, S. W. et al. Controlling ferromagnetic easy axis in a LayeredMoS2single crystal. *Physical Review Letters*, American Physical Society (APS), v. 110, n. 24, jun. 2013. Disponível em: <https://doi.org/10.1103/physrevlett.110.247201>. 27

64 HU, J. et al. Tribological properties of pulsed laser deposited mo–s–te composite films at moderate high temperatures. *Surface and Coatings Technology*, Elsevier BV, v. 203, n. 16, p. 2322–2327, maio 2009. Disponível em: <https://doi.org/10.1016/j.surfcoat.2009.02.057>. 28

65 LU, Q. et al. 2d transition-metal-dichalcogenide-nanosheet-based composites for photocatalytic and electrocatalytic hydrogen evolution reactions. *Advanced Materials*, Wiley, v. 28, n. 10, p. 1917–1933, dez. 2015. Disponível em: <https://doi.org/10.1002/adma.201503270>. 28

66 CHANG, K.; HAI, X.; YE, J. Transition metal disulfides as noble-metal-alternative co-catalysts for solar hydrogen production. *Advanced Energy Materials*, Wiley, v. 6, n. 10, p. 1502555, mar. 2016. Disponível em: <https://doi.org/10.1002/aenm.201502555>. 28

67 ZHU, C. et al. Single-layer MoS2-based nanoprobes for homogeneous detection of biomolecules. *Journal of the American Chemical Society*, American Chemical Society (ACS), v. 135, n. 16, p. 5998–6001, abr. 2013. Disponível em: <https://doi.org/10.1021/ja4019572>. 28

68 KAM, K. K.; PARKINSON, B. A. Detailed photocurrent spectroscopy of the semiconducting group VIB transition metal dichalcogenides. *The Journal of Physical Chemistry*, American Chemical Society (ACS), v. 86, n. 4, p. 463–467, fev. 1982. Disponível em: <https://doi.org/10.1021/j100393a010>. 28

69 JOENSEN, P.; FRINDT, R.; MORRISON, S. Single-layer MoS2. *Materials Research Bulletin*, Elsevier BV, v. 21, n. 4, p. 457–461, abr. 1986. Disponível em: <https://doi.org/10.1016/0025-5408(86)90011-5>. 28

70 JOENSEN, P. et al. A study of single-layer and restacked MoS2by x-ray diffraction and x-ray absorption spectroscopy. *Journal of Physics C: Solid State Physics*, IOP Publishing, v. 20, n. 26, p. 4043–4053, set. 1987. Disponível em: <https://doi.org/10.1088/0022-3719/20/26/009>.

28

2 Characterization of a Solar Concentration Thermoelectric Generator

In order to develop a complete study of thermoelectric materials, we start with a computational tool studied and adapted from the literature.

This chapter presents a work I carried out in collaboration with Fernandes, AA, where I applied the SADE to the case studied in his dissertation. SADE was adapted for the evolution of three parameters belonging to three equations, simultaneously.

This algorithm adapted by the research group of the LCM (*Materials Characterization Laboratory*) was registered and the Software Registration Certificate is presented in Annex A and was also used in the article presented in the Annex D.

The paper was published in the European Journal of Physics. The results of this work were presented at the events in the Annex E and F.

Graphical Abstract
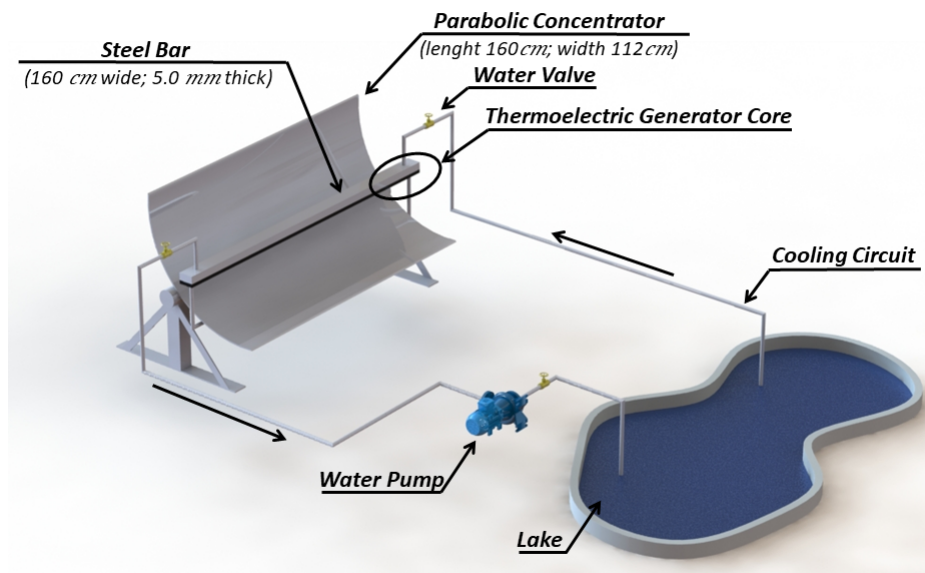
Figure 1 – Graphical Abstract of Publication 1

Highlights

- A didactic thermoelectric generator based on parabolic mirror solar concentrator was built and tested outdoor.

- Acquisition and analyses of the outdoor IV measurements were carried out at various irradiation and temperature conditions.

- Self-Adaptive Differential Evolution method was applied to extract parameters by simultaneously fitting (I,V,W,R_L) data.

Abstract

In this work we developed a didactic linear parabolic solar concentrator for use with Peltier cooling modules for power generation. The main idea is to maximize the temperature gradient between the hot and cold sides to provide maximum power for this system and use that in class for experimental explanations. The cold temperature is provided by a flow of water pumped from a cold water reservoir and the hot temperature provided by solar radiation which could reach up to 200 °C, but is limited to the Peltier modules allowed temperature of T< 140°C. This system is compact and lightweight when compared to conventional solar electric generators and can be easily assembled and used in lectures. For this system, we have dedicated to IV measurements and fitting models to precisely extract the model parameters in a robust simultaneous autonomous fitting of three equations. As far as we know, our parameter extraction approach was applied to thermoelectric generation for the first time.

Keywords

Solar concentrator ● Seebeck effect ● Self-adaptative Differential Evolution ● Efficiency ● Outdoor measurements

2.1 Introduction

Due to constant reduction in non-renewable natural resources used as power generation matrices [13] as well as the growing availability of semiconductors devices at frequent lowering costs for the fabrication of PVSC (*Photovoltaic Solar Cells*) [14] as well as TEG [15], alternative forms are becoming worldwide spread. In order to deal with intermittency associated to photovoltaic [16] and wind power generation, [17] limits of radiation absorption spectral range [18] and also efficiency decreases due to temperature effects on PVSC [19], the use of the TEG alone or in association with PVSC technology

must be considered. One remarkable advantage of TEGs against PVSC is that it generates energy more effective under cloudy weather [57] since long wavelength radiation are less subject to be contained by clouds being an effective form to cope with PVSC intermittency.

PVSC technology is based on a combination of two effects: electron-hole pair generation by incident light and some space-charge splitting of those pair as presented on Figure 2. In this example, space-charge effect is provided by a pn junction which builds a potential barrier at the junction.

On the other hand, TEG Technology is based on a single effect that is the Seebeck effect, presented on Figure 3. Seebeck effect is caused by the diffusion of carriers from the hot to the cold side of the sample building a difference of potential between them.

HPC (*Heliothermic Power Concentration*) is a viable form of power generation with many power plants and variable forms of power generation scattered throughout the world. With proper adaptations, HPC can be used with heat storage, allowing its use for power generation even at night or cloudy environments. Also, according to Singh et al. [21], the association of HPC with TEG technology is advantageous since it allows power generation without mechanical parts such as electrical generators, capacitors among other components, being noiseless, reliable and environment friendly. For this, TEGs convert heat energy from a temperature gradient that established a small voltage in the opposite terminals a pn junction of a thermoelectric material due to the Seebeck effect [22]. A TEG module is composed by more than a hundred of such junctions. Although there are numerous materials that present Seebeck effect commercially produced, the most commonly used materials is Bi_2Te_3 [23] since it presents a good Figure of Merit ZT and
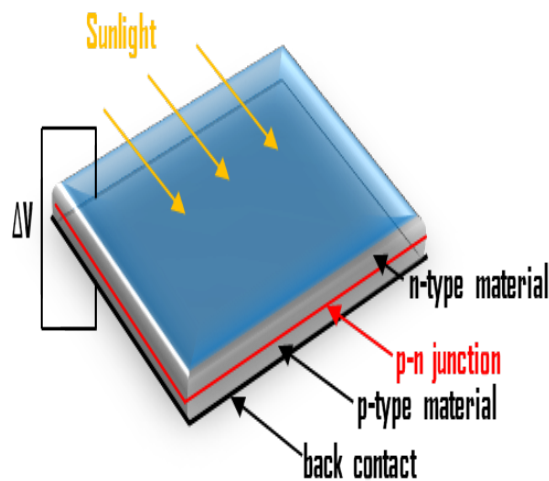
Figure 2 – Illustration of the PVSC containing all relevant parts and simplified operation characteristics.
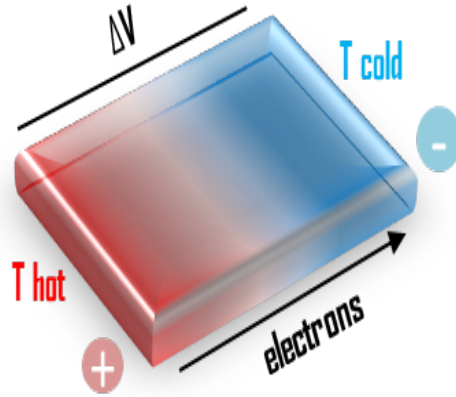
Figure 3 – Illustration of the Seebeck effect showing how the displacement of free charge
carriers, i.e. electrons builds a potential between sample extremes.

thus better tradeoff in US$ per Watt. Other worth to mention materials are PbTe, Bi_2Se_3,
Sb_2Te_3, GeTe [24].

In order to analyze TEG measurements, it is important to consider a proper theore-
tical background [43, 44, 45, 46]. For a TEG device, power is derived from thermodynamics
first law considering internal power dissipation RI^2 as

$$P = NI[S(T_h - T_c) - RI], \tag{2.1}$$

where N stands for number of pn junctions, S is the Seebeck coefficient, I the
current through the TEG, R its internal resistance, and T_h e T_c are the temperatures from
the hot and cold sides respectively. Output power can also be expressed as a function of
the load resistance R_L as

$$P = NI^2 R_L. \tag{2.2}$$

Thus, combining Equation 2.1 and 2.2 we obtained the Voltage across the load
resistance

$$V = NI[S(T_h - T_c) - RI]. \tag{2.3}$$

From Equation 2.1 and 2.2 the current can be isolated as

$$I = \frac{S(T_h - T_c)}{R_L + R}. \tag{2.4}$$

Here, we can see that the current is not a function of the number of pn junctions. We obtain the power as

$$P = \frac{NS^2(T_h - T_c)^2}{R} \frac{R_L/R}{(1 + R_L/R)^2}. \tag{2.5}$$

Considering the heat equation, thermal efficiency as the ratio between the output power and the heat absorbed from the hot side

$$\eta = \frac{P}{\phi} \tag{2.6}$$

where the power per modulus P is $P_{max}/8$ and the heat flux ϕ is

$$\phi = \frac{\kappa B \Delta T}{w} \tag{2.7}$$

where w the thickness, the surface area and κ is the thermal conductivity. The Equation 2.6 can be rewritten as

$$\eta = \frac{\left(1 - \frac{T_c}{T_h}\right) \frac{R_L}{R}}{\left(1 + \frac{R_L}{R}\right) - \frac{1}{2}\left(1 - \frac{T_c}{T_h}\right) \frac{\left(1 + \frac{R_L}{R}\right)^2 \frac{T_c}{T_h}}{ZT_c}}, \tag{2.8}$$

where $ZT_c = \frac{S^2 T_c}{\kappa \rho}$ and the ρ is electrical resistivity. It is also important to consider a comparison with the thermal efficiency of an ideal Carnot machine given by

$$\eta_c = 1 - \frac{T_c}{T_h}. \tag{2.9}$$

The maximum efficiency is obtained with $R_L = R$, so that

$$\eta_{max} = \left(1 - \frac{T_c}{T_h}\right) \frac{\sqrt{1 + Z\bar{T}} - 1}{\sqrt{1 + Z\bar{T}} + \frac{T_c}{T_h}}, \tag{2.10}$$

where, $\bar{T}$ is the average temperature between the hot and cold junction temperatures and is expressed by

$$\bar{T} = \frac{T_h + T_c}{2}, \tag{2.11}$$

and the maximum power equation is

$$P_{max} = \frac{NS^2(T_h - T_c)^2}{4R}. \tag{2.12}$$

Finally, the effective resistivity is

$$\rho = \frac{4P_{max}A/L}{N(I_{max})^2} \tag{2.13}$$

and the effective Z-factor is

$$Z_{eff} = \frac{1}{\overline{T}} \left[\left(\frac{1 + \frac{T_c \eta_{max}}{T_h \eta_c}}{1 - \frac{\eta_{max}}{\eta_c}} \right)^2 - 1 \right]. \tag{2.14}$$

Thus, this work consists in the experimental measurements of IV characteristics of a parabolic solar concentrator with Peltier modules in its focus and its subsequent analysis by a differential Evolution algorithm considering here presented equations. In the following we will describe our experimental setup and methods.

2.2 Materials and Methods

For this work we developed a cylindrical-parabolic solar concentrator module whose patent was registered with the INPI (*National Institute of Industrial Property*) [38]. It was developed onto folded and soldered metal bars as shown in Figure 4 (a). The parabolic concentrator has length 160 cm and width 112 cm. In the central parabolic axis, a vertical iron fixture was added in both extremes with wing nuts to fine tune the position of the TEG core, composed by eight TEC (*Thermoelectric Cooler*)s brand Danvic model HC-40-15.4 attached to a 160.0 cm iron profile and connected in series. The cold side of this core is attached to a rectangular tube 160.0 cm long with cross section as 0.5×5.0 cm^2 connected to the cold side of the modules. In Figure 4 (b) we present the generator schematics in which water is made to circulate through this tube by a submersible water pump brand Anauger model Ecco 60973 with a flow rate of 1050 Lh^{-1} placed inside university's lake in order to maintain constant the cold side temperature, since the dimensions of the lake is too large.

Since the lake is a large water mass its temperature is measured and kept constant throughout the entire experiment. The 160 cm wide 5.0 mm thick steel bar was also painted with black paint that supports high temperature (300 °C) to maximize heat absorption in order to provide highest hot side temperature to the modules. Temperature was measure by two K-type thermocouples: T_c measured the cold side at the contact between rectangular tubes and the modules and T_h measured the hot-side temperature, i.e. at the side of the bar that touches the modules.

In order to measure output electrical power from the setup we used precision portable Reed Instruments DW-6060 watt meter able to measure voltage and current as well as power and a 100 kΩ precision in series potentiometer used as load resistance with
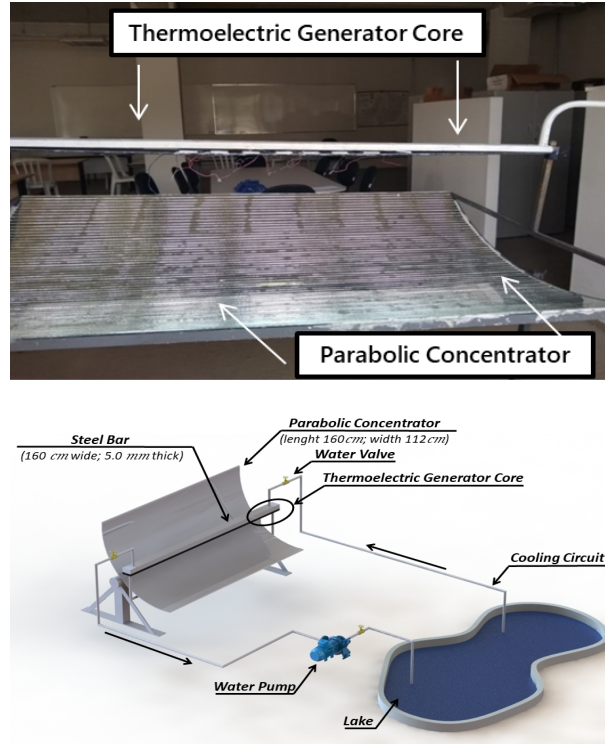
Figure 4 – (a) photograph and (b) schematics of the generator setup of the cylindrical-parabolic collector with dimensions. Main parts are indicated on the Figure.

the voltmeter connected in parallel to the in-series module association ampere meter in series and potentiometer in series too. The choice of instrument considered being battery powered since in field measurements were taken far from laboratory, not being possible to have benchtop instruments in use. Experimental data were collected as current-voltage IV characteristics with a constant temperature gradient throughout each measurement. Power output P was directly calculated as the product P = VI and load resistance R_L calculated according to Equation 2.3.

2.3 Differential Evolution Algorithm

Experimental data of thermoelectric generators were analyzed following the metaheuristic ADE (*Adaptative Evolution Algorithm*) [49]. In order to, obtain in a robust and automatic fashion the parameters electrical resistivity (ρ), thermal conductivity (κ) and an estimate of the Figure of Merit (ZT) of the associated modules studied. The metaheuristic method called DE was proposed by Storn and Price [51] and is an evolutionary algorithm based on natural selection mechanisms and population genetics. For this, the DE uses mutation, crossing and selection operators to generate new individuals in search of the most adapted. Initially, the DE algorithm was applied to solve continuous variable systems [51] and soon proved to be efficient for a wide range of problems [52, 53, 54, 34].

Later, he received an update, no longer dependent on control parameters that became self-adaptive [56], receiving the name of SADE. With this procedure, it is possible to find global minimum of multimodal non-linear functions in a light and efficient fashion, being popularly used to solve engineering problems [36] as that of TEG studied here.

About the peltier modules, is important to consider constitutive and intrinsic properties of a module to be considered in calculations. L is the characteristic length of a single pn junction, A the cross-sectional area, N the number of pn junctions and Z is the Z-factor which, multiplied by T gives the Figure of Merit. Those values are listed in Table 3. In the fittings we will consider as $8 \times N$, since our system contains eight in series Peltier modules.

$L(cm) \pm 0.002$	$A(cm^2) \pm 0.0005$	N	$Z(K^{-1})$
0.144	0.0259	127	0.0026

Table 3 – Sample dimensional parameters, number of pn junctions and Z-factor.

Initially, at ADE a set of individuals is generated, randomly, within predefined physical intervals, generating the initial population that will evolve through the generations. Each individual is a candidate for the solution that minimizes the objective function. In this work, the initial population of the parameter was obtained through Equation 2.15

$$X_{i,j}^{G=1} = X_l^{G=1} + rand_{i,j}(0,1)(X_u^{G=1} - X_l^{G=1}) \qquad (2.15)$$

with $rand_{ij}(0,1)$ being a real random number between 0 and 1. The index i goes from 1 to the population size NP (i.e. in this case 100) and the index j from 1 to 4, i.e. the number of parameters for the studied problem. X_u and X_l are the lower and upper bonds for the parameters according to Table 4, defining the search space and G stands for the generation ranging from 1 to G_{max}, the maximal number of iterations. In this work we used $G_{max} = 50000$. Each individual X_i is a candidate to be the optimal solution.

In mutation stage, a donor vector is generated, which in this work was obtained through Equation 2.16

$$V_i^G = X_i^G + F(X_{best}^G - X_i^G) + F(X_{r1}^G - X_{r2}^G) \qquad (2.16)$$

where V is the mutation vector that will select the tested individuals. (G, X_i^G) is the individuals generation where X_i^G stands for the present individual. (X_{r1}^G e X_{r2}^G) are randomly chosen to be others than X_i^G. X_{best}^G is the best individual, i.e. the one that minimizes the objective function f.

Besides that, F (F$\epsilon[0,2]$) is a real number, chosen by the user as the mutation factor, that is adjusted by Equation 2.17

$$F_i^{G+1} = \begin{cases} F_l + rand_1 F_u, & \text{if } rand_2 < \tau_1, \\ F_i^G, & \text{otherwise.} \end{cases} \qquad (2.17)$$

The crossover stage is defined by mixing the target vector X$_i^G$, produced by an experimental vector U$_i^G$ between 0 and 1, and carrying a comparison between the crossover values as:

$$U_{i,j}^G = \begin{cases} V_{i,j}, & \text{if } rand(0,1)_j \le CR \text{ or } j = j_{rand}, \\ X_{i,j}^G, & \text{otherwise.} \end{cases} \qquad (2.18)$$

where V$_{i,j}^G$ is the donor vector, j_{rand} is an integer random number between 1 and 6 and CR is another real number CR$\epsilon[0,1]$ is the crossing rate, defined by the Equation 2.19.

$$CR_i^{G+1} = \begin{cases} rand_3, & \text{if } rand_4 < \tau_2, \\ CR_i^G, & \text{otherwise.} \end{cases} \qquad (2.19)$$

where $rand_4$ are 4 random numbers between 0 and 1. τ_1 and τ_2 represent the probabilities of fitting F and CR.

Finally, in the selection step the temporary vector is the vector X$_i^G$ are compared and the vectors that best minimize the objective function are chosen, using the Equation 2.20 relationship.

$$X_i^{G+1} = \begin{cases} U_i^G, & \text{if } f(U_i) < f(X_i), \\ X_{i,j}^G, & \text{otherwise.} \end{cases} \qquad (2.20)$$

This process repeats until the end of generations, or some predefined criterion is satisfied.

From this fitting procedure a consistent simultaneous fitting of V, I and P allows the parameters associated to the experimental curves to be extracted as will be presented on Tables 6 and 7 in the results section.

For this method to reach consistently best performance on the parameters we considered the constraints according to Table 4 for all of the nine measures. All the measures used in these parameters for the Lower and Upper case are below, the called search space. Temperature values are based on experimental values, $T_{h,exp}$ e $T_{c,exp}$.

Measures	Seebeck Coefficient (S)	Internal Resistance (R)	T_h	T_c
1 to 6	0 - 5	0 - 5	$T_{h,exp} \pm 1$	$T_{c,exp} \pm 1$

Table 4 – Search Space. The choice of F and CR (i.e. the mutation factor and crossover ratio) allows a better tradeoff between convergence time and accuracy of the fittings.

2.4   Results and discussion

The parabolic solar concentrator was tested in a standard sunny day with some clouds appearing eventually. Figure 5 shows registered temperatures at concentration focus together with Sun radiation obtained from the university weather station. It can be seen a strong correlation between in focus measured temperatures with the available sun radiation, being indicative that we have carefully focused and positioned the sun concentrator during the day.
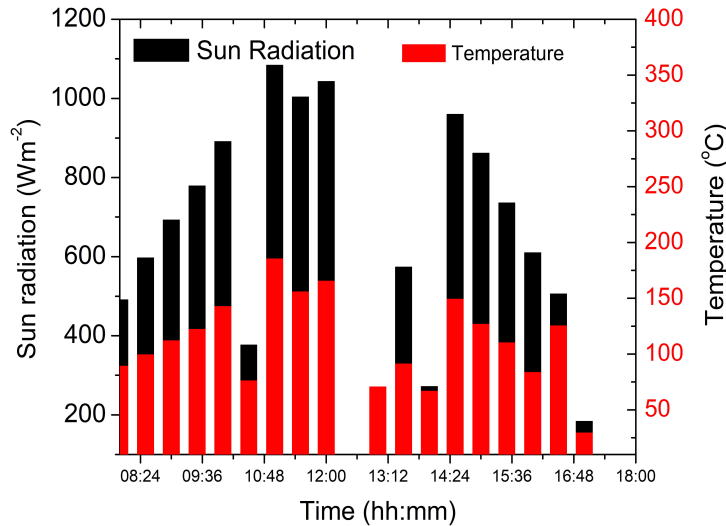
Figure 5 – Weather data collected from university weather station during a typical measurement day. Left y-axis stands for sun radiation in black and right axis for the temperature measured in the focus of the first parabolic concentrator in red (color online).

After testing the first cylindrical-parabolic collector regarding its ability to reach high temperatures we proceeded IV measurements for various temperature gradient conditions. Many measurements were carried out and we selected six of them to be analyzed which are listed in Table 5. Temperature gradients are within the range of 52 °C and 109 °C. These measurements were taken considering irradiation conditions within Figure 5 data.

In Figure 6 we present our experimental data with fittings extrapolated to both

Measurement	$T_h(°C)$	$T_c(°C)$	$\triangle T(°C)$	Sun Radiation(Wm^{-2})
1	90	38	52	640
2	95	38	57	680
3	108	38	70	693
4	118	37	81	753
5	128	38	90	865
6	138	29	109	966

Table 5 – Measurement list with hot, cold and temperature gradients together with measured sun radiation power.
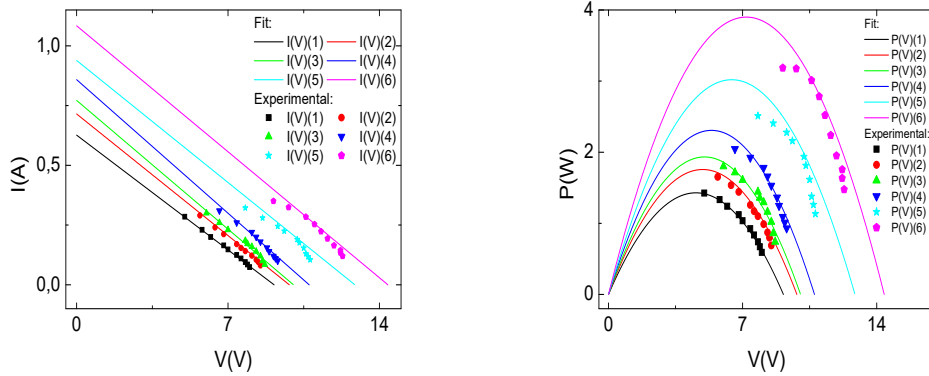
Figure 6 – Experimental data for IV characteristics (dots) and power P(V) (dots) and fitted data (lines of same colors) extrapolated to the limits V = 0 V with I = I_{sc} and I = 0 with V = V_{oc} for the collector system. Data corresponds to Table 4 in the order: (a) IV measurements 1 to 6, (b) P(V) measurements 1 to 6.

limits (0V, I_{sc}) and (V_{oc},0). Dots (line) stand for experimental data (fittings) of IV and power P(V) data. Colors and symbols correspond to numbered measurement being black and square, red and circle, green and upper triangle, navy and down triangle, cyan and star, and magenta and pentagon for measurements 1 to 6 respectively. In-field measurements were limited to a narrow voltage range and presented some fluctuations that were properly dealt by carrying fittings under the applied differential evolution algorithm. For higher temperature gradients, data seems to be nonlinear but this is a thermodynamic effect of not being able to assure the same temperature at all device surface points when you're far from equilibrium. As can be identified in Table 6, fitting error of parameters were kept under acceptable limits. Besides, simultaneous fittings of both IV and P(V) actually carried by considering I(R_L), V(R_L) and P(R_L) with R_L determined by the ratio V/(NI) (see Equation 2.3 were absolutely necessary to keep consistency of the data. Even though IV is practically linear and P(V) parabolic, From Equations 2.1 to 2.5 it can be seen that it is a hard task to isolate variables since they are interdependent. This task, carried by the differential evolution algorithm, gave consistent data with excellent

convergence for S, R. Temperature were allowed to variate since in practice it is not homogeneously distributed, but errors around 0.5 K are compatible with those natural fluctuations.

	S(mVK^{-1})	R(Ω)	T$_h$(°C)	T$_c$(°C)
1	0.17	0.01435	90.1 $\pm$ 0.4	38.0 $\pm$ 0.5
2	0.17	0.01354	95.2 $\pm$ 0.4	37.9 $\pm$ 0.5
3	0.14	0.01279	108.0 $\pm$ 0.4	37.9 $\pm$ 0.5
4	0.13	0.01233	118.0 $\pm$ 0.5	37.1 $\pm$ 0.5
5	0.14	0.01348	128.0 $\pm$ 0.4	38.1 $\pm$ 0.5
6	0.13	0.01307	137.9 $\pm$ 0.4	29.0 $\pm$ 0.4

Table 6 – Search Space Results. The four first parameters from left are fitting results and the two others measures fitting quality. S, R here are considered as the mean value for a single pn junction unit inside a module.

In Table 7 we present other important parameters necessary to evaluate the performance of the Solar concentrator, namely Short circuit current I$_{sc}$, open circuit voltage V_{oc}, maximum power point P_{max} which is the maximum power that could be delivered to a load, followed by corresponding voltage and current at this point. Other parameters Z_{eff} which is a measure of the overall thermoelectric performance of a material/junction, ρ its electrical resistivity. The last two parameters are the theoretical limit of the efficiency of a perfect Carnot machine η_c and the solar concentrator efficiency operating at the maximal power point η_{max}. See Equations 2.8 to 2.14 for details. The results indicate a low power generation when compared to the performance of commercially available photovoltaic solar cells, however its important to mention that besides being a technology in its early stages of development if compared to photovoltaic technology, it also harvest most of the energy in the electromagnetic spectrum region which photovoltaic technology does not absorb energy. Under this scenario the top efficiency of 6.20% obtained for sample 6 is worth to mention as better than some organic and flexible photovoltaic modules [37].

	I_{sc}(A)	V_{oc}(V)	P_{max}(W)	V(P_{max})	I(P_{max})	Z_{eff}(K^{-1})	ρ(mΩ m)	η_c(%)	η_{max}(%)
1	0.623 ± 0.015	9.08 ± 0.22	1.41705	4.98603	0.28420	0.0026	2.59 ± 0.12	57.9 ± 0.5	3.08 ± 0.03
2	0.712 ± 0.017	9.80 ± 0.24	1.70229	5.78436	0.29429	0.0026	2.38 ± 0.11	60.2 ± 0.6	3.37 ± 0.04
3	0.767 ± 0.007	9.96 ± 0.09	1.84646	6.07695	0.30385	0.0026	2.22 ± 0.04	64.9 ± 0.5	4.08 ± 0.04
4	0.854 ± 0.007	10.69 ± 0.08	2.15226	6.76922	0.31795	0.0026	2.09 ± 0.03	68.6 ± 0.4	4.67 ± 0.04
5	0.933 ± 0.007	12.79 ± 0.09	2.78702	8.21655	0.33920	0.0026	2.27 ± 0.03	70.2 ± 0.4	5.15 ± 0.04
6	1.084 ± 0.006	14.39 ± 0.08	3.49064	9.52663	0.36641	0.0026	2.10 ± 0.02	79.0 ± 0.3	6.20 ± 0.05

Table 7 – Calculated parameters from the fitting data and model.

η_{max} is a calculated theoretical value, being a maximum allowed thermodynamic limit. To calculate the value of the real efficiency, we use the Equation 2.6 and 2.7 with w = 0.00324 m, B = 0.0016 m^2 and κ = 1.5 Wm^{-1}K^{-1}. The result of the power generated by each module and the efficiency is presented in Table 8.

	P(W)	η (%)
1	0.1771	0.46
2	0.2127	0.50
3	0.2308	0.44
4	0.2690	0.45
5	0.3483	0.52
6	0.4363	0.54

Table 8 – Value of power generated by each module and actual efficiency.

The suggestion for the didactic laboratory classes is the formation of small groups of up to six physics undergraduate students for setup and carrying out the measurements of the experiment. Such activity must consider technological aspects involved on heat energy harvesting using semiconductor devices as well as clean energy generation. Besides, students are expected to analyze experimental data with the development of graphical analysis and fitting with python algorithm models made available by the professor for extracting the relevant parameters as exposed in this work.

2.5 Conclusions

We have built and analyzed a solar concentration for energy harvesting using TEG technology based on eight Peltier cooler modules and parabolic mirrors. The developed setup was built with standard workshop materials aiming simplicity, robustness and also easy to handle. In this way it is suitable for physics or renewable energy experimental classes at undergraduate or even high school levels. Measurements were carried outdoor by students using a handheld wattmeter using university weather station to monitor climate conditions during the experiment day and using a potentiometer as load. (V,I,P) datapoints were verified by the professor in charge of the class and subject to differential evolution algorithm fittings simultaneous V,I,P as a function of the load resistance in order to obtain maximal consistency and accurate parameter extraction. Considering the best temperature gradient of 109 °C we obtained an efficiency of 6.20% as the thermodynamic limit for direct conversion from heat to electric power. This is an excellent result considering that thermoelectric generation technology by the use of semiconductor thermoelectric properties is still under development. It is possible, by the use of other materials and concentrating more the sun radiation to achieve higher temperatures to reach even higher power generation. However those materials are hard to find commercially and have high costs which are not necessary as a proof of concept of the generator system.

Thus, considering the advantage of simplicity and ease of construction our TEG shows as a good alternative to harvest heat energy as well as direct sun heat as demonstrated.

Acknowledgments

References

1 ALVARADO, R. et al. Do economic development and human capital decrease non-renewable energy consumption? evidence for OECD countries. *Energy*, Elsevier BV, v. 215, p. 119147, jan. 2021. Disponível em: <https://doi.org/10.1016/j.energy.2020.119147>. 39

2 ZAFOSCHNIG, L. A.; NOLD, S.; GOLDSCHMIDT, J. C. The race for lowest costs of electricity production: Techno-economic analysis of silicon, perovskite and tandem solar cells. *IEEE Journal of Photovoltaics*, Institute of Electrical and Electronics Engineers (IEEE), v. 10, n. 6, p. 1632–1641, nov. 2020. Disponível em: <https://doi.org/10.1109/jphotov.2020.3024739>. 39

3 MONTECUCCO, A.; SIVITER, J.; KNOX, A. R. The effect of temperature mismatch on thermoelectric generators electrically connected in series and parallel. *Applied Energy*, Elsevier BV, v. 123, p. 47–54, jun. 2014. Disponível em: <https://doi.org/10.1016/j.apenergy.2014.02.030>. 39

4 YIN, J.; MOLINI, A.; PORPORATO, A. Impacts of solar intermittency on future photovoltaic reliability. *Nature Communications*, Springer Science and Business Media LLC, v. 11, n. 1, set. 2020. Disponível em: <https://doi.org/10.1038/s41467-020-18602-6>. 39, 58

5 DORSEY-PALMATEER, R. Effects of wind power intermittency on generation and emissions. *The Electricity Journal*, Elsevier BV, v. 32, n. 3, p. 25–30, abr. 2019. Disponível em: <https://doi.org/10.1016/j.tej.2019.02.007>. 39, 58

6 NELSON, J. *The Physics of Solar Cells*. PUBLISHED BY IMPERIAL COLLEGE PRESS AND DISTRIBUTED BY WORLD SCIENTIFIC PUBLISHING CO., 2003. Disponível em: <https://doi.org/10.1142/p276>. 39, 58

7 SUHERMAN, S. et al. Water and heat-sink cooling system for increasing the solar cell performances. *EAI Endorsed Transactions on Energy Web*, European Alliance for Innovation n.o., v. 0, n. 0, p. 161050, jul. 2018. Disponível em: <https://doi.org/10.4108/eai.13-7-2018.161050>. 39, 58

8 TAWIL, S. N. M.; ZAINAL, M. Z. Energy harvesting using TEG and PV cell for low power application. In: . Author(s), 2018. Disponível em: <https://doi.org/10.1063/1.5022935>.

9   SINGH, B. et al. DESIGN AND CONSTRUCTION OF a SIMPLE THERMOELEC-TRIC GENERATOR HEAT EXCHANGER FOR POWER GENERATION FROM SA-LINITY GRADIENT SOLAR POND. *Jurnal Teknologi*, Penerbit UTM Press, v. 76, n. 5, set. 2015. Disponível em: <https://doi.org/10.11113/jt.v76.5527>. 40, 59

10   SINGH, M.; NIRAPURE, S.; MISHRA, A. Thermoelectric generator: A review. *IOSR Journal of Mechanical and Civil Engineering*, v. 12, n. 3, p. 40–45, 2015. 40, 59

11   ZHENG, X. et al. A review of thermoelectrics research – recent developments and potentials for sustainable and renewable energy applications. *Renewable and Sustainable Energy Reviews*, Elsevier BV, v. 32, p. 486–503, abr. 2014. Disponível em: <https://doi.org/10.1016/j.rser.2013.12.053>. 40

12   TRAVADI, S.; DABHI, J. Review on design and analytical model of thermoelectric generator. *International Journal of Scientific Research*, 2012. 41

13   ELARUSI, A. H. et al. Theoretical approach to predict the performance of thermoe-lectric generator modules. *Journal of Electronic Materials*, Springer Science and Business Media LLC, v. 46, n. 2, p. 872–881, out. 2016. Disponível em: <https://doi.org/10.1007/s11664-016-4948-9>.

14   NARDUCCI, D. Do we really need high thermoelectric figures of merit? a critical appraisal to the power conversion efficiency of thermoelectric materials. *Applied Physics Letters*, AIP Publishing, v. 99, n. 10, p. 102104, set. 2011. Disponível em: <https://doi.org/10.1063/1.3634018>.

15   Nganyang Paul Bayendang et al. A comprehensive thermoelectric generator (teg) modelling. Zenodo, 2020. Disponível em: <https://zenodo.org/record/4289574>.

16   SNYDER, G. J.; SNYDER, A. H. Figure of merit ZT of a thermoelectric device defined from materials properties. *Energy & Environmental Science*, Royal Society of Chemistry (RSC), v. 10, n. 11, p. 2280–2283, 2017. Disponível em: <https://doi.org/10.1039/c7ee02007d>.

17   FERNANDES, A. A.; FILHO, G. L. T.; RODRIGUES, M. R. B. *Desenvolvimento de um sistema concentrador heliotermoelétrico de efeito Seebeck*. 2020. 43, 61

18   FÉBBA, D. et al. The effects of noises on metaheuristic algorithms applied to the PV parameter extraction problem. *Solar Energy*, Elsevier BV, v. 201, p. 420–436, maio 2020. Disponível em: <https://doi.org/10.1016/j.solener.2020.02.093>.

19   STORN, R.; PRICE, K. *Journal of Global Optimization*, Springer Science and Business Media LLC, v. 11, n. 4, p. 341–359, 1997. Disponível em: <https://doi.org/10.1023/a:1008202821328>.

20 RAMLI, M. A.; BOUCHEKARA, H.; ALGHAMDI, A. S. Optimal sizing of PV/wind/diesel hybrid microgrid system using multi-objective self-adaptive differential evolution algorithm. *Renewable Energy*, Elsevier BV, v. 121, p. 400–411, jun. 2018. Disponível em: <https://doi.org/10.1016/j.renene.2018.01.058>.

21 BEIRAMI, H.; SHABESTARI, A. Z.; ZERAFAT, M. M. Optimal PID plus fuzzy controller design for a PEM fuel cell air feed system using the self-adaptive differential evolution algorithm. *International Journal of Hydrogen Energy*, Elsevier BV, v. 40, n. 30, p. 9422–9434, ago. 2015. Disponível em: <https://doi.org/10.1016/j.ijhydene.2015.05.114>.

22 SUN, C.-H. et al. Comparison of dynamic differential evolution and self-adaptive dynamic differential evolution for buried metallic cylinder. *Research in Nondestructive Evaluation*, Informa UK Limited, v. 24, n. 1, p. 35–50, jan. 2013. Disponível em: <https://doi.org/10.1080/09349847.2012.699607>.

23 KUMAR, D. N.; RAJU, K. S. Editorial: Evolutionary algorithms in water resources. *H2Open Journal*, IWA Publishing, v. 3, n. 1, p. 390–391, jan. 2020. Disponível em: <https://doi.org/10.2166/h2oj.2020.001>. 44

24 DAS, S.; MULLICK, S. S.; SUGANTHAN, P. Recent advances in differential evolution – an updated survey. *Swarm and Evolutionary Computation*, v. 27, p. 1–30, 2016. ISSN 2210-6502. Disponível em: <https://www.sciencedirect.com/science/article/pii/S2210650216000146>.

25 ELSAYED, S.; SARKER, R. Differential evolution framework for big data optimization. *Memetic Computing*, Springer Science and Business Media LLC, v. 8, n. 1, p. 17–33, jan. 2016. Disponível em: <https://doi.org/10.1007/s12293-015-0174-x>. 45

26 SHIN, D. H. et al. Enhancement of efficiency and stability in organic solar cells by employing MoS2 transport layer, graphene electrode, and graphene quantum dots-added active layer. *Applied Surface Science*, Elsevier BV, v. 538, p. 148155, fev. 2021. Disponível em: <https://doi.org/10.1016/j.apsusc.2020.148155>. 49

3 Concentrated Solar Power with thermoelectric generator - an approach using the Cross-Entropy optimization method

To continue the study of a solar power concentrator, we now apply another optimization method, called CE (*Cross-Entropy*). The article was published in the Energies.

Graphical Abstract
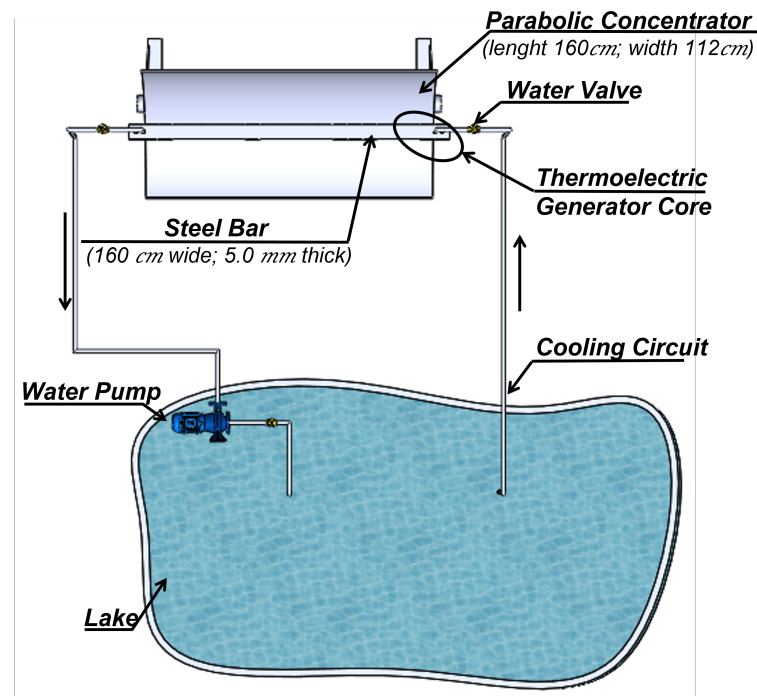
Figure 7 – Graphical Abstract of Publication 2

Abstract

In this research, a CSP as a PTC (*Parabolic Trough Collector*), using Peltier cooling modules for power generation was analyzed by the Cross-Entropy method. When comparing conventional solar electric generators with this system, we have the advantage that it is compact and lightweight and can be easily assembled and used as low-cost power generation equipment. For this system, we perform IV measurements and use fit models in order to accurately extract the model parameters. This is all in a standalone, robust

and simultaneous fit of three equations, through the global optimization method called CE. This is a robust method that had never been applied to extract parameters in a thermoelectric generation.

Keywords

Concentrated Solar Power • Parabolic Trough Collector • Seebeck Effect • Cross-Entropy • Optimization Method • Efficiency

3.1 Introduction

The world is going through a transition. The energy sector is transforming to be more sustainable, safe, and economical in the future [5]. One of the pillars of this transition is renewable energy, and it is fueled by unprecedented public pressure and political action, triggered by the United Nations Sustainable Development Goals, increasing air pollution and water stress, as well as growing concerns about climate change. Innovation is a key factor and the energy sector is evolving even further [10].

Rapid declines in renewable energy costs, particularly for wind and solar generation, have boosted the energy sector, which is leading the ongoing energy transition [4]. As an example, between the years 2010 and 2018, prices fell sharply. PVSC modules decreased by 90%, and the LCOE (*Levelized Cost of Energy*) of solar photovoltaic energy decreased by 77%. The per-unit price of wind turbines has halved over the same period, and the LCOE of onshore wind electricity has dropped by nearly 30%, with further dramatic drops expected over the next decade [9].

The energy sector transition and falling prices are accelerated by three main innovation trends: 1) digitalization, 2) decentralization, and 3) electrification. These trends are shifting paradigms, roles, and responsibilities, opening doors to new players in the industry, and freeing up system flexibility for a high share of VRE (*Variable Renewable Energy*) penetration. In this article, we propose to make a contribution to the construction of knowledge in the number one trend, digitization.

Digitization can be defined as the conversion of data into value for the power sector. The application of digital monitoring and control technologies in the power generation and transmission domains has been a major trend for several decades and has recently started to penetrate more deeply into power systems. The wider use of smart meters and sensors, the application of the Internet of Things, and the use of large amounts of data with artificial intelligence have created opportunities to provide new services to the system [2, 3].
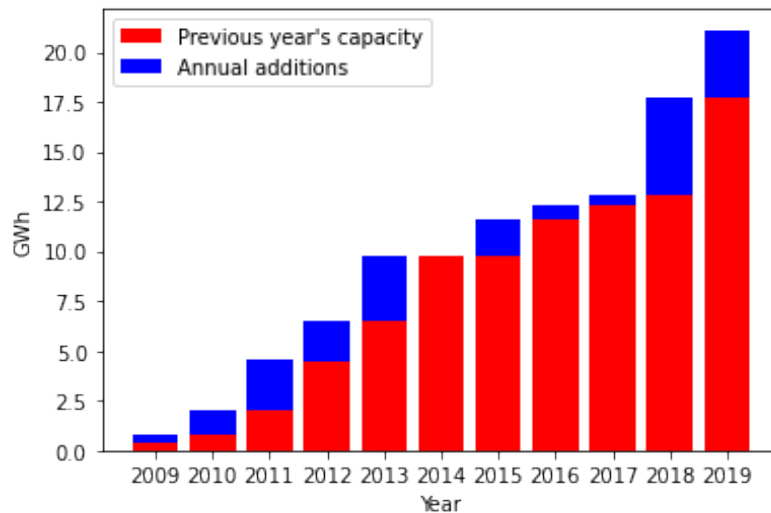
Figure 8 – CSP Thermal Energy Storage Global Capacity and Annual Additions, 2009-
2019 [12].

There are several technologies used for the use of renewable energies, including
PVSC, Wind, Biomass, and CSP, which will be the subject of study here.

CSP is a viable form of power generation with many power plants and variable
forms of power generation scattered throughout the world [6]. CSP technologies focus heat
in one area to produce the high temperatures required to make electricity. Since the solar
radiation that reaches the Earth is so spread out and diluted, it must be concentrated to
produce the high temperatures required to generate electricity. There are several types of
technologies that use mirrors or other reflecting surfaces to concentrate the sun's energy
up to 2.000 times its normal intensity [11].

PTC use long reflecting troughs that focus the sunlight onto a pipe located at the
focal line. The first parabolic-trough system was developed in 1912 in Cairo, Egypt [8]. A
fluid circulating inside the pipe collects the energy and transfers it to a heat exchanger,
which produces steam to drive a turbine. One of the world's largest parabolic trough
power plants is located in the Mojave Desert in California. This collection of plants has
a total generating capacity of 354 MW, one-third the size of a large nuclear power plant
[7].

Global CSP capacity grew 11% in 2019 to 6.2 GW, with 600 MW of capacity
coming online. This was down from the 700 MW commissioned in 2018 and well below
the average annual increase (24%) of the past decade. However, CSP continued to spread
to new markets, and more than 1.1 GW of additional capacity was under construction at
year's end, as seen in the Figure 8.

To deal with intermittency associated with PVSC [16] and wind power generation,
[17] limits of radiation absorption spectral range [18] and also efficiency decreases due to
temperature effects on PVSC [19], the use of the TEG alone or in association with PVSC

technology must be considered. One remarkable advantage of TEGs against PVSC is that it generates energy more effective under cloudy weather [57] since long wavelength radiation is less subject to being contained by clouds being an effective form to cope with PVSC intermittency.

TEG Technology is based on a single effect that is the Seebeck effect. Seebeck effect is caused by the diffusion of carriers from the hot to the cold side of the sample building a difference of potential between them [47, 48].

With proper adaptations, CSP can be used with heat storage, allowing its use for power generation even at night or in cloudy environments. Also, according to Singh et al. [21], the association of CSP with TEG technology is advantageous since it allows power generation without mechanical parts such as electrical generators, and capacitors among other components, being noiseless, reliable, and environment friendly. For this, TEGs convert heat energy from a temperature gradient that established a small voltage in the opposite terminals a pn junction of a thermoelectric material due to the Seebeck effect [22]. A TEG module is composed of more than a hundred such junctions.

To analyze TEG measurements, it is important to consider a proper theoretical background [43, 44, 45, 46, 49]. For a TEG device, power is derived from thermodynamics first law considering internal power dissipation RI^2 or as a function of load resistance, as shown in Equation 3.1.

$$P = NI[S(T_h - T_c) - RI] = NI^2R_L \tag{3.1}$$

where N stands for several pn junctions, S is the Seebeck coefficient, I the current through the TEG, R its internal resistance, T_h e T_c are the temperatures from the hot and cold sides respectively, and R_L is the load resistance.

Using an Equation 3.1 we get the voltage across the load resistance (Equation 3.2) and the current (Equation 3.3).

$$V = NI[S(T_h - T_c) - RI]. \tag{3.2}$$

$$I = \frac{S(T_h - T_c)}{R_L + R}. \tag{3.3}$$

Here, we can see that the current is not a function of the number of pn junctions.

Applying Equations 3.2 and 3.3, we can write the power in the form presented in Equation 3.4.

$$P = \frac{NS^2(T_h - T_c)^2}{R} \frac{R_L/R}{(1 + R_L/R)^2}. \tag{3.4}$$

Considering the heat equation, thermal efficiency is the ratio between the output power and the heat absorbed from the hot side

$$\eta = \frac{P}{\phi},$$ (3.5)

where the power per modulus P is $P_{max}/8$ and the heat flux ϕ is

$$\phi = \frac{\kappa B \Delta T}{w},$$ (3.6)

where w the thickness, the surface area and κ is the thermal conductivity. The Equation 3.5 can be rewritten as

$$\eta = \frac{\left(1 - \frac{T_c}{T_h}\right)\frac{R_L}{R}}{\left(1 + \frac{R_L}{R}\right) - \frac{1}{2}\left(1 - \frac{T_c}{T_h}\right)\frac{\left(1+\frac{R_L}{R}\right)^2 \frac{T_c}{T_h}}{ZT_c}},$$ (3.7)

where $ZT_c = \frac{S^2 T_c}{\kappa \rho}$ and the ρ is electrical resistivity. It is also important to consider a comparison with the thermal efficiency of an ideal Carnot machine given by

$$\eta_c = 1 - \frac{T_c}{T_h}.$$ (3.8)

The maximum efficiency is obtained with $R_L = R$, so that

$$\eta_{max} = \left(1 - \frac{T_c}{T_h}\right)\frac{\sqrt{1 + Z\bar{T}} - 1}{\sqrt{1 + Z\bar{T}} + \frac{T_c}{T_h}},$$ (3.9)

where $\bar{T}$ is the average temperature between the hot and cold junction temperatures and the maximum power equation is

$$P_{max} = \frac{NS^2(T_h - T_c)^2}{4R}.$$ (3.10)

Finally, the effective resistivity is

$$\rho = \frac{4P_{max}A/L}{N(I_{max})^2},$$ (3.11)

and the effective Z-factor is

$$Z_{eff} = \frac{1}{\bar{T}}\left[\left(\frac{1 + \frac{T_c \eta_{max}}{T_h \eta_c}}{1 - \frac{\eta_{max}}{\eta_c}}\right)^2 - 1\right].$$ (3.12)
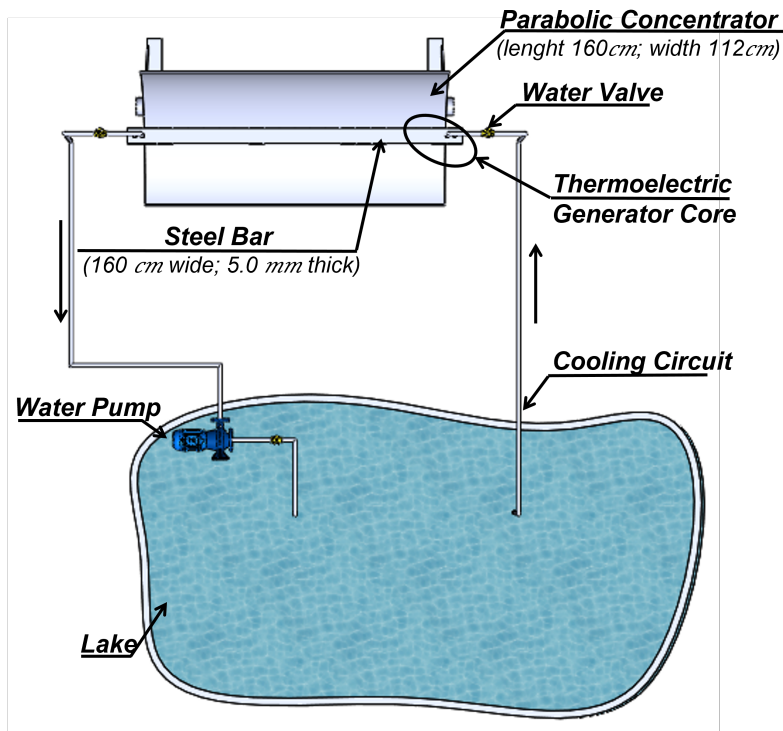
Figure 9 – Schematics of the generator setup of the cylindrical-parabolic collector with dimensions. Main parts are indicated on the Figure.

Thus, this work consists of the experimental measurements of IV characteristics of a parabolic solar concentrator with Peltier modules in its focus and its subsequent analysis by a cross-entropy optimization method considering here presented equations. In the following, we will describe our experimental setup and methods.

3.2   Materials and Methods

For this work, we analyzed a CSP whose patent was registered in [38]. An iron bar was designed and fixed to the sides of the CSP so that it is above, along the center of the parabolic axis. Eight TECs, Danvic brand, model HC-40-15.4, were placed at the bottom of the bar. These TECs had the hot side facing down, towards the center. The cold side was up, fixed to the iron bar. Inside the iron bar there is a stream of water, which comes directly from the side. This flow of water inside the iron bar causes the side of the TEC that is in contact with it to stay cool as well. This schematic is shown in Figure 9.

The lake used for this experiment is large, has a large mass of water, so its temperature remains constant. Two type K thermocouples were used to measure temperatures. One of them measured the temperature of the cold side, the contact between the iron bar and the TEC, called T_c, and the other measured the hot temperature, the side of the TEC that was facing the center of the CSP, called T_h, the side that will receive the sun's rays concentrated by the reflecting parabola.

A portable Reed Instruments DW-6060 watt meter was used to measure electrical output power. With it we were able to measure voltage, current and power and a precision potentiometer of 100 kΩ. As the measurements were carried out far from the laboratory, these instruments were the most indicated because of the battery. Current-voltage data were collected with a constant temperature gradient along each measurement. The measured current I and voltage V give us directly the power P and the load resistance R_L calculated according to Equation 3.2.

3.3   The Cross-Entropy optimization method

The CE method is an interactive optimization method that applies to continuous and discrete problems. It minimizes the entropy between the distribution of solutions in the objective function, choosing the best sample for the next interaction. The CE was introduced by Rubinstein [39] to estimate the probability of rare events in stochastic and discrete optimization networks. The CE has been applied to several optimization problems, such as alignment of DNA sequences [40], adjustments of isochrones in open clusters [43, 44], thickness estimation in thin films [41] and electronic mobility in semiconductors [42], showing a robust method for the solution of parameter estimation. The CE uses sampling concepts, being a technique of reduction of variance, but that does not require a priori knowledge of the parameters regarding distribution. The CE consists of a simple adaptive procedure for estimating parameters. Furthermore, the CE procedure is based on a solution space, with an evolutionary rule in which a fraction of the space is selected in each iteration based on some selection criteria.

Each CE method interaction follows these steps:

1. Initial sample generation of the set of parameters to be estimated through normal distributions, following the rule

$$v_n^j = N(\mu^j, \sigma^j, n), \tag{3.13}$$

where N is a normal distribution centered between the pre-specified physical intervals μ^j, is the number of entities of the distribution, which in this research were adopted 100 entities, j is the number of parameters to be adjusted, which here is equal to 4 and σ^j is the variation of the distribution of solutions that are initially adopted between the pre-specified lower and upper physical limits;

2. Select 10% of the best solutions, v_{best}^j based on the negative logarithm of likelihood. For this, a comparison occurs through an objective function between the experimental data of power, current, and voltage, with the models obtained through the Equations 3.2, 3.3, and 3.4;

3. Random generation of a new distribution of parameters using the values of v_{best}^j to generate the center of the distribution, μ and for the variation of the distribution, σ, following the rule:

$$\mu^j = \alpha\mu(v_{best}^j) + (1-\alpha)\mu(v_{best}^j), \qquad (3.14)$$

$$\sigma^j = \alpha\sigma(v_{best}^j) + (1-\alpha)\sigma(v_{best}^j, \qquad (3.15)$$

where $\mu(v_{best}^j)$ is the mean value of the distribution v_{best}^j for each parameter j and $\sigma(v_{best}^j)$ the standard deviation. The α parameter determines the convergence speed for the solution and doesn't allow the method to get stuck in a local minimum;

4. The method returns to the first for until a pre-specified criterion is satisfied.

In this work, we opted for a random resampling of the data. For that, we used the Bootstrap [45] technique, which is a repetition technique in which some experimental data are removed and randomly added in order to make the procedure in which it was inserted more robust. In this work, the data were resampled 50 times, producing good statistics on the parameters found.

3.4   Discussion

The equipment was adjusted and tested for its ability to reach high temperatures and we chose a rolled-up day for the experiment. Several measurements of IV curves were performed and for our analyses, we highlight six of them. The measurements are shown in the Table 9 along with the temperature gradients, which are between 52° C and 109° C.

The experimental data with the respective adjustments of our experiment are shown in Figure 10. Measured values are represented by dots and adjustments by lines.

The data collected in the field were limited to a small voltage range and showed some fluctuations. They were treated under the CE optimization method. These measurements are difficult to perform and the same temperature cannot be guaranteed at all points on the device's surface, so the data appear non-linear for higher temperature gradients, however, it is just a thermodynamic effect due to variation.

Parameter adjustment errors were kept within acceptable limits, as can be seen in Table 10. The ratio V/(NI), Equation 3.2, determines the value of R_L and with that we make the simultaneous adjustments of IV and P(V), because, for this, we consider I(R_L), V(R_L).
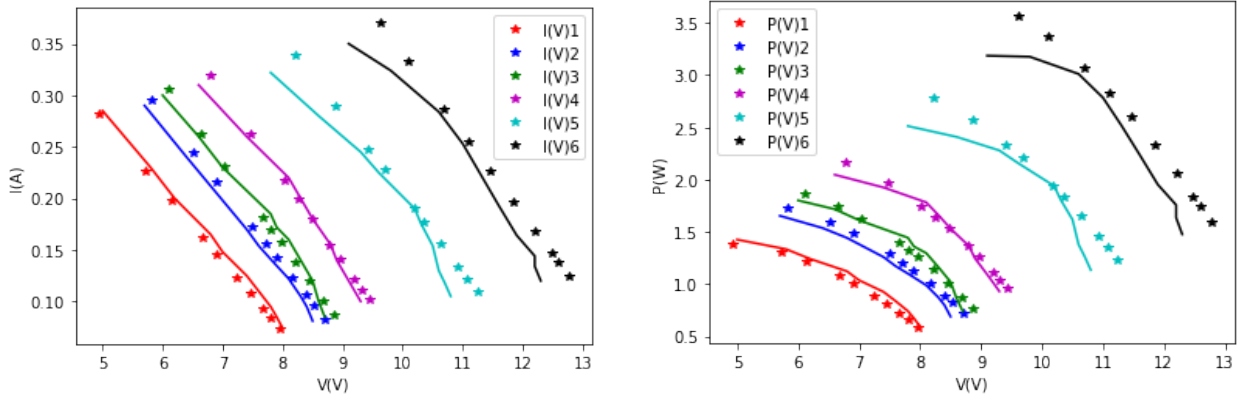
Figure 10 – Experimental data for IV characteristics (dots) and power P(V) (dots) and fitted data (lines of same colors) for the collector system. Data corresponds to Table 9 in the order: (a) IV measurements 1 to 6, (**b**) P(V) measurements 1 to 6.

From the graphs it can be seen that IV is almost linear and P(V) is parabolic. If we look at the Equation 3.1 until the Equation 3.4, we will notice that the variables are interdependent, therefore, difficult to be isolated. The Cross-Entropy method, applied here, worked with excellent convergence for S, R.

In the Table 11 we present relevant parameters to analyze the performance of the CSP. In them we have short-circuit current I_{sc}, open-circuit voltage V_{oc}, maximum power point P_{max}, voltage at maximum power point V(P_{max}) and current at maximum power point I(P_{max}).

The thermoelectric performance is presented by Z_{eff}, the effective Figure of Merit, and the electrical resistivity by ρ.

The last two parameters related to CSP efficiency. One is the theoretical limit η_c of the efficiency of a perfect Carnot engine and the other η_{max} the efficiency of the CSP at the maximum power point.

If we compare the performance of commercial PVSC, the CSP power generation results are low, however, two things need to be remembered. First, that CSP is a technology in its early stages of development, when compared to PVSC technology. Second, it captures most of the energy in a region of the electromagnetic spectrum where PVSC technology does not absorb energy.

η_{max} is a calculated theoretical value, being a maximum allowed thermodynamic limit. To calculate the value of the real efficiency, we use the Equation 3.5 and 3.6 with w = 0.00324 m, B = 0.0016 m^2 and κ = 1.5 Wm^{-1}K^{-1}. The result of the power generated by each module and the efficiency is presented in Table 12.

These results show us a good behavior of the Concentrated Solar Power with the use of thermoelectric generators and, mainly, the robustness of the applied mathematical

method, the Cross-Entropy, which obtained results consistent with those already presented in the literature, thus showing an excellent alternative for application in the energy sector, especially in this case for a thermoelectric generation.

3.5   Conclusions

We have analyzed a CSP for energy harvesting using TEG technology based on eight Peltier cooler modules and parabolic mirrors with the CE optimization method. Voltage, current, and power (V,I,P) datapoints were subject to CE optimization method fittings simultaneous V,I,P as a function of the load resistance to obtain maximal consistency and accurate parameter extraction. Considering the best temperature gradient of 109° C we obtained an efficiency of 6.20% as the thermodynamic limit for direct conversion from heat to electric power. This is an excellent result considering that thermoelectric generation technology by the use of semiconductor thermoelectric properties is still under development. The proposed mathematical optimization method, CE, for analysis proved to be very robust, presenting results consistent with those already presented in the literature, thus proving to be an excellent alternative for application in the energy sector, especially in this case for a thermoelectric generation.

The use of this simple construction and maintenance mechanism, using TECs and a metallic mirror, is promising for the generation of clean and environmentally sustainable energy. In addition, through the CE optimization method, it is possible to find the temperature range in which the system presents better performance, helping in the construction project of other systems of different dimensions.

Table 9 – Measurement list with hot, cold and temperature gradients together with measured sun radiation power.

Measurement	$T_h(°C)$	$T_c(°)$	$\Delta T(°C)$	Sun Radiation (Wm^{-2})
1	90	38	52	640
2	95	38	57	680
3	108	38	70	693
4	118	37	81	753
5	128	38	90	865
6	138	29	109	966

Table 10 – Search Space Results. The four first parameters from left are fitting results and the two others measures fitting quality. S, R here are considered as the mean value for a single pn junction unit inside a module.

	$S(mVK^{-1})$	$R(\Omega)$	$T_h(°C)$	$T_c(°C)$
1	0.17	0.0143 ± 0.0003	90.0 ± 0.3	37.5 ± 0.2
2	0.17	0.0134 ± 0.0003	94.9 ± 0.4	38.1 ± 0.4
3	0.14	0.0124 ± 0.0009	107.9 ± 0.3	38.1 ± 0.3
4	0.13	0.0117 ± 0.0009	117.9 ± 0.3	37.1 ± 0.3
5	0.14	0.0126 ± 0.0016	128.0 ± 0.3	38.1 ± 0.3
6	0.13	0.0128 ± 0.0011	137.9 ± 0.2	29.1 ± 0.2

Table 11 – Calculated parameters from the fitting data and model.

	$\mathbf{I}_{sc}$ (A)	$\mathbf{V}_{oc}$ (V)	$\mathbf{P}_{max}$ (W)	V (P_{max})	I (P_{max})	$\mathbf{Z}_{eff}$ ($\mathbf{K}^{-1}$)	ρ ($m\Omega$)m	η_c (%)	η_{max} (%)
1	0.63 ± 0.01	9.06 ± 0.07	1.38849	4.93554	0.28133	0.0026	2.52 ± 0.10	58.3 ± 0.3	3.11 ± 0.02
2	0.72 ± 0.02	9.78 ± 0.16	1.72117	5.81634	0.29592	0.0026	2.37 ± 0.14	59.9 ± 0.4	3.35 ± 0.03
3	0.79 ± 0.06	9.95 ± 0.18	1.86300	6.10410	0.30521	0.0026	2.13 ± 0.32	64.7 ± 0.3	4.07 ± 0.02
4	0.89 ± 0.07	10.65 ± 0.13	2.16587	6.79059	0.31895	0.0026	1.92 ± 0.29	68.5 ± 0.3	4.67 ± 0.03
5	0.98 ± 0.13	12.50 ± 0.50	2.78694	8.21642	0.33919	0.0026	2.10 ± 0.60	70.2 ± 0.2	5.14 ± 0.02
6	1.09 ± 0.10	14.20 ± 0.40	3.55976	9.62048	0.37002	0.0026	2.10 ± 0.40	78.9 ± 0.2	6.20 ± 0.02

Table 12 – Value of power generated by each module and actual efficiency.

	P(W)	η (%)
1	0.1736	0.45
2	0.2151	0.51
3	0.2329	0.45
4	0.2707	0.45
5	0.3484	0.52
6	0.4450	0.55

References

1 Fernandes, A., Rubinger, R., Ider, J., Oliveira, A., Tiago-Filho, G. & Baldissera, M. Characterization of a solar concentration thermoelectric generator. *European Journal Of Physics.* **42**, 065103 (2021,10), https://doi.org/10.1088/1361-6404/ac2937

2 Xu, Q., Zhong, M. & Li, X. How does digitalization affect energy? International evidence. *Energy Economics.* **107** pp. 105879 (2022) 57

3 Bernabé-Moreno, J. When digitalization becomes an essential part of our energy transition. *Digitale Welt.* **6**, 8-13 (2022) 57

4 Luderer, G., Madeddu, S., Merfort, L., Ueckerdt, F., Pehl, M., Pietzcker, R., Rottoli, M., Schreyer, F., Bauer, N., Baumstark, L. & Others Impact of declining renewable energy costs on electrification in low-emission scenarios. *Nature Energy.* **7**, 32-42 (2022) 57

5 Olabi, A. & Abdelkareem, M. Renewable energy and climate change. *Renewable And Sustainable Energy Reviews.* **158** pp. 112111 (2022) 57

6 Noč, L. & Jerman, I. Review of the spectrally selective (CSP) absorber coatings, suitable for use in SHIP. *Solar Energy Materials And Solar Cells.* **238** pp. 111625 (2022) 58

7 Gharat, P., Bhalekar, S., Dalvi, V., Panse, S., Deshmukh, S. & Joshi, J. Chronological development of innovations in reflector systems of parabolic trough solar collector (PTC)-A review. *Renewable And Sustainable Energy Reviews.* **145** pp. 111002 (2021) 58

8 Ummadisingu, A. & Soni, M. Concentrating solar power–technology, potential and policy in India. *Renewable And Sustainable Energy Reviews.* **15**, 5169-5175 (2011) 58

9 Irena, I. Renewable power generation costs in 2017. Report. *International Renewable Energy Agency, Abu Dhabi.* (2018) 57

10 Irena Innovation landscape for a renewable-powered future: solutions to integrate variable renewables. (International Renewable Energy Agency Abu Dhabi, United Arab Emirates,2019) 57

11 Islam, M., Huda, N., Abdullah, A. & Saidur, R. A comprehensive review of state-of-the-art concentrating solar power (CSP) technologies: Current status and research trends. *Renewable And Sustainable Energy Reviews.* **91** pp. 987-1018 (2018) 58

12 Murdock, H., Gibb, D., André, T., Sawin, J., Brown, A., Appavou, F., Ellis, G., Epp, B., Guerra, F., Joubert, F. & Others Renewables 2020-Global status report. (2020) 9, 58

13 Alvarado, R., Deng, Q., Tillaguango, B., Méndez, P., Bravo, D., Chamba, J., Alvarado-Lopez, M. & Ahmad, M. Do economic development and human capital decrease non-renewable energy consumption? Evidence for OECD countries. *Energy*. **215** pp. 119147 (2021,1), https://doi.org/10.1016/j.energy.2020.119147 39

14 Zafoschnig, L., Nold, S. & Goldschmidt, J. The Race for Lowest Costs of Electricity Production: Techno-Economic Analysis of Silicon, Perovskite and Tandem Solar Cells. *IEEE Journal Of Photovoltaics*. **10**, 1632-1641 (2020,11), https://doi.org/10.1109/jphotov.2020.3024739 39

15 Montecucco, A., Siviter, J. & Knox, A. The effect of temperature mismatch on thermoelectric generators electrically connected in series and parallel. *Applied Energy*. **123** pp. 47-54 (2014,6), https://doi.org/10.1016/j.apenergy.2014.02.030 39

16 Yin, J., Molini, A. & Porporato, A. Impacts of solar intermittency on future photovoltaic reliability. *Nature Communications*. **11** (2020,9), https://doi.org/10.1038/s41467-020-18602-6 39, 58

17 Dorsey-Palmateer, R. Effects of wind power intermittency on generation and emissions. *The Electricity Journal*. **32**, 25-30 (2019,4), https://doi.org/10.1016/j.tej.2019.02.007 39, 58

18 Nelson, J. The Physics of Solar Cells. (Imperial College,2003,5), https://doi.org/10.1142/p276 39, 58

19 Suherman, S., Sunarno, A., Hasan, S. & Harahap, R. Water and heat-sink cooling system for increasing the solar cell performances. *Endorsed Transactions On Energy Web*. pp. 161050 (2018,7), https://doi.org/10.4108/eai.13-7-2018.161050 39, 58

20 Tawil, S. & Zainal, M. Energy harvesting using TEG and PV cell for low power application. (Author(s),2018), https://doi.org/10.1063/1.5022935 40, 59, 79

21 Singh, B., Saoud, A., Remeli, M., Ding, L., Date, A. & Akbarzadeh, A. Desing and construction of a simple thermoelectric generator heat exchanger for power generation from salinity gradient solar pond. *Jurnal Teknologi*. **76** (2015,9), https://doi.org/10.11113/jt.v76.5527 40, 59

22 Singh, M., Nirapure, S. & Mishra, A. Thermoelectric generator: a review. *Journal Of Mechanical And Civil Engineering*. **12**, 40-45 (2015) 40, 59

23 Zheng, X., Liu, C., Yan, Y. & Wang, Q. A review of thermoelectrics research – Recent developments and potentials for sustainable and renewable energy applications. *Renewable And Sustainable Energy Reviews*. **32** pp. 486-503 (2014,4), https://doi.org/10.1016/j.rser.2013.12.053 40

24 Travadi, S. & Dabhi, J. Review on design and analytical model of thermoelectric generator. *International Journal Of Scientific Research.* (2012) 41

25 Elarusi, A., Fagehi, H., Lee, H. & Attar, A. Theoretical approach to predict the performance of thermoelectric generator modules. *J. Electron. Mater.* **46**, 872-881 (2016,10), https://doi.org/10.1007/s11664-016-4948-9 41, 59, 76

26 Narducci, D. Do we really need high thermoelectric figures of merit? A critical appraisal to the power conversion efficiency of thermoelectric materials. *Applied Physics Letters.* **99**, 102104 (2011,9), https://doi.org/10.1063/1.3634018 41, 59, 76

27 Bayendang, N., Kahn, M., Balyan, V., Draganov, I. & Pasupathi, S. A comprehensive thermoelectric generator (TEG) modelling. (Zenodo,2020), https://zenodo.org/record/4289574 41, 59, 76

28 Snyder, G. & Snyder, A. Figure of merit ZT of a thermoelectric device defined from materials properties. *Energy & Environmental Science.* **10**, 2280-2283 (2017), https://doi.org/10.1039/c7ee02007d 41, 59, 76

29 Fébba, D., Bortoni, E., Oliveira, A. & Rubinger, R. The effects of noises on metaheuristic algorithms applied to the PV parameter extraction problem. *Solar Energy.* **201** pp. 420-436 (2020,5), https://doi.org/10.1016/j.solener.2020.02.093 44, 77

30 Storn, R. & Price, K. undefined. *Journal Of Global Optimization.* **11**, 341-359 (1997), https://doi.org/10.1023/a:1008202821328 44, 77

31 Ramli, M., Bouchekara, H. & Alghamdi, A. Optimal sizing of PV/wind/diesel hybrid microgrid system using multi-objective self-adaptive differential evolution algorithm. *Renewable Energy.* **121** pp. 400-411 (2018,6), https://doi.org/10.1016/j.renene.2018.01.058 44, 77

32 Beirami, H., Shabestari, A. & Zerafat, M. Optimal PID plus fuzzy controller design for a PEM fuel cell air feed system using the self-adaptive differential evolution algorithm. *International Journal Of Hydrogen Energy.* **40**, 9422-9434 (2015,8), https://doi.org/10.1016/j.ijhydene.2015.05.114 44, 77

33 Sun, C., Chiu, C., Ho, M. & Li, C. Comparison of Dynamic Differential Evolution and Self-Adaptive Dynamic Differential Evolution for Buried Metallic Cylinder. *Research In Nondestructive Evaluation.* **24**, 35-50 (2013,1), https://doi.org/10.1080/09349847.2012.699607 44, 77

34 Kumar, D. & Raju, K. Editorial: Evolutionary Algorithms in Water Resources. *H2Open Journal.* **3**, 390-391 (2020,1), https://doi.org/10.2166/h2oj.2020.001 44

35 Das, S., Mullick, S. & Suganthan, P. Recent advances in differential evolution – An updated survey. *Swarm And Evolutionary Computation.* **27** pp. 1-30 (2016,4), https://doi.org/10.1016/j.swevo.2016.01.004 45, 77

36 Elsayed, S. & Sarker, R. Differential evolution framework for big data optimization. *Memetic Computing.* **8**, 17-33 (2016,1), https://doi.org/10.1007/s12293-015-0174-x 45

37 Shin, D., Jang, C., Ko, J. & Choi, S. Enhancement of efficiency and stability in organic solar cells by employing MoS2 transport layer, graphene electrode, and graphene quantum dots-added active layer. *Applied Surface Science.* **538** pp. 148155 (2021,2), https://doi.org/10.1016/j.apsusc.2020.148155 49

38 Assini Fernandes, A., Tiago Filho, G. & Baldissera Rodrigues, M. Desenvolvimento de um sistema concentrador heliotermoelétrico de efeito Seebeck. (2020,12) 43, 61

39 Rubinstein, R. Optimization of computer simulation models with rare events. *European Journal Of Operational Research.* **99**, 89-112 (1997,5), https://doi.org/10.1016/s0377-2217(96)00385-2 62

40 Keith, J. & Kroese, D. Sequence alignment by rare event simulation. *Proceedings Of The Winter Simulation Conference.* **1** pp. 320-327 (2002) 62

41 Zaccaro, S., Oliveira, A., Rubinger, R., Siqueira, C. & Costa Junior, R. Determination of thickness and refractive index of SiO2 thin films using the cross-entropy global optimization method. *Research, Society And Development.* **10**, e326101019028 (2021,8), https://doi.org/10.33448/rsd-v10i10.19028 62

42 Oliveira, A., Rubinger, R., Monteiro, H., Rubinger, C., Ribeiro, G. & Oliveira, A. Main scattering mechanisms in InAs/GaAs multi-quantum-well: a new approach by the global optimization method. *Journal Of Materials Science.* **51**, 1333-1343 (2015,9), https://doi.org/10.1007/s10853-015-9451-9 62

43 Caetano, T., Dias, W., Lépine, J., Monteiro, H., Moitinho, A., Hickel, G. & Oliveira, A. The OPD photometric survey of open clusters I. Techniques, program details and first results of robust determination of the fundamental parameters. *New Astronomy.* **38** pp. 31-49 (2015,7), https://doi.org/10.1016/j.newast.2015.01.003 62

44 Oliveira, A., Monteiro, H., Dias, W. & Caetano, T. Fitting isochrones to open cluster photometric data. *Astronomy & Astrophysics.* **557** pp. A14 (2013,8), https://doi.org/10.1051/0004-6361/201321157 62

45 Efron, B. & LePage, R. Introduction to bootstrap. (Wiley & Sons, New York,1992) 63

46 Cheng, Y., Zeng, Z., Liu, T., Wang, Y., Rodrıguez-Gallegos, C., Liu, H., Liu, X., Thway, M., Khup, D., Khaing, A. & Others Amorphous CdO-In2O3 Electrode for Perovskite-based Bifacial and Tandem Photovoltaic Technologies with High Energy Production. *Solar RRL*.

47 Riffat, S. & Ma, X. Thermoelectrics: a review of present and potential applications. *Applied Thermal Engineering*. **23**, 913-935 (2003) 59

48 Nasu, J. & Naka, M. Spin Seebeck effect in nonmagnetic excitonic insulators. *Physical Review B*. **103**, L121104 (2021) 59

49 Mansoor, M., Mirza, A., Duan, S., Zhu, J., Yin, B. & Ling, Q. Maximum energy harvesting of centralized thermoelectric power generation systems with non-uniform temperature distribution based on novel equilibrium optimizer. *Energy Conversion And Management*. **246** pp. 114694 (2021) 59

50 Fernandes, A., Rubinger, R., Ider, J., Oliveira, A., Tiago-Filho, G. & Baldissera, M. Characterization of a solar concentration thermoelectric generator. *European Journal Of Physics*. **42**, 065103 (2021)

51 Ribeiro, L., Ider, J., Oliveira, A., Rubinger, R., Rubinger, C. & Oliveira, A. Investigation of electronic transport in InAs/GaAs samples. A study using the metaheuristic self-adaptive differential evolution method. *Physica B: Condensed Matter*. **621** pp. 413293 (2021,11), https://doi.org/10.1016/j.physb.2021.413293

4 Efficiency analysis of thermoelectric generators

With the algorithm already well studied and its effectiveness proven, we are now going to study thermoelectric materials. We start here with ready-made materials, commercial, thermoelectric devices.

This chapter presents a work developed by me where I used SADE again, but now in an analysis of TEG. An entire experimental setup was carried out, which had good control of the necessary parameters, and thus the necessary measurements were taken and then analyzed by the algorithm. This work was submitted to a Journal.

Graphical Abstract
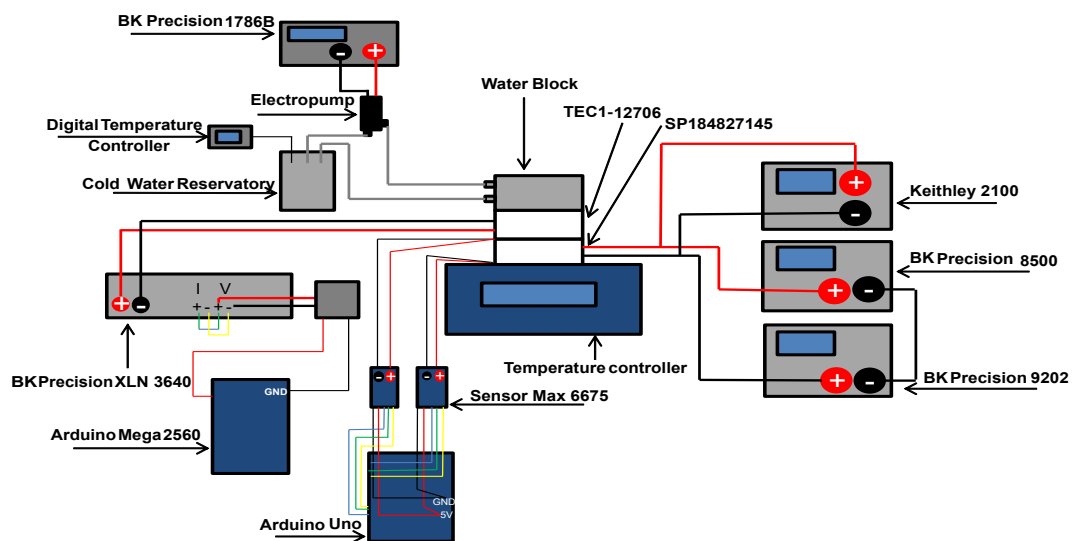
Figure 11 – Graphical Abstract of Publication 3

Highlights

- A new methodology for the characterization of thermoelectric devices.

- Extraction of parameters using the meta-heuristic Self-adaptative Differential Evolution method.

- Characterization of thermoelectric devices in a controlled temperature gradient.

Abstract

The negative environmental and economic impact, derived from the use of fossil fuels - oil, coal, gas, and other non-renewable sources of energy - has stimulated scientific research on clean and economically viable sources. Photovoltaics and wind power are intermittent sources which stimulates the quest for other energy sources. In this sense, a promising source of energy is made up of TEGs, which have the property of converting thermal energy into electrical energy, through the well-known Seebeck Effect. A new methodology for the characterization of these devices is presented in this work. For a robust analysis of the measures, the extraction of parameters is done through the meta-heuristic SADE. This is made possible by simultaneous fitting of three equations and five parameters in a consistent autonomous fashion. Besides a robust experimental setup which allows the generation and precise control of the temperature variable as electrical measurements, in a controlled environment, and a thorough statistical analysis is carried for eight TEGs, model SP-184827145 which gives the mean performance of the manufactured devices. The results obtained with low uncertainties indicates that this methodology is a reliable and low-cost option for the characterization of thermoelectric devices.

Keywords

Thermoeletric Generator ● Seebeck Effect ● Self-adaptative differential evolution ● Clean Energy

4.1 Introduction

Energy sources are a major concern and growing target for research throughout the scientific community and concern by government agencies, due to their great importance for the social and economic development of the population [1]. Since the economic development of a population is linked to the levels of energy consumption [2], this creates a need to use other options to replace the use of fossil fuels with alternative sources of renewable and sustainable energy [3, 4, 5, 6]. Besides, the main motivations are the reduction in reservoirs, fossil fuel price rises, and its impact on the environment.

In recent years, alternative and efficient renewable energy sources have been explored, such as, solar and wind power, which are already part of the energy generation system of several countries [7]. Among several technologies used from these sources, the generation of thermoelectric energy emerges as a great option, being green and clean, which occurs through the use of TEGs [8].

Thermoelectric energy can be generated with the use of TEGs, which are solid state devices. They operate by performing a direct conversion of thermal energy into

electrical energy [9]. They have many advantages, such as simple design, non-use of moving parts, greater longevity, without maintenance and operation costs, do not emit harmful pollutants during operation and do not contain chemicals, therefore, do not harm the environment [10, 11, 12, 13, 14].

The fabrication of TEGs can be done using different types of technology, a variety of manufacturing methods, and a plurality of materials in the function of the substrate such as silicon [15, 16, 17, 18], aluminum [19, 20, 21, 22, 23] and polymers [24, 25, 26].

Its applications are in diverse and very important areas. Some that we can mention are car engines [27, 28, 29, 30], industrial electronic devices [31, 32], micro powered wireless platforms [33, 34], health monitoring, tracking systems [35, 36, 37] and aerospace [38, 39].

TEGs are well-studied devices and present in the literature. A general and detailed overview of them was carried out by Nesrini [17], Sidique [40] and Patil [41]. Although these commercial modules are well studied, there is speculation that they may sometimes perform below the specified ratings [42]. This is also due to a difficult experimental analysis of such devices. The main issue is a the necessity of a measurement of three quantities namely electrical thermal conductivities and Seebeck's coefficient. Until recently the was no single setup for measure those quantities and calculate the Figure of Merit [58]. Also, our fitting procedure can lead to consistent values of five parameters considered in three distinct equations in a autonomous fashion, i.e. without any human interference during the process. The seeding of initial parameters and evolution rules are the sole human contribution to this process.

Because of these difficulties in presenting robustly the parameters that demonstrate the efficiency of thermoelectric devices, we present in this work a new methodology that proves to be more efficient. For this purpose, eight thermoelectric energy generators (TEGs) were used to perform measurements, through a new and efficient experimental arrangement, which generates and precisely controls a temperature gradient while performing electrical measurements. In addition, further analysis of these data is presented through a metaheuristic method, SADE, which presents a set of parameters that robustly describe the efficiency and functioning of the devices.

In summary this work tested the contributions of both the fitting method of the SADE algorithm together with a robust setup form the analysis of commercial thermoelectric generators. We also provide efficiency data in a similar fashion to photovoltaic devices which allows the comparison with other technologies. Our results could establish a new approach for characterizing commercial devices for the purpose of defining the optimal parameters and ratings for the datasheet of thermoelectric power generating commercial devices.

4.2   Review of thermoelectric devices

The modeling of the experimental data is done through the theoretical models of the TEGs [43, 44, 45, 46] and, in our analysis, we first looked at the power delivered by the device. This power is a function of the number of pn junctions N, Seebeck coefficient S, current I, hot temperature T_h, cold temperature T_c, internal resistance R and load resistance R_L. The power of the TEG does not depend directly on the current or the voltage and can be expressed as

$$W = \frac{NS^2(T_h - T_c)^2}{R} \frac{R_L/R}{(1 + R_L/R)^2}. \tag{4.1}$$

The voltage as a function of N is

$$V = \frac{NS(T_h - T_c)}{\frac{R_L}{R} + 1} \frac{R_L}{R}, \tag{4.2}$$

and the current is

$$I = \frac{S(T_h - T_c)}{R_L + R}. \tag{4.3}$$

Another important parameter for thermoelectric generators is their efficiency. One can calculate the thermal efficiency of an ideal Carnot machine, given by

$$\eta_c = 1 - \frac{T_c}{T_h}, \tag{4.4}$$

which can be compared with the thermal efficiency obtained from the ratio between the power and the heat absorbed by the hot part, which is presented in the Appendix, Equation 4.16.

Finally, we show here the expressions relative to the theoretically calculated effective quantities, important for TEG analysis. We have, first, the effective resistivity

$$\rho = \frac{4P_{max}A/L}{N(I_{max})^2}, \tag{4.5}$$

and the effective Z-factor

$$Z_{eff} = \frac{1}{\bar{\bar{T}}} \left[\left(\frac{1 + \frac{T_c \eta_{max}}{T_h \eta_c}}{1 - \frac{\eta_{max}}{\eta_c}} \right)^2 - 1 \right]. \tag{4.6}$$

All these quantities can be calculated at their maximum point. Expressions for P_{max}, , , η_{max} are given in the Appendix.

Thus, this work consists of the experimental measurements of a Thermoelectric Generator and its subsequent analysis robustly by the metaheuristic method named SADE considering the equations presented here. Next, we will describe the method used.

4.3 Materials and Methods

4.3.1 Differential Evolution Algorithm

GA are a particular type of evolutionary algorithms that use approaches derived from evolutionary biology such as heredity, mutation, natural selection and recombination [48]. They are like a computer simulation where a fixed amount of possible solutions, called a population, is evolved in search of better, more adapted solutions. This evolution starts from a population created randomly and goes through several mutations, or processes, through its generations. With each new generation, the new set of solutions is evaluated, and its adaptation to the environment is verified (in this case, the adaptation to some mathematical criteria previously established, called the objective function). The most adapted are then selected for the next generation, recombined, mutated, and form a new population. This new population is then used as an entry for the next iteration until a pre-defined criterion is established.

In this work, the experimental data collected were then analyzed according to a genetic algorithm, namely, the method of differential self-adaptive evolution [49, 50]. This algorithm, given the data provided in this study, provides us with the Seebeck coefficient values (S), internal resistance (R), and the hot and cold temperatures (T_h e T_c). From these data, and using the Equations 4.1-4.6, it is possible to calculate the short circuit current (I_{sc}), open-circuit voltage (V_{oc}), maximum power (P_{max}), resistivity (ρ), efficiency (η) and the effective Z-factor (Z_{eff}) of the TEG modules studied.

The metaheuristic method, called DE, was proposed by Storn and Price [51]. It had its development done quickly, already being effective for a large number of problems [52, 53, 54, 55], considering that at the beginning it was applied to solve systems of continuous variables, only [51]. One of these developments of the algorithm is its non-dependence on the control parameters, which made it self-adaptive [56], and for that reason, it received the name of Self-adaptive Differential Evolution.

For the application of the method in the calculation of the parameters of the thermoelectric generators it is important to consider their constitutive and intrinsic properties. These properties are L, the characteristic length of a single junction pn, A, the cross-sectional area, N, the number of junctions pn and Z, the Z-factor. These values are shown in the Table 13.

First, for the generation of solutions, a set of individuals is randomly generated.

Table 13 – Sample dimensional parameters, number of pn junctions and Z factor.

L (cm)	A (cm^2)	N	Z
0.2	0.01	128	0.00209

These individuals, potential solutions, will evolve over the generations. Each of these individuals is a candidate to be the best adapted to the environment, that is, to minimize the objective function, a mathematical criterion previously established. This initial population is obtained through the Equation 4.7

$$P_{i,j}^{G=1} = P_l^{G=1} + rand_{i,j}(0,1)(P_u^{G=1} - P_l^{G=1}), \tag{4.7}$$

where $rand_{ij}(0,1)$ is a random real number, which belongs to the range between 0 and 1. The index i represents the size of the population NP (in this case 100), and the index j, ranging from 1 to 4, the number of parameters studied, which are - as stated earlier - Seebeck coefficient (S), internal resistance (R) and hot and cold temperatures (T_h e T_c). P$_u$ and P$_l$ are the upper and lower limits that define the so-called search space. G represents each new generation of populations, ranging from 1 to G$_{max}$=50000, the value chosen for this study. Each P$_i$ is a candidate to be an optimal solution, the most adapted.

After the generation of the initial population, the mutation stage occurs, where a donor vector is generated, and obtained through the Equation 4.8

$$D_i^G = P_i^G + F(P_{best}^G - P_i^G) + F(P_{r1}^G - P_{r2}^G), \tag{4.8}$$

where D is the mutation vector that will select the tested individuals. (G, P$_i^G$) is the generation of individuals where P$_i^G$ represents the current individual. (P$_{r1}^G$ and P$_{r2}^G$) are chosen at random, exactly to be different from P$_i^G$. P$_{best}^G$ is the best individual, the most adapted, the one who minimizes the objective function f.

One of the self-adapting values in this algorithm is F, a real number, called a mutation factor and which belongs to the range (F$\epsilon[0,2]$). For each iteration, its value is adopted by the Equation 4.9

$$F_i^{G+1} = \begin{cases} F_l + rand_1 F_u, & \text{if } rand_2 < \tau_1, \\ F_i^G, & \text{otherwise.} \end{cases} \tag{4.9}$$

The next stage of evolution is called a crossover. It is defined by mixing the target vector P$_i^G$, produced by a vector T$_i^G$ between 0 and 1, and carries a comparison between

the crossover values as:

$$T_{i,j}^G = \begin{cases} D_{i,j}, & \text{if } rand(0,1)_j \leq C \text{ or } j = j_{rand}, \\ P_{i,j}^G, & \text{otherwise.} \end{cases}$$
(4.10)

Here, $D_{i,j}^G$ is the donor vector, j_{rand} is a random integer between 1 and 6 (size of the search space). CR is another self-adaptive factor in the algorithm. It is also a real number, now belonging to the range ($CR\epsilon[0,1]$) and called the crossover rate. It is defined by the Equation 4.11

$$CR_i^{G+1} = \begin{cases} rand_3, & \text{if } rand_4 < \tau_2, \\ CR_i^G, & \text{otherwise.} \end{cases}$$
(4.11)

In this equation, $rand_4$ is 4 random numbers between 0 and 1. τ_1 and τ_2 represent the probability of adjusting the mutation factor F and the crossover rate CR.

Finally, in the selection step, the temporary vector and the P_i^G vector are compared and the vector that minimizes the objective function is chosen, using the Equation **??**

$$P_i^{G+1} = \begin{cases} T_i^G, & \text{if } f(T_i) < f(P_i), \\ P_{i,j}^G, & \text{otherwise.} \end{cases}$$
(4.12)

This process is repeated until the end of the generations, or when some pre-defined criteria are satisfied. In the case of this work, the evolution of the solutions is finalized when reaching the 50000 generation. Thus, a simultaneous adjustment of the variables V, I, and W is made.

The parameters associated with the experimental curves are shown in the Tables 15 and 18, in the results section.

4.3.2 Experimental results

The measurements were taken at the LCM of the IFQ (*Institute of Physics and Chemistry*) of UNIFEI (*Federal University of Itajubá*). Eight Bismuth Telluride (Bi_2Te_3) TEGs, model SP-184827145 were used individually, to obtained better statistics. They withstands temperatures up to 200 °C, with length 40 mm, width 40 mm and height 3.4 mm, insulated with Teflon and connected with copper cables [57, 42].

Each TEG operates with a temperature gradient between its hot and cold sides which generates a voltage drop between those sides through the Seebeck effect. Since the generated voltage drop is proportional to the temperature gradient and the proportionality constant as the module's Seebeck coefficient, measurements needs to be carried

out through specific experimental setup comprising a power source (BK precision 9202) used to oppose the generated module's voltage, and electronic load (BK precision 8500) to dissipate the generated power and a voltmeter (Keithley 2100) to acquire module's voltage and current as IV characteristics as presented in Figure 12 and this defines the measurement circuit. However in order to produce reliable and stable results we developed a control system to be used together with the measuring circuit with the sole function to assure stable temperature gradient between hot and cold sides of the module.

Thus the remaining parts of the setup, used to control the TEG module's temperature were composed by a Microcomputer temperature controller, model UYUE 946S UY-D220V as the heat constant temperature source T_h (limited the control to up to 150 °C) with the hot TEG module's face placed in direct contact with the hot side of the UYUE 946S UY-D220V. The cold TEG module's face was put in contact with the cold side of a Peltier Thermoelectric Cooler TEC1-12706 to act as the constant cold temperature T_c. The TEC1-12706 however needs to be connected to a heat sink in order to keep T_c really stable. This is carried out by putting a metallic water block placed on the top of TEC1-12706 hot side and through which cold water circulates and removes the heat generated by the TEC1-12706 Peltier cooler. To finish the cold side control circuit, this water block was connected by hoses to a cold-water reservoir kept at cold with water and ice. The circulation of this water, between the reservoir and the water blocks, was made by a BF12 fine nozzle water pump, which was supplied with 5 V by a BK Precision 1786B source. The water temperature measurement was carefully monitored by a Digital Controller Temperature KT1210W.

The control of T_c is carried just by controlling the power driven to the TEC1-12706 Peltier cooler. The control of the voltage applied to the Peltier TEC was done through a standard PID (*Proportional Integral and Derivative*) routine developed in Python, which regulated the applied voltage and kept T$_c$ stable and constant throughout one IV measurement. This routine controlled a voltage output of an Arduino Mega 2560, through its PWM (*Pulse Width Modulation*) port which was in turn connected to the voltage outputs of a BK Precision XLN 3640 power supply that drives the TEC-12706 Peltier cooler. The pulsed PWM output needs to be converted to continuous voltage prior to its connection with the voltage control port of the XLN 3640 and this process is performed by a low-pass filter (built in the laboratory), connected to the Arduino Mega 2560 PWM port.

The characterization of the TEG's device and its generated power is carried out by IV measurements considering some fixed generated temperature gradients of 10 °C, 20 °C, 30 °C, 40 °C, 50 °C, 60 °C, 70 °C, 80 °C and 90 °C. The cold temperature T_c was kept at 20 °C. The measurements carried with the BK Precision 9202 Multi-Range DC Power Supply, BK Precision 8500 Programmable DC Electronic Load and digital multimeter Keithley 2100 6 1/2 Digit were controlled by a LabView program that changes the applied

voltage in 5 mV steps from 0 V to the open circuit voltage observed for each temperature gradient. Temperature T_c and T_h were also measured during experiments using two MAX 6675 Sensors, which use type K thermocouples. These measured the TEG's cold and hot temperatures. The MAX 6675 Sensors were connected to an Arduino Uno for data acquisition in the developed software.

For each of the eight TEGs, nine measurements were made, where gradients of approximately, 10 °C, 20 °C, 30 °C, 40 °C, 50 °C, 60 °C, 70 °C, 80 °C and 90 °C.
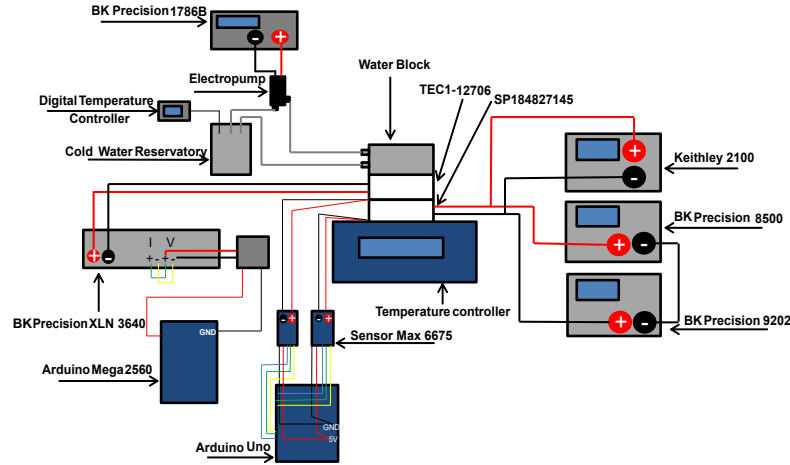
Figure 12 – Connection scheme used in the experimental apparatus for measuring curves IV.

For each of the seventy two measurements, SADE was used to analyze and extract parameters. The method was operated with an initial of 100 individuals for each parameter, evolving them for 50000 generations, and running each program 40 times, with a random initial population. For each set of 40 solutions, a statistical analysis was performed which provided us with the parameters of hot temperature T_h, cold temperature T_c, Seebeck coefficient S, resistance R from the studied model of Equations **??** to 4.6, short circuit current could be calculated I_{sc}, open-circuit voltage V_{oc}, maximum power P_{max}, voltage at maximum power $V(P_{max})$, current at maximum power $I(P_{max})$, resistivity ρ, Carnot efficiency η_c, maximum efficiency η_{max} and effective Z-factor Z_{eff}.

4.4   Results and discussion

Each TEG then had nine measurements, varying the temperature gradiente from 10 °C to 90 °C, with steps of 10 °C. With that, all the equivalent measures between the TEGs were used and statistical results of the parameters that determine the functioning of the TEGs are presented here. In Table 14 the results of measure 1 are presented, which refer to a statistical analysis of the measures with gradients of 10 °C of each TEG, measure 2 with gradients of 20 °C, successively up to the measure 9, which is the statistical analysis

of all measurements performed with a gradient of 90 °C. Thus, the Table 14 presents the median values of the temperature gradients $\Delta T(°C)$, Seebeck coefficient $S(\mu VK^{-1})$ and resistance $R(\Omega)$. Although the set of TEGs was acquired in the same batch, it is possible to verify a great variation in the values of the parameters, which confirms what was observed by Saim et al. [42].

In Table 15 we present medians of short circuit current values I_{sc}, open-circuit voltage V_{oc}, maximum power P_{max}, voltage at maximum power $V(P_{max})$ and current at maximum power $I(P_{max})$. The values are consistent with the experiment, increasing with increasing temperature gradient between the faces. However, we already see a noticeable difference here.

The values provided by the devices' datasheet are shown in Table 16. This shows, for a given temperature gradient, an associated open-circuit voltage.

A comparison is then made between the theoretical (provided by the datasheet) and the experimental (from our research) values of the open-circuit voltage for a given temperature gradient. A variation in these values is noted here, even for TEGs in the same batch. These data can be seen in Table 17. The experimental values is close to the theoretical V_{oc} but lower due to contact resistance or chemical potential mismatch between layers of the device.

The medians of the resistivity values ρ, Carnot efficiency η_c, maximum efficiency η_{max} and effective Z-factor Z_{eff} are shown in Table 18. The results obtained for the effective Z-factor of the devices were exactly those presented in the literature, without alteration for all the studied TEGs. Efficiency, as expected, increased with increasing temperature gradient, reaching 2.97 % for a gradient of 90 °C. Table 18 main message is of a fixed Z_{eff} with all the variations the second low of thermodynamics as in the operation of an idealized Carnot machine. The experimental errors or uncertainties are resulting from two statistical process: The first due to the fitting itself and the second from the behavior of eight distinct modules.

The Figure 13 presents the values of current per voltage and power per voltage showing the experimental results (in red) and those generated from the proposed model (in black). Curves 1, 2, 3, 4, 5, 6, 7, 8 and 9 represent, respectively, the values for the temperature gradients of 10 °C, 20 °C, 30 °C, 40 °C, 50 °C, 60 °C, 70 °C, 80 °C and 90 °C.

We see a linear behavior in the IV curves and, as you have larger temperature gradients, the experimental values fluctuate more. This is due to the TEG's behavior and the nature of the electrical measurement performed in this experiment. When generating a temperature gradient in the TEG, it provides a voltage value that passes through the load resistance, here represented by the electronic load BK precision 8500. This resistance, in

Table 14 – Medians of temperature gradients $\Delta T(°C)$, Seebeck coefficient $S(\mu VK^{-1})$ and resistance $R(\Omega)$.

	$\Delta T(°C)$	$S(\mu VK^{-1})$	$R(\Omega)$
1	11 ± 1	0.30 ± 0.03	0.01799
2	20 ± 1	0.33 ± 0.02	0.01929
3	30 ± 2	0.34 ± 0.02	0.02025
4	40 ± 1	0.35 ± 0.01	0.02145
5	50 ± 2	0.33 ± 0.01	0.02213
6	60 ± 2	0.35 ± 0.01	0.02468
7	71 ± 2	0.34 ± 0.01	0.02571
8	81 ± 2	0.34 ± 0.01	0.02679
9	94 ± 3	0.35 ± 0.01	0.02885

Table 15 – Medians of the short circuit current values I_{sc}, open-circuit voltage V_{oc}, maximum power P_{max}, voltage at maximum power $V(P_{max})$ and current at maximum power $I(P_{max})$.

	$I_{sc}(A)$	$V_{oc}(V)$	$P_{max}(W)$	$V(P_{max})$	$I(P_{max})$
1	0.17 ± 0.02	0.40 ± 0.06	0.01772	0.19793	0.08372
2	0.33 ± 0.02	0.84 ± 0.07	0.06988	0.42134	0.16674
3	0.49 ± 0.03	1.32 ± 0.08	0.15622	0.65083	0.24403
4	0.61 ± 0.03	1.71 ± 0.07	0.24890	0.84866	0.30622
5	0.73 ± 0.03	2.06 ± 0.09	0.37332	1.03186	0.36514
6	0.85 ± 0.03	2.61 ± 0.09	0.54331	1.30286	0.42071
7	0.94 ± 0.03	3.05 ± 0.11	0.68436	1.51865	0.46263
8	1.03 ± 0.04	3.49 ± 0.14	0.87320	1.75340	0.51318
9	1.10 ± 0.04	4.09 ± 0.15	1.08757	2.04016	0.55104

Table 16 – Values provided by the device's datasheet

$\Delta T(°C)$	$V_{oc}(V)$	$I(mA)$
20	0.97	225
40	1.8	368
60	2.4	469
80	3.6	558
100	4.8	669

Table 17 – Comparison between theoretical and experimental values of open-circuit voltage for temperature gradient data

$\Delta T(°C)$	$V_{oc}(V)$ theoretical	$V_{oc}(V)$ experimental
20	0.97	0.84 ± 0.07
40	1.8	1.71 ± 0.07
60	2.4	2.61 ± 0.09
80	3.6	3.49 ± 0.14

turn, makes this voltage pass back into the TEG, causing a disturbance in its temperature.

This same behavior is seen in Figure 13, on the P(V) curve, where there are greater oscillations in the experimental values for greater temperature gradients.
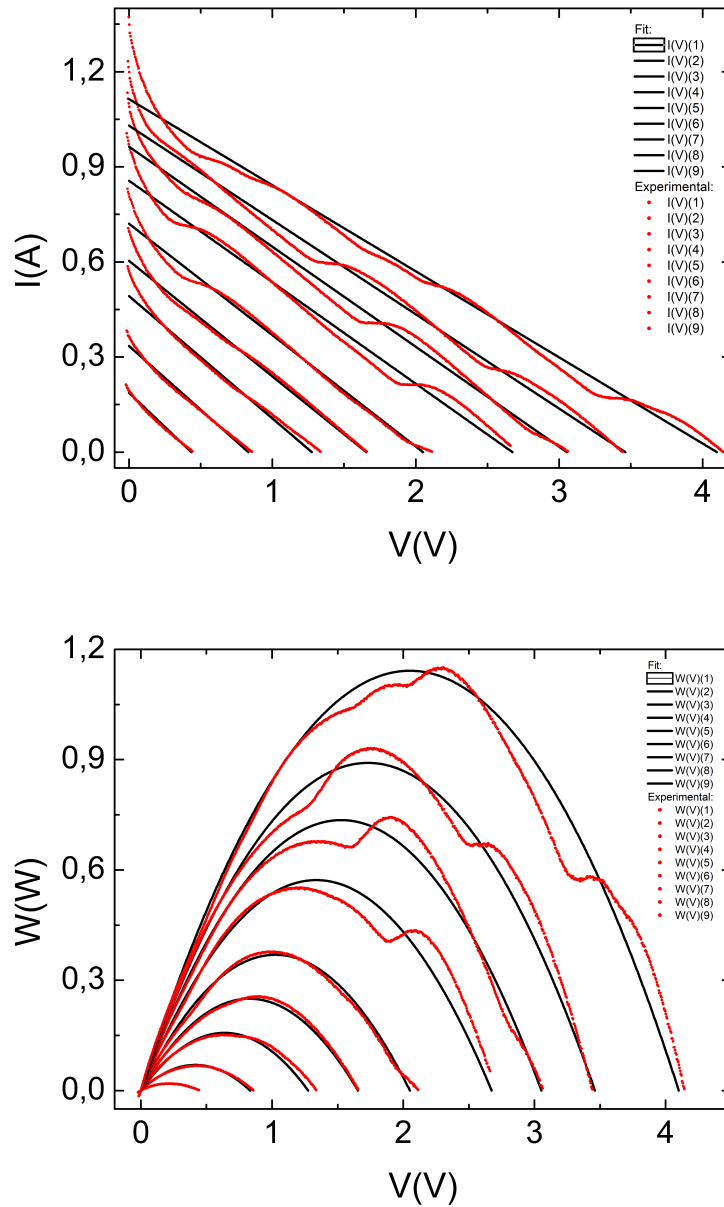
Figure 13 – (a) Current by voltage and (b) voltage power for experimental values (in red) and generated from the proposed model (in black). Curves 1, 2, 3, 4, 5, 6, 7, 8 and 9 represent, respectively, the values for the temperature gradients of 10 °C, 20 °C, 30 °C, 40 °C, 50 °C, 60 °C, 70 °C, 80 °C and 90 °C.

Analyzing the data presented in Figure 13, we see that the experimental arrangement created for this experiment was satisfactory. He fulfilled his goal of generating temperature gradients and controlling them, in addition to measuring them, a fact obser-

ved in the graphs (except the oscillations previously discussed). SADE's good behavior was also noted.

4.5 Summary and Conclusions

In this work we have presented a:

- new methodology for analyzing thermoelectric generating devices;

- new experimental arrangement, which generates and controls temperature gradients with precision, measures such temperatures, and also allow the precise determination of relevant associated electrical quantities.

The results from this assembly lead to acceptable statistical variations, compatible with the expected for commercial devices.

Together with this new experimental arrangement, we:

- applied a method of data analysis through a genetic algorithm of differential evolution for the first time, which presented excellent results and shows a new powerful tool for the analysis of thermoelectric materials.

The autonomous fitting process with simultaneous equations and parameters being analyzed lead to a successful method to obtain precise performance ratings of thermoeletric generators.

The TEGs studied, despite showing variations in their characteristics between elements of the same batch,

- behaved reliably, presenting a good thermal efficiency, from 2.97 % to a temperature gradient of 90 °C.

This evidence the robustness of the proposed methodology to define precisely relevant operation ratings for the commercial thermoelectric generators.

Appendix

Making R_L=R [47] we get the maximum quantities. Thus, the power described in the Equation 4.1 is

$$P_{max} = \frac{NS^2(T_h - T_c)^2}{4R},$$

(4.13)

while the current in Equation 4.3 is

$$I_{max} = \frac{S(T_h - T_c)}{2R} \tag{4.14}$$

and the voltage of the Equation 4.2

$$V_{max} = \frac{NS(T_h - T_c)}{2}. \tag{4.15}$$

The efficiency is

$$\eta = \frac{\left(1 - \frac{T_c}{T_h}\right) \frac{R_L}{R}}{\left(1 + \frac{R_L}{R}\right) - \frac{1}{2}\left(1 - \frac{T_c}{T_h}\right) \frac{\left(1 + \frac{R_L}{R}\right)^2 \frac{T_c}{T_h}}{ZT_c}}, \tag{4.16}$$

where ZT$_c = \frac{S^2 T_c}{\kappa \rho}$ is the Figure of Merit (ZT), κ the thermal conductivity, and ρ the electrical resistivity.

and the maximum efficiency

$$\eta_{max} = \left(1 - \frac{T_c}{T_h}\right) \frac{\sqrt{1 + Z\bar{T}} - 1}{\sqrt{1 + Z\bar{T}} + \frac{T_c}{T_h}}, \tag{4.17}$$

where $\bar{T}$ is the average temperature between the hot and cold sides, expressed by

$$\bar{T} = \frac{T_h + T_c}{2}. \tag{4.18}$$

Table 18 – Medians of the resistivity values ρ, Carnot efficiency η_c, maximum efficiency η_{max} and effective Z-factor Z_{eff}

	$\rho(\mathrm{m\Omega m})$	$\eta_c(\%)$	$\eta_{max}(\%)$	$Z_{eff}(\mathrm{K}^{-1})$
1	0.91 ± 0.24	53.35 ± 3.44	0.22 ± 0.04	0.00209
2	0.97 ± 0.16	94.85 ± 2.73	0.91 ± 0.09	0.00209
3	1.01 ± 0.11	94.75 ± 1.74	1.37 ± 0.09	0.00209
4	1.07 ± 0.09	91.05 ± 1.23	1.69 ± 0.08	0.00209
5	1.11 ± 0.09	92.45 ± 1.25	2.22 ± 0.10	0.00209
6	1.22 ± 0.09	87.75 ± 0.88	2.35 ± 0.09	0.00209
7	1.26 ± 0.10	86.45 ± 0.85	2.58 ± 0.10	0.00209
8	1.35 ± 0.12	80.50 ± 0.70	2.66 ± 0.10	0.00209
9	1.47 ± 0.13	76.25 ± 0.68	2.97 ± 0.11	0.00209

References

1 PANDIYARAJAN, V. et al. Experimental investigation on heat recovery from diesel engine exhaust using finned shell and tube heat exchanger and thermal storage system. *Applied Energy*, Elsevier BV, v. 88, n. 1, p. 77–87, jan. 2011. Disponível em: <https://doi.org/10.1016/j.apenergy.2010.07.023>. 74

2 SAIDUR, R. et al. Technologies to recover exhaust heat from internal combustion engines. *Renewable and Sustainable Energy Reviews*, Elsevier BV, v. 16, n. 8, p. 5649–5659, out. 2012. Disponível em: <https://doi.org/10.1016/j.rser.2012.05.018>. 74

3 XI, H.; LUO, L.; FRAISSE, G. Development and applications of solar-based thermoelectric technologies. *Renewable and Sustainable Energy Reviews*, Elsevier BV, v. 11, n. 5, p. 923–936, jun. 2007. Disponível em: <https://doi.org/10.1016/j.rser.2005.06.008>. 74

4 OMER, A. M. Focus on low carbon technologies: The positive solution. *Renewable and Sustainable Energy Reviews*, Elsevier BV, v. 12, n. 9, p. 2331–2357, dez. 2008. Disponível em: <https://doi.org/10.1016/j.rser.2007.04.015>. 74

5 AFSHAR, O. et al. A review of thermodynamics and heat transfer in solar refrigeration system. *Renewable and Sustainable Energy Reviews*, Elsevier BV, v. 16, n. 8, p. 5639–5648, out. 2012. Disponível em: <https://doi.org/10.1016/j.rser.2012.05.016>. 74

6 THIRUGNANASAMBANDAM, M.; INIYAN, S.; GOIC, R. A review of solar thermal technologies. Elsevier BV, v. 14, n. 1, p. 312–322, jan. 2010. Disponível em: <https://doi.org/10.1016/j.rser.2009.07.014>. 74

7 RITCHIE, H.; ROSER, M. Renewable energy. *Our World in Data*, 2020. Https://ourworldindata.org/renewable-energy. 74

8 ROWE, D. Thermoelectrics, an environmentally-friendly source of electrical power. *Renewable Energy*, Elsevier BV, v. 16, n. 1-4, p. 1251–1256, jan. 1999. Disponível em: <https://doi.org/10.1016/s0960-1481(98)00512-6>. 74

9 PROTO, A. et al. Thermal energy harvesting on the bodily surfaces of arms and legs through a wearable thermo-electric generator. *Sensors*, MDPI AG, v. 18, n. 6, p. 1927, jun. 2018. Disponível em: <https://doi.org/10.3390/s18061927>. 75

10 HE, W. et al. Recent development and application of thermoelectric generator and cooler. *Applied Energy*, Elsevier BV, v. 143, p. 1–25, abr. 2015. Disponível em: <https://doi.org/10.1016/j.apenergy.2014.12.075>. 75

11   RIFFAT, S.; MA, X. Thermoelectrics: a review of present and potential applications. *Applied Thermal Engineering*, Elsevier BV, v. 23, n. 8, p. 913–935, jun. 2003. Disponível em: <https://doi.org/10.1016/s1359-4311(03)00012-7>. 75

12   DAI, D.; ZHOU, Y.; LIU, J. Liquid metal based thermoelectric generation system for waste heat recovery. *Renewable Energy*, Elsevier BV, v. 36, n. 12, p. 3530–3536, dez. 2011. Disponível em: <https://doi.org/10.1016/j.renene.2011.06.012>. 75

13   TIE, S. F.; TAN, C. W. A review of energy sources and energy management system in electric vehicles. *Renewable and Sustainable Energy Reviews*, Elsevier BV, v. 20, p. 82–102, abr. 2013. Disponível em: <https://doi.org/10.1016/j.rser.2012.11.077>. 75

14   ULLAH, K. et al. A review of solar thermal refrigeration and cooling methods. *Renewable and Sustainable Energy Reviews*, Elsevier BV, v. 24, p. 499–513, ago. 2013. Disponível em: <https://doi.org/10.1016/j.rser.2013.03.024>. 75

15   YANG, M.-Z. et al. Energy harvesting thermoelectric generators manufactured using the complementary metal oxide semiconductor process. *Sensors*, MDPI AG, v. 13, n. 2, p. 2359–2367, fev. 2013. Disponível em: <https://doi.org/10.3390/s130202359>. 75

16   KAO, P.-H. et al. Fabrication and characterization of CMOS-MEMS thermoelectric micro generators. *Sensors*, MDPI AG, v. 10, n. 2, p. 1315–1325, fev. 2010. Disponível em: <https://doi.org/10.3390/s100201315>. 75

17   JAZIRI, N. et al. A comprehensive review of thermoelectric generators: Technologies and common applications. *Energy Reports*, Elsevier BV, v. 6, p. 264–287, dez. 2020. Disponível em: <https://doi.org/10.1016/j.egyr.2019.12.011>. 75

18   CHEN, Y.-W. et al. Fabrication and testing of thermoelectric CMOS-MEMS microgenerators with CNCs film. *Applied Sciences*, MDPI AG, v. 8, n. 7, p. 1047, jun. 2018. Disponível em: <https://doi.org/10.3390/app8071047>. 75

19   MARKOWSKI, P. M. Multilayer thick-film thermoelectric microgenerator based on LTCC technology. *Microelectronics International*, Emerald, v. 33, n. 3, p. 155–161, ago. 2016. Disponível em: <https://doi.org/10.1108/mi-05-2016-0038>. 75

20   MARKOWSKI, P. Thick-film photoimageable and laser-shaped arms for thermoelectric microgenerators. *Microelectronics International*, Emerald, v. 28, n. 3, p. 43–50, ago. 2011. Disponível em: <https://doi.org/10.1108/13565361111162620>. 75

21   MARKOWSKI, P.; DZIEDZIC, A. Planar and three-dimensional thick-film thermoelectric microgenerators. *Microelectronics Reliability*, Elsevier BV, v. 48, n. 6, p. 890–896, jun. 2008. Disponível em: <https://doi.org/10.1016/j.microrel.2008.03.008>. 75

22 MARKOWSKI, P.; STRASZEWSKI, L.; DZIEDZIC, A. Sandwich-type three-dimensional thick-film thermoelectric microgenerators. In: *2008 31st International Spring Seminar on Electronics Technology*. IEEE, 2008. Disponível em: <https://doi.org/10.1109/isse.2008.5276638>. 75

23 MARKOWSKI, P. Thermoelectric energy harvester fabricated in thick-film/LTCC technology. *Microelectronics International*, Emerald, v. 31, n. 3, p. 176–185, ago. 2014. Disponível em: <https://doi.org/10.1108/mi-11-2013-0077>. 75

24 HUU, T. N.; VAN, T. N.; TAKAHITO, O. Flexible thermoelectric power generator with y-type structure using electrochemical deposition process. *Applied Energy*, Elsevier BV, v. 210, p. 467–476, jan. 2018. Disponível em: <https://doi.org/10.1016/j.apenergy.2017.05.005>. 75

25 HASEBE, S. et al. Polymer based smart flexible thermopile for power generation. In: *17th IEEE International Conference on Micro Electro Mechanical Systems. Maastricht MEMS 2004 Technical Digest*. IEEE. Disponível em: <https://doi.org/10.1109/mems.2004.1290678>. 75

26 SUAREZ, F. et al. Flexible thermoelectric generator using bulk legs and liquid metal interconnects for wearable electronics. *Applied Energy*, Elsevier BV, v. 202, p. 736–745, set. 2017. Disponível em: <https://doi.org/10.1016/j.apenergy.2017.05.181>. 75

27 CRANE, D. T.; LAGRANDEUR, J. W. Progress report on BSST-led US department of energy automotive waste heat recovery program. *Journal of Electronic Materials*, Springer Science and Business Media LLC, v. 39, n. 9, p. 2142–2148, nov. 2009. Disponível em: <https://doi.org/10.1007/s11664-009-0991-0>. 75

28 ORR, B.; AKBARZADEH, A.; LAPPAS, P. An exhaust heat recovery system utilising thermoelectric generators and heat pipes. *Applied Thermal Engineering*, Elsevier BV, v. 126, p. 1185–1190, nov. 2017. Disponível em: <https://doi.org/10.1016/j.applthermaleng.2016.11.019>. 75

29 CAO, Q.; LUAN, W.; WANG, T. Performance enhancement of heat pipes assisted thermoelectric generator for automobile exhaust heat recovery. *Applied Thermal Engineering*, Elsevier BV, v. 130, p. 1472–1479, fev. 2018. Disponível em: <https://doi.org/10.1016/j.applthermaleng.2017.09.134>. 75

30 MOSTAFAVI, S. A.; MAHMOUDI, M. Modeling and fabricating a prototype of a thermoelectric generator system of heat energy recovery from hot exhaust gases and evaluating the effects of important system parameters. *Applied Thermal Engineering*, Elsevier BV, v. 132, p. 624–636, mar. 2018. Disponível em: <https://doi.org/10.1016/j.applthermaleng.2018.01.018>. 75

31 SOLBREKKEN, G.; YAZAWA, K.; BAR-COHEN, A. Thermal management of portable electronic equipment using thermoelectric energy conversion. In: *The Ninth Intersociety Conference on Thermal and Thermomechanical Phenomena In Electronic Systems (IEEE Cat. No.04CH37543)*. IEEE. Disponível em: <https://doi.org/10.1109/itherm.2004.1319185>. 75

32 ZHOU, Y.; PAUL, S.; BHUNIA, S. Harvesting wasted heat in a microprocessor using thermoelectric generators: Modeling, analysis and measurement. In: *2008 Design, Automation and Test in Europe*. IEEE, 2008. Disponível em: <https://doi.org/10.1109/date.2008.4484669>. 75

33 GUAN, M. et al. Design and experimental investigation of a low-voltage thermoelectric energy harvesting system for wireless sensor nodes. *Energy Conversion and Management*, Elsevier BV, v. 138, p. 30–37, abr. 2017. Disponível em: <https://doi.org/10.1016/j.enconman.2017.01.049>. 75

34 MUSLEH, M. A. et al. Thermoelectric generator experimental performance testing for wireless sensor network application in smart buildings. *MATEC Web of Conferences*, EDP Sciences, v. 120, p. 08003, 2017. Disponível em: <https://doi.org/10.1051/matecconf/201712008003>. 75

35 AMAR, A.; KOUKI, A.; CAO, H. Power approaches for implantable medical devices. *Sensors*, MDPI AG, v. 15, n. 11, p. 28889–28914, nov. 2015. Disponível em: <https://doi.org/10.3390/s151128889>. 75

36 TORFS, T. et al. Body-heat powered autonomous pulse oximeter. In: *2006 5th IEEE Conference on Sensors*. IEEE, 2006. Disponível em: <https://doi.org/10.1109/icsens.2007.355497>. 75

37 THIELEN, M. et al. Human body heat for powering wearable devices: From thermal energy to application. *Energy Conversion and Management*, Elsevier BV, v. 131, p. 44–54, jan. 2017. Disponível em: <https://doi.org/10.1016/j.enconman.2016.11.005>. 75

38 LIU, K. et al. Experimental prototype and simulation optimization of micro-radial milliwatt-power radioisotope thermoelectric generator. *Applied Thermal Engineering*, Elsevier BV, v. 125, p. 425–431, out. 2017. Disponível em: <https://doi.org/10.1016/j.applthermaleng.2017.07.022>. 75

39 YUAN, Z. et al. Screen-printed radial structure micro radioisotope thermoelectric generator. *Applied Energy*, Elsevier BV, v. 225, p. 746–754, set. 2018. Disponível em: <https://doi.org/10.1016/j.apenergy.2018.05.073>. 75

40 SIDDIQUE, A. R. M.; MAHMUD, S.; HEYST, B. V. A review of the state of the science on wearable thermoelectric power generators (TEGs) and their existing challenges.

Renewable and Sustainable Energy Reviews, Elsevier BV, v. 73, p. 730–744, jun. 2017. Disponível em: <https://doi.org/10.1016/j.rser.2017.01.177>. 75

41 PATIL, D. S.; ARAKERIMATH, R. R.; WALKE, P. V. Thermoelectric materials and heat exchangers for power generation – a review. *Renewable and Sustainable Energy Reviews*, Elsevier BV, v. 95, p. 1–22, nov. 2018. Disponível em: <https://doi.org/10.1016/j.rser.2018.07.003>. 75

42 MEMON, S.; TAHIR, K. Experimental and analytical simulation analyses on the electrical performance of thermoelectric generator modules for direct and concentrated quartz-halogen heat harvesting. *Energies*, MDPI AG, v. 11, n. 12, p. 3315, nov. 2018. Disponível em: <https://doi.org/10.3390/en11123315>. 75, 79, 82

43 ELARUSI, A. H. et al. Theoretical approach to predict the performance of thermoelectric generator modules. *Journal of Electronic Materials*, Springer Science and Business Media LLC, v. 46, n. 2, p. 872–881, out. 2016. Disponível em: <https://doi.org/10.1007/s11664-016-4948-9>. 41, 59, 76

44 NARDUCCI, D. Do we really need high thermoelectric figures of merit? a critical appraisal to the power conversion efficiency of thermoelectric materials. *Applied Physics Letters*, AIP Publishing, v. 99, n. 10, p. 102104, set. 2011. Disponível em: <https://doi.org/10.1063/1.3634018>. 41, 59, 76

45 Nganyang Paul Bayendang et al. A comprehensive thermoelectric generator (teg) modelling. Zenodo, 2020. Disponível em: <https://zenodo.org/record/4289574>. 41, 59, 76

46 SNYDER, G. J.; SNYDER, A. H. Figure of merit ZT of a thermoelectric device defined from materials properties. *Energy & Environmental Science*, Royal Society of Chemistry (RSC), v. 10, n. 11, p. 2280–2283, 2017. Disponível em: <https://doi.org/10.1039/c7ee02007d>. 41, 59, 76

47 KIM, H. S. et al. Relationship between thermoelectric figure of merit and energy conversion efficiency. *Proceedings of the National Academy of Sciences*, Proceedings of the National Academy of Sciences, v. 112, n. 27, p. 8205–8210, jun. 2015. Disponível em: <https://doi.org/10.1073/pnas.1510231112>. 85

48 GOLDBERG, D. E. *Genetic algorithms*. [S.l.]: Pearson Education India, 2006. 77

49 FÉBBA, D. et al. The effects of noises on metaheuristic algorithms applied to the PV parameter extraction problem. *Solar Energy*, Elsevier BV, v. 201, p. 420–436, maio 2020. Disponível em: <https://doi.org/10.1016/j.solener.2020.02.093>. 44, 77

50   BREST, J. et al. Self-adapting control parameters in differential evolution: A comparative study on numerical benchmark problems. *IEEE Transactions on Evolutionary Computation*, Institute of Electrical and Electronics Engineers (IEEE), v. 10, n. 6, p. 646–657, dez. 2006. Disponível em: <https://doi.org/10.1109/tevc.2006.872133>. 77

51   STORN, R.; PRICE, K. *Journal of Global Optimization*, Springer Science and Business Media LLC, v. 11, n. 4, p. 341–359, 1997. Disponível em: <https://doi.org/10.1023/a:1008202821328>. 44, 77

52   RAMLI, M. A.; BOUCHEKARA, H.; ALGHAMDI, A. S. Optimal sizing of PV/wind/diesel hybrid microgrid system using multi-objective self-adaptive differential evolution algorithm. *Renewable Energy*, Elsevier BV, v. 121, p. 400–411, jun. 2018. Disponível em: <https://doi.org/10.1016/j.renene.2018.01.058>. 44, 77

53   BEIRAMI, H.; SHABESTARI, A. Z.; ZERAFAT, M. M. Optimal PID plus fuzzy controller design for a PEM fuel cell air feed system using the self-adaptive differential evolution algorithm. *International Journal of Hydrogen Energy*, Elsevier BV, v. 40, n. 30, p. 9422–9434, ago. 2015. Disponível em: <https://doi.org/10.1016/j.ijhydene.2015.05.114>. 44, 77

54   SUN, C.-H. et al. Comparison of dynamic differential evolution and self-adaptive dynamic differential evolution for buried metallic cylinder. *Research in Nondestructive Evaluation*, Informa UK Limited, v. 24, n. 1, p. 35–50, jan. 2013. Disponível em: <https://doi.org/10.1080/09349847.2012.699607>. 44, 77

55   NANDI, S.; REDDY, M. J. Comparative performance evaluation of self-adaptive differential evolution with GA, SCE and DE algorithms for the automatic calibration of a computationally intensive distributed hydrological model. *H2Open Journal*, IWA Publishing, v. 3, n. 1, p. 306–327, jan. 2020. Disponível em: <https://doi.org/10.2166/h2oj.2020.030>. 77

56   DAS, S.; MULLICK, S. S.; SUGANTHAN, P. Recent advances in differential evolution – an updated survey. *Swarm and Evolutionary Computation*, v. 27, p. 1–30, 2016. ISSN 2210-6502. Disponível em: <https://www.sciencedirect.com/science/article/pii/S2210650216000146>. 45, 77

57   TAWIL, S. N. M.; ZAINAL, M. Z. Energy harvesting using TEG and PV cell for low power application. In: . Author(s), 2018. Disponível em: <https://doi.org/10.1063/1.5022935>. 40, 59, 79

58   Ider, J., Oliveira, A. & Rubinger, R. A Robust System for Thermoelectric Device Characterization. *IEEE Transactions On Instrumentation And Measurement* . **70** pp. 1-7 (2021) 75

5 A robust system for thermoelectric device characterization

One more step taken. With a well-established computational tool for data analysis and an experimental apparatus for measuring thermoelectric devices, we now need an apparatus that allows us to measure thermoelectric materials in bulk or thin films.

In this chapter we take a step further in the studies of thermoelectric materials. After applying a computational tool, the SADE algorithm, for three different scenarios, and carrying out a study of commercial thermoelectric devices, here we carry out the construction of an entire system for characterization of thermoelectric devices, such as in bulk state or in thin films.

The algorithm developed to control the equipment has been registered and the software registration certificate is in Annex B. The equipment has been patented and the patent registration is in Annex C. The article resulting from this work was published in the IEEE Institute of Electrical and Electronics Engineers (Instrumentation and Measurement Society) and presented in Global Experts Meet on Condensed Matter Physics, at Rome, Annex G.

Graphical Abstract

Highlights

- A new system for thermoelectric device characterization.

- Electrical conductivity, Seebeck coefficient, and thermal conductivity to obtain the Figure of Merit.

- Reduction of systematic errors through the use of single measuring equipment.

Abstract

Due to the large reduction in fossil fuel reservoirs, the consequent cost increase of deep water extraction, and the emission of pollutant, there is a constant search for alternative ways to obtain clean energy at lower cost. Among those sources we focus on the energy produced by thermoelectric materials. In this work we present a new system for the characterization of thermoelectric generation devices. Such a system performs
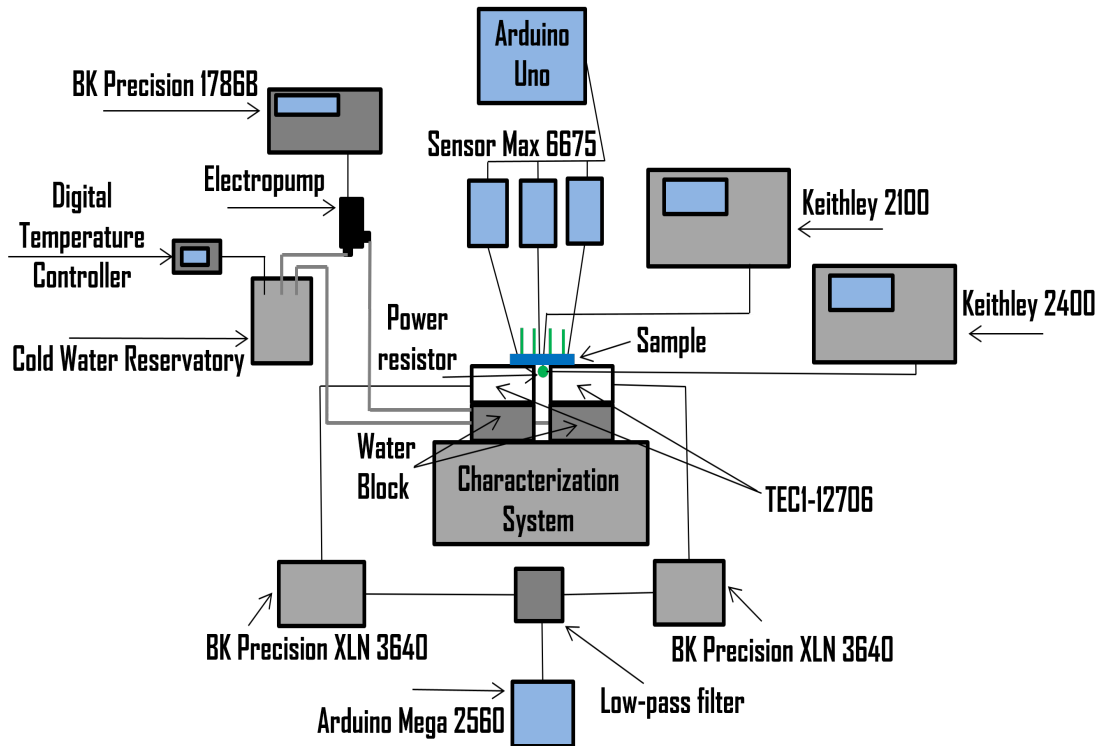
Figure 14 – Graphical Abstract of Publication 4

measurements of electrical resistivity, Seebeck coefficient, and thermal conductivity in a single setup. With this, it is possible to reduce the systematic errors in the Figure of Merit *ZT* and the cost of the equipment. Our equipment, together with the developed software, presented excellent results and analyses, and with that, it proves to be a robust alternative for the characterization of commercial thermoelectric devices, and of laboratory thin film thermoelectric materials.

Keywords

Figure of Merit ● Systematic errors ● Seebeck coefficient ● Thermal conductivity ● Electrical conductivity ● Thermoelectric device characterization

5.1 Introduction

The increasing search and need for new environment friendly energy sources drives research on thermoelectric materials and characterization techniques. Among the materials studied, thermoelectric power plants have emerged as a promising solution. The advantages are: being small, having no moving parts, and performing conversion of heat into electricity with a single module. Numerous researches have been dedicated to looking for high-performance and low-cost thermoelectric materials [1]. The search for such mate-

rials or to improve their ratings is continuously growing due to the strong global demand for economically viable and pollution-free energy conversion [2, 3, 4, 5].

Energy is a commodity with worldwide increasing consumption and being able to harvest energy considering environmental issues have attracted great attention in recent years. To overcome the energy crisis that is approaching the exploitation of sustainable and ecological energy resources is a key issue [6]. Thermoelectric materials and devices, based on the direct conversion of energy between heat and electricity, were considered as promising alternatives to face the challenges of the global energy dilemma [7, 8]. Thermoelectric materials are capable of converting heat into electricity, commonly used in cooling and refrigeration applications [9]. A low-cost and scalable thermoelectric material, with a high energy conversion performance, is highly desired [10].

Thermoelectric devices however, produce tiny voltages and therefore needs to be miniaturized and highly integrated with existing semiconductor chip systems with micro-generators or micro refrigerators [11]. However, part of the difficulty in finding thermoelectric materials is their characterization which would allow performance improvements. The efficiency of thermoelectric materials is assessed by the dimensionless Figure of Merit ZT, which is expressed as $ZT = S^2T/\rho\kappa$. Here, S is the Seebeck coefficient with the unit [VK^{-1}]; ρ is the electrical resistivity with the unit [Ωcm]; T is the temperature with the unit [K]; κ is the thermal conductivity with the unit [Wm^{-1}K^{-1}]. Thus, to obtain the Figure of Merit of a material, it is necessary to measure S, ρ and κ.

In the last two decades, several reviews have been produced on thermoelectric materials, including topics such as designing guidances [7, 12, 13, 14], novel materials [15, 16, 17] and, in particular, on methods of measurement [1, 18, 19, 20, 21]. Developments on measurement techniques should be considered as important as the development of new materials. Sometimes, there are large deviations between experimental results and theoretical predictions [1]. For this reason, the importance of a single equipment that calculates all associated thermoelectric quantities allows reducing systematic errors.

This manuscript presents the development of a complete system for the characterization of thermoelectric generation devices and materials. Such a system performs the measurements of electrical resistivity, Seebeck coefficient, and thermal conductivity in a single piece of equipment that included the development of a software for control and measurement. The combination of these three quantities gives us information about the Figure of Merit, a thermoelectric quantity of great importance for the tuning of materials thermoelectric performance i.e. to improve energy generation. To evaluate the here proposed setup, a thin film of ITO was analyzed. From the measurements and analyses, the equipment proved to be promising for use in industry and scientific research.

5.2 Determination of the Figure of Merit

As already mentioned, to obtain the Figure of Merit, it is necessary to measure the electrical resistivity, the Seebeck coefficient, and the thermal conductivity. Here we will briefly explain how these measurements will be assessed and their importance in the characterization of thermoelectric generators.

5.2.1 Electrical Resistivity

Electrical resistivity is a physical quantity necessary to be determined for the use of materials for electrical and electronic applications, especially if they are films, sheets, and conductive surfaces [22]. The method most extensively used for this purpose is the four-probe system [23, 24] which consists of measuring the current and voltage using independent electrodes from which the resistivity can be obtained according to the sample geometry.

The four-probe system is widely used for the measurement of resistivity and resistances of bulk materials and thin films. This method is not new, having already been used in 1915 to measure the resistance of the Earth [25], known as the Wenner method. However, Valdes [26] adopted the technique to perform electrical resistivity measurements in semiconductor wafers, and, for this reason, it is known today as an analytical method for electrical resistivity measurements in solids, mainly semiconductors. The four-probe method is the most common approach to obtain electrical conductivity [27, 28]. The system consists of a sensor formed by four vertical electrodes, whose tips are coplanarly, collinearly and regularly spaced placed on the sample surface. The two external electrodes are connected to a current source and the inner ones to a voltmeter [29]. However, it is possible to use other geometric arrangements, as well as to inject current through the internal electrodes [22, 29].

During the measurements, one way to improve the probe contact with the sample surface is the use of springs contacts that provides a certain pressure to the sample surface. Thus, it is possible to always assure contact between the four tips and the sample. This method minimizes measurement errors due to the low contact resistance between the electrodes and the sample [30, 31]. The electrical resistivity measurement is also useful in characterizing the electrical properties of conductive surfaces, such as the change in conductivity due to surface oxidation, as described by Petersen [32].

In general, the voltage V at a function of distance l of an electrode that carries a current i in an electrical resistivity material ρ is given by:

$$V = \frac{\rho i}{2\pi f(l)} \tag{5.1}$$

Considering a material of semi-infinite dimensions, with the current going in through one end (called 1) and going out through the opposite side (called 4), the voltage V' could be considered as a first attempt of $f(l)$ as:

$$V' = \frac{\rho i}{2\pi} \left(\frac{1}{l_{12}} - \frac{1}{l_{34}} \right) \tag{5.2}$$

Since l_{12} and l_{34} are the distances of the points 1 to 2 and 3 to 4 respectively. By determining the value of potential at the probes V_n for n as the index of probes 2 and 3 ends, we have to

$$V_2 = \frac{\rho i}{2\pi} \left(\frac{1}{l_{12}} - \frac{1}{l_{23} + l_{34}} \right) \tag{5.3}$$

$$V_3 = \frac{\rho i}{2\pi} \left(\frac{1}{l_{12} + l_{23}} - \frac{1}{l_{34}} \right) \tag{5.4}$$

Thus, the difference in total potential, V = V_2 - V_3 is equivalent to:

$$V = \frac{\rho i}{2\pi} \left(\frac{1}{l_{12}} + \frac{1}{l_{34}} - \frac{1}{l_{23} + l_{34}} - \frac{1}{l_{12} + l_{23}} \right) \tag{5.5}$$

since what interests us is the resistivity ρ, rearranging the Equation 5.5 we have

$$\rho = \frac{2\pi \frac{V}{i}}{\frac{1}{l_{12}} + \frac{1}{l_{34}} - \frac{1}{l_{23} + l_{34}} - \frac{1}{l_{12} + l_{23}}} \tag{5.6}$$

in our case the spacing between the probe tips is equal, so $l_{12} = l_{23} = l_{34} = l$ and so the Equation 5.6 is reduced to

$$\rho = 2\pi l \frac{V}{i} \tag{5.7}$$

this is the general equation. However, there are situations where we do not have a material of semi-infinite dimensions and, therefore, the previous Equation 5.7 must be corrected for a finite geometry.

For an arbitrarily shaped sample, the electrical resistivity is given by the Equation 5.8, F being the correction factor that depends on the shape of the sample, its dimensions, where the tips for the measurement are placed and also, how it is arranged (type of substrate, for example, in the case of deposited material).

$$\rho = 2\pi l \frac{V}{i} F \tag{5.8}$$

F can be derived also for other geometries as carried by Valdes, Schroder, Smits and Uhlir [26, 27, 30, 33].

For our case, the ITO sample is rectangular thin film, with finite length a, width d, and thickness w, presented in the Figure 15. Being w $< 4l/10$, the F correction factor to be used is shown in Equation 5.9.

$$F = \frac{\pi}{\pi\frac{l}{d} + \ln\left(\frac{1-e^{-\frac{4\pi l}{d}}}{1-e^{-\frac{2\pi l}{d}}}\right) + e^{-\frac{2\pi l}{d}\left(\frac{a}{l}-2\right)}\frac{\left(1-e^{-\frac{6\pi l}{d}}\right)\left(1-e^{-\frac{2\pi l}{d}}\right)}{1+e^{-\frac{2\pi a}{d}}}} \tag{5.9}$$

The Figure 15 shows the four-probe in line, three thermocouples and the dimensions on the rectangular ITO sample. Sample dimensions are w the thickness, a the length and d the width of the sample. l indicates the distance between consecutive probes. Thermocouples were positioned parallel to the first and last probes and another at the sample center.
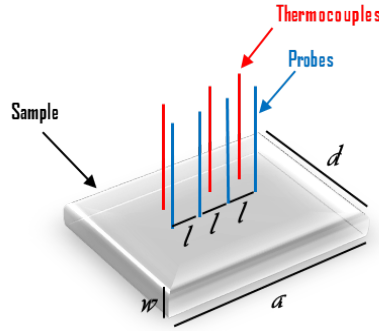

Figure 15 – Illustration of four-probe, three thermocouples placed parallel to the contacts on the extremes and at the center and the dimensions on the rectangular ITO sample. All sample dimensions and contact distances are represented in terms of the equation parameters.

5.2.2 Seebeck coefficient

In 1821, the German physicist Thomas Johann Seebeck observed that a compass needle was deflected from its position when it was placed in the vicinity of a closed circuit, where the circuit was simply formed by a link of two different metals and whose junctions were maintained at different temperatures [34]. The temperature difference causes, in the material, diffusion of charge carriers (electrons or holes) from the hot junction to the cold junction. A configuration of mobile charge carriers migrate to the cold side and leave behind the immobile cores of opposite charge on the hot side, thus giving rise to a voltage difference called thermoelectric potential. The value of the thermoelectric electromotive

force *fem*, which is generated between the two different materials, such as metals or semiconductors, can be obtained through Equation 5.10.

$$E_{AB} = S\Delta T, \tag{5.10}$$

where S is defined as the relative Seebeck coefficient between materials A and B. The Equation 5.10 can be rewritten according to the potential difference generated, knowing that $\mathrm{E}_{AB} = -\Delta \mathrm{V}$

$$S = -\frac{\Delta V}{\Delta T} \tag{5.11}$$

This leads to a direct current that flows through the materials, through the junction, when they are kept at different temperatures. The electromotive force E_{AB} and the coefficient S are positive if the conventional current flows from the material A to B from the hot junction.

Two approaches are commonly used to measure the Seebeck coefficient in the thin-film plane: the integral method and the differential method. In the integral method, [35] one end of the sample is kept at a reference temperature (usually room temperature or 273 K) and the other is increased continuously over a temperature range of interest. This method assumes that the thermal balance between the thermocouple junctions and the sample is achieved instantly, and there is no delay between the voltage and temperature measurements.

The differential method, used in this work, for measuring the Seebeck coefficient in the plane is more widely used for thin-film thermoelectric materials [36, 37, 38]. Small thermal gradients are applied along the length of the sample, close to the temperature of interest; that is, in the linear regime. Several data points with variable temperature differences are collected and the slope of the voltage about the temperature difference provides the Seebeck coefficient.

5.2.3 Thermal Conductivity

The measurement of thermal conductivity is performed using the method created by Kohlrausch [39]. It is a well established method in the physical and thermodynamic analysis of materials, presented in [40, 41].

The Kohlrausch method shows how constant temperature can be used to find the ratio of thermal (κ) and electrical (σ), known as the Wiedemann-Franz ratio [42]. The extreme regions of the sample are kept as close as possible to the same temperature by making $\mathrm{T}_1 = \mathrm{T}_2 = \mathrm{T}$, while the center of the sample is heated to T_h, thus generating a

temperature gradient $\Delta T = T_h - T$. This generates a potential difference ΔV between the ends of the sample and Equation 5.12 describes the entire phenomenon.

$$\frac{\kappa}{\sigma} = \frac{(\Delta V)^2}{8\Delta T}$$ (5.12)

with this, it is possible to determine simply the κ/σ ratio of the thermal and electrical conductivities, involving only the reading of the temperature difference and the potentials in two points of the sample.

5.2.4   Figure of Merit

With the measurements of electrical conductivity, Seebeck coefficient, and thermal conductivity it is possible to obtain the Figure of Merit ZT through Equation 5.13.

$$ZT = \frac{S^2 T}{\rho \kappa}$$ (5.13)

where S is the Seebeck coefficient, ρ the electrical resistivity, κ the thermal conductivity and T the temperature, which leaves the ZT dimensionless.

5.3   Experimental setup

The developed system has a structure assembled to carry out electrical conductivity measurements, Seebeck coefficient, and thermal conductivity in the same equipment. This excludes errors due to the use of various equipment and increases the robustness of the measurements.

In the system we developed, heatsinks, fans, water blocks, Peltier devices, a Teflon block, a power resistor, and a metallic structure that provides stability and support for the entire system were used. All characterization system is done as illustrated in detail in the Figure 16, alternating only with the rectangular Teflon block, to perform the electrical conductivity measurements and the Seebeck coefficient, and the power resistor, to perform the thermal conductivity measurement.

To carry out the Seebeck coefficient and thermal conductivity measurements, temperature differences must occur. The water blocks, where cold water is circulated, have the function of maintaining a stable temperature in the Peltier modules, generating a temperature gradient and preventing it from entering thermal equilibrium. Thermal contact between the Peltier modules and the sample is mechanically assured by a couple of coils besides the extra contact pin coils.

The heatsinks under the Peltier modules function to dissipate excess heat from the aluminum water blocks. The two fans under the smaller heatsinks under aluminum

waterblocks are used to force an airflow from top to bottom, assisting the heatsink that is at the botton of the structure. In this way, the heat generated by the Peltier modules is efficiently dissipated out of the system.

As illustrated in Figure 16, the structure has two circular air vents on its sides, the front and rear part is open, to allow air to circulate efficiently.
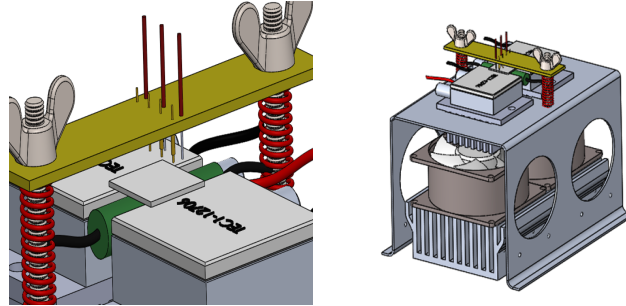

Figure 16 – Illustration of the thermoelectric sample characterization system. In the image it is possible to check the circular air vents on the side, increasing the efficiency in cooling the system.

5.3.1   Electrical conductivity and Seebeck coefficient

To perform the electrical conductivity measurement, the four-probe technique was used, where 4 spring contact pins model 0985-2-15-20-71-14-11-0 brand Mil-max 0.48 mm and limited to 2 A current, in diameter and in line are placed in contact on the sample surface (Figure 15). The pins were equally spaced by 3.9 mm so that minimal sample length a $\geq$ 14 mm and the width d $\geq$ 4 mm in order to acommodate pins and thermocouples. The sample is on a surface, formed by the two Peltier devices and the Teflon block. The Teflon block is necessary to give mechanical support to the sample between the Peltier modules and also to avoid them to enter into thermal equilibrium. An external voltage is applied through the two external pins, using the 5 1/2 digit Keithley 2400 source-measure unit , from which the current is also measured. Minimal applied current is about 1 μA and maximal is 1 A but limited to 20 V. We measure the voltage using the two internal pins, using the 6 1/2 digit Keithley 2100 multimeter with its resolution limited to 0.1 μV at 0.1 V range and 1 mV at 1000 V range, as illustrated in Figure 17. With the IV curves of the material, we obtain, according to the Equation 5.8, the electrical resistivity of the sample.

The measurement of the Seebeck coefficient is carried using two Peltier modules, placed under the sample. One module is the hot temperature reference (limited to 390 K) and the other is the cold temperature reference (limited to 280 K). The purpose here is to generate a temperature gradient in the sample. Voltage is applied to Peltier devices through the Control Software, which was developed in Python. The software controls

an Arduino Mega 2560, which sends a voltage to a low-pass filter. This low-pass filter converts the received signal to two independent Bk Precision XLN3640 sources, each of which will apply a voltage to a Peltier device. The water blocks are connected by hoses to a cooling system, formed by Cold Water Reservoir, the Digital Temperature Controller, the Electropump, and the BK Precision 1786B that provides the necessary voltage.

The procedure is then to generate a temperature gradient in the material so that by the Seebeck effect the generation of voltage occurs. The voltage generated is measured by Keithley 2100, through the two external pins connected to the sample. The Arduino Uno, through the Max6675 Sensors, performs the reading of the temperatures in the sample, to analyze the data according to Equation 5.11. Figure 17 shows the assembly diagram for measurements of the Seebeck coefficient.

5.3.2 Thermal conductivity

The measurement of thermal conductivity is carried out by the Kohlrausch method which uses 2 Peltier modules being at the same cold reference temperature, and a power resistor in place of the Teflon block in the center of the sample to be the hot temperature reference.

The power resistor is activated, by Keithley 2400, to raise the temperature of the sample center, while the Peltiers cool the external parts, from the Arduino Mega2560, the low-pass filter, and the two BK Precision XLN3640. Peltier devices are also cooled by the cooling system, composed of Cold Water Reservoir, the Digital Temperature Controller, the Electropump, and the BK Precision 1786B.

The voltage generated between the outer pins on the surface of the material is measured with the Keithley 2100 multimeter. The temperatures on the material surface points are a very important to be taken close to the measuring pins using three K type thermocouples and an Arduino Uno connecting each thermocouple to a Max6675 transducer with 0.25 K temperature resolution. Typical tip ball diameter is of the order of 0.5 mm, the same as the spring electrical pins. One thermocouple is placed close to the center pin and the other two close to the outer ones. With the data collected, simply apply Equation 17 and obtain the thermal conductivity of the material.

For an analysis of the operation of the equipment, a sample of Indium tin oxide, commonly referred to as ITO, was used which is a standard degenerate n-type transparent semiconductor material. It is highly transparent to visible light ($>80\%$) and low resistivity ($\rho < 5 \times 10^{-4}\Omega$cm) [43, 44], being $\rho \approx 1 \times 10^{-4}\Omega$cm in [45], and ranged from $2.9 \times 10^{-4}\Omega$cm to $3.2 \times 10^{-3}\Omega$cm in [46].

Its Seebeck coefficient varies from 5.96 μVK^{-1} to 43.16 μVK^{-1}, depending on the material manufacturing process [47]. Thermal conductivity ranged to 4.00 to 5.86
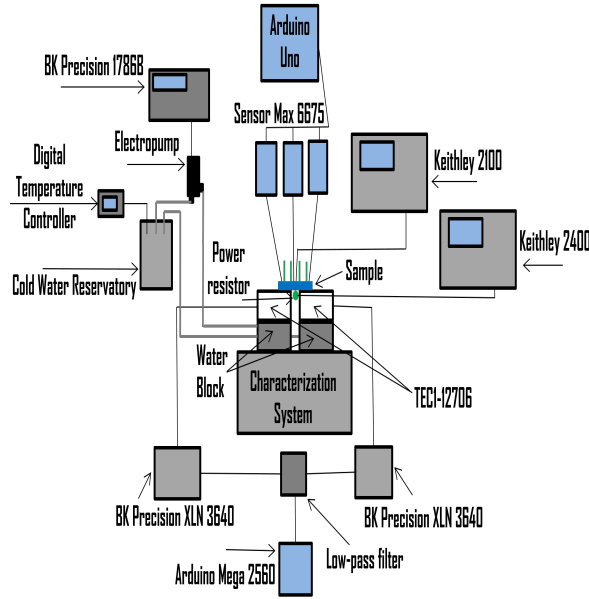
Figure 17 – Scheme for measuring electrical resistivity, Seebeck coefficient and thermal conductivity.

$Wm^{-1}K^{-1}$ according to material growth [46]. In [48] we have $\kappa \approx 0.84\pm 0.12$ $Wm^{-1}K^{-1}$ at room temperature for nanogranular ITO, can be $\kappa \approx 10$ $Wm^{-1}K^{-1}$ at room temperature [49, 50], $\kappa \approx 1.2$ $Wm^{-1}K^{-1}$ at 973 K in sintered In_2O_3 doped by Zn and Ce [50]. In [51, 52] $\kappa \approx 1.58\text{-}1.75$ $Wm^{-1}K^{-1}$.

The Z-factor varies according to the thickness of the material, being for 50 nm, 100 nm, 200 nm, 280 nm respectively, $9.76\times 10^{-5}K^{-1}$, $7.16\times 10^{-4}K^{-1}$, $1.28\times 10^{-3}K^{-1}$ and $1.84\times 10^{-3}K^{-1}$ [54]. In [53] the Z-factor is $1.19\times 10^{-2}K^{-1}$.

Our sample is a rectangular thin ITO film deposited onto a glass substrate w = 10 nm thick. The spacing between the 4 points of the measurement is l = 3.9 mm, the length of the rectangular sample (in the direction of the 4 points) is a = 24.9 mm and the width of the rectangular sample (perpendicular to the 4 points) is d = 17.1 mm.

5.4 Results

To evaluate the efficiency of the equipment, a sequence of tests was performed on a thin ITO film, which is already well established in the literature. We performed the measurements of electrical conductivity, Seebeck coefficient, and thermal conductivity, to obtain the Figure of Merit.

Five IV curves were made for the sample. Figure 18 shows one of the IV curves obtained for calculating the electrical resistivity ρ of ITO.

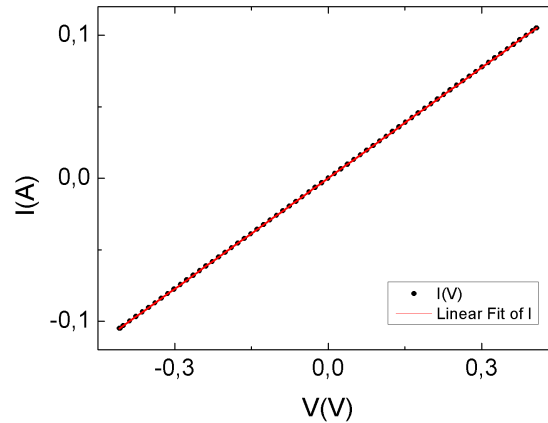From the graph, we obtained the resistance R = V/I of the sample, and from

Figure 18 – IV curve obtained for calculating the electrical resistivity ρ, of ITO.

Equation 5.8 we calculated the resistivity of the sample.

With a statistical calculation, we obtain the electrical resistivity of the material, presented in Table 19. Five measurements were also taken to calculate the Seebeck S coefficient. Figure 19 shows one of the five V(ΔT) curves obtained.
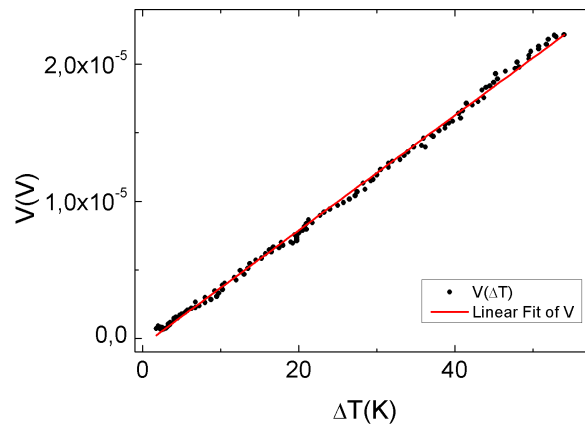

Figure 19 – V(ΔT) curve obtained to calculate the Seebeck coefficient. T$_C$= 293 K

From statistical calculations, the value of the Seebeck S coefficient of the ITO sample was obtained, presented in Table 19. The values of thermal conductivity were calculated from five measurements and the Equation 5.12 and are shown in Table 19. Thus, Table 19 presents all the experimental data obtained from our analysis and those presented in the literature. The value of Z was calculated by the Equation 5.13 using the values of reference [46, 47, 48, 50] and presented in the same Table. As can be seen in the comparison of the values obtained in the literature and the results obtained by our equipment, the equipment presented an excellent performance and obtained outstanding

results, showing its robustness for applications in the characterization of thermoelectric devices.

Parameter	Literature	Experimental
ρ (Ωcm)	1×10^{-4} [45] $\to$ 3.2×10^{-3} [46]	$(1.3100 \pm 0.0007) \times 10^{-4}$
S (μVK^{-1})	$5.96 \to 43.16$ [47]	(4.38 ± 0.22)
κ (Wm^{-1}K^{-1})	0.84 [48] $\to 10$ [50]	(3.10 ± 0.83)
Z (K^{-1})	$2.98 \times 10^{-5} \to 5.82 \times 10^{-4}$	$(4.7 \pm 1.4) \times 10^{-5}$

Table 19 – Values mean of the electrical resistivity, Seebeck coefficient, and thermal conductivity of the ITO sample.

5.5 Conclusions

The single equipment shown here reduces the time and complexity considered in the measurement of all the three thermoelectric quantities necessary to obtain the Figure of Merit since, for that task, it is commonly used at least two distinct equipment one for the Seebeck coefficient and electrical resistivity and another for the thermal conductivity. The presented equipment was designed to performed accurate temperature control leading to stable measurements. The values of electrical resistivity, Seebeck coefficient, thermal conductivity obtained by our robust thermoelectric characterization system will contribute to improve the access to the determination of the Figure of Merit in a simple, fast and reliable form, which will contribute for research on the characterization of thermoelectric materials.

Acknowledgement

References

1 MA, Z. et al. Review of experimental approaches for improving zT of thermoelectric materials. *Materials Science in Semiconductor Processing*, Elsevier BV, v. 121, p. 105303, jan. 2021. Disponível em: <https://doi.org/10.1016/j.mssp.2020.105303>. 95, 96

2 HARMAN, T. C. Quantum dot superlattice thermoelectric materials and devices. *Science*, American Association for the Advancement of Science (AAAS), v. 297, n. 5590, p. 2229–2232, set. 2002. Disponível em: <https://doi.org/10.1126/science.1072886>. 96

3 JOSHI, G. et al. Enhanced thermoelectric figure-of-merit in nanostructured p-type silicon germanium bulk alloys. *Nano Letters*, American Chemical Society (ACS), v. 8, n. 12, p. 4670–4674, out. 2008. Disponível em: <https://doi.org/10.1021/nl8026795>. 96

4 SRINIVASAN, R.; GOTHARD, N.; SPOWART, J. Improvement in thermoelectric properties of an n-type bismuth telluride (bi2se0.3te2.7) due to texture development and grain refinement during hot deformation. *Materials Letters*, Elsevier BV, v. 64, n. 16, p. 1772–1775, ago. 2010. Disponível em: <https://doi.org/10.1016/j.matlet.2010.05.018>. 96

5 RODRÍGUEZ, J.; MORENO, L. ceramics as new thermoelectric material for low temperature applications. *Materials Letters*, Elsevier BV, v. 65, n. 1, p. 46–48, jan. 2011. Disponível em: <https://doi.org/10.1016/j.matlet.2010.09.034>. 96

6 SHI, X.-L.; ZOU, J.; CHEN, Z.-G. Advanced thermoelectric design: From materials and structures to devices. *Chemical Reviews*, American Chemical Society (ACS), v. 120, n. 15, p. 7399–7515, jul. 2020. Disponível em: <https://doi.org/10.1021/acs.chemrev.0c00026>. 96

7 TAN, G.; ZHAO, L.-D.; KANATZIDIS, M. G. Rationally designing high-performance bulk thermoelectric materials. *Chemical Reviews*, American Chemical Society (ACS), v. 116, n. 19, p. 12123–12149, ago. 2016. Disponível em: <https://doi.org/10.1021/acs.chemrev.6b00255>. 96

8 SHI, X.; CHEN, L. Thermoelectric materials step up. *Nature Materials*, Springer Science and Business Media LLC, v. 15, n. 7, p. 691–692, jun. 2016. Disponível em: <https://doi.org/10.1038/nmat4643>. 96

9 DISALVO, F. J. Thermoelectric cooling and power generation. *Science*, American Association for the Advancement of Science (AAAS), v. 285, n. 5428, p. 703–706, jul. 1999. Disponível em: <https://doi.org/10.1126/science.285.5428.703>. 96

10   ZHANG, Y.; STUCKY, G. D. Heterostructured approaches to efficient thermoelectric materials. *Chemistry of Materials*, American Chemical Society (ACS), v. 26, n. 1, p. 837–848, set. 2013. Disponível em: <https://doi.org/10.1021/cm402150j>. 96

11   WEI, J. et al. Review of current high-ZT thermoelectric materials. *Journal of Materials Science*, Springer Science and Business Media LLC, v. 55, n. 27, p. 12642–12704, jun. 2020. Disponível em: <https://doi.org/10.1007/s10853-020-04949-0>. 96

12   SNYDER, G. J.; TOBERER, E. S. Complex thermoelectric materials. *Nature Materials*, Springer Science and Business Media LLC, v. 7, n. 2, p. 105–114, fev. 2008. Disponível em: <https://doi.org/10.1038/nmat2090>. 96

13   YANG, J. et al. On the tuning of electrical and thermal transport in thermoelectrics: an integrated theory–experiment perspective. *npj Computational Materials*, Springer Science and Business Media LLC, v. 2, n. 1, fev. 2016. Disponível em: <https://doi.org/10.1038/npjcompumats.2015.15>. 96

14   BELL, L. E. Cooling, heating, generating power, and recovering waste heat with thermoelectric systems. *Science*, American Association for the Advancement of Science (AAAS), v. 321, n. 5895, p. 1457–1461, set. 2008. Disponível em: <https://doi.org/10.1126/science.1158899>. 96

15   ZHU, T. et al. High efficiency half-heusler thermoelectric materials for energy harvesting. *Advanced Energy Materials*, Wiley, v. 5, n. 19, p. 1500588, jul. 2015. Disponível em: <https://doi.org/10.1002/aenm.201500588>. 96

16   HE, J.; TRITT, T. M. Advances in thermoelectric materials research: Looking back and moving forward. *Science*, American Association for the Advancement of Science (AAAS), v. 357, n. 6358, p. eaak9997, set. 2017. Disponível em: <https://doi.org/10.1126/science.aak9997>. 96

17   ALAM, H.; RAMAKRISHNA, S. A review on the enhancement of figure of merit from bulk to nano-thermoelectric materials. *Nano Energy*, Elsevier BV, v. 2, n. 2, p. 190–212, mar. 2013. Disponível em: <https://doi.org/10.1016/j.nanoen.2012.10.005>. 96

18   CAHILL, D. G. et al. Thermal conductivity of thin films: Measurements and understanding. *Journal of Vacuum Science & Technology A: Vacuum, Surfaces, and Films*, American Vacuum Society, v. 7, n. 3, p. 1259–1266, maio 1989. Disponível em: <https://doi.org/10.1116/1.576265>. 96

19   LIU, Y. et al. Measuring methods for thermoelectric properties of one-dimensional nanostructural materials. *RSC Advances*, Royal Society of Chemistry (RSC), v. 6, n. 54, p. 48933–48961, 2016. Disponível em: <https://doi.org/10.1039/c5ra23634g>. 96

20 ZEVALKINK, A. et al. A practical field guide to thermoelectrics: Fundamentals, synthesis, and characterization. *Applied Physics Reviews*, AIP Publishing, v. 5, n. 2, p. 021303, jun. 2018. Disponível em: <https://doi.org/10.1063/1.5021094>. 96

21 WU, H. et al. Advanced electron microscopy for thermoelectric materials. *Nano Energy*, Elsevier BV, v. 13, p. 626–650, abr. 2015. Disponível em: <https://doi.org/10.1016/j.nanoen.2015.03.034>. 96

22 ZRUDSKY, D. R.; BUSH, H. D.; FASSETT, J. R. Four point sheet resistivity techniques. *Review of Scientific Instruments*, AIP Publishing, v. 37, n. 7, p. 885–890, jul. 1966. Disponível em: <https://doi.org/10.1063/1.1720355>. 97

23 KENNEDY, J. K. Four-point probe for measuring the resistivity of small samples. *Review of Scientific Instruments*, AIP Publishing, v. 33, n. 7, p. 773–775, jul. 1962. Disponível em: <https://doi.org/10.1063/1.1717968>. 97

24 PETERSEN, C. et al. Scanning microscopic four-point conductivity probes. *Sensors and Actuators A: Physical*, Elsevier BV, v. 96, n. 1, p. 53–58, jan. 2002. Disponível em: <https://doi.org/10.1016/s0924-4247(01)00765-8>. 97

25 WENNER, F. A method of measuring earth resistivity. *Bulletin of the Bureau of Standards*, National Institute of Standards and Technology (NIST), v. 12, n. 4, p. 469, maio 1916. Disponível em: <https://doi.org/10.6028/bulletin.282>. 97

26 VALDES, L. Resistivity measurements on germanium for transistors. *Proceedings of the IRE*, Institute of Electrical and Electronics Engineers (IEEE), v. 42, n. 2, p. 420–427, fev. 1954. Disponível em: <https://doi.org/10.1109/jrproc.1954.274680>. 97, 98

27 SCHRODER, D. K. *Semiconductor Material and Device Characterization.* Wiley-IEEE Press, 2015. ISBN 0471739065. Disponível em: <https://www.xarg.org/ref/a/0471739065/>. 97, 98

28 F84-93, A. M. *Standard Test Method for Measuring Resistivity of Silicon Wafers With an In-Line Four-Point Probe.* [S.l.]: West Conshohocken, PA, 1999. 97

29 SEIDEL, C. *Acta Polymerica*, Wiley, v. 38, n. 1, p. 101–101, jan. 1987. Disponível em: <https://doi.org/10.1002/actp.1987.010380126>. 97

30 SMITS, F. M. Measurement of sheet resistivities with the four-point probe. *Bell System Technical Journal*, Institute of Electrical and Electronics Engineers (IEEE), v. 37, n. 3, p. 711–718, maio 1958. Disponível em: <https://doi.org/10.1002/j.1538-7305.1958.tb03883.x>. 97, 98

31 KEYWELL, F.; DOROSHESKI, G. Measurement of the sheet resistivity of a square wafer with a square four-point probe. *Review of Scientific Instruments*, AIP Publishing,

v. 31, n. 8, p. 833–837, ago. 1960. Disponível em: <https://doi.org/10.1063/1.1717065>. 97

32 PETERSEN, C.; GREY, F.; AONO, M. Oxidation of clean silicon surfaces studied by four-point probe surface conductance measurements. *Surface Science*, Elsevier BV, v. 377-379, p. 676–680, abr. 1997. Disponível em: <https://doi.org/10.1016/s0039-6028(96) 01470-7>. 97

33 UHLIR, A. The potentials of infinite systems of sources and numerical solutions of problems in semiconductor engineering. *Bell System Technical Journal*, Institute of Electrical and Electronics Engineers (IEEE), v. 34, n. 1, p. 105–128, jan. 1955. Disponível em: <https://doi.org/10.1002/j.1538-7305.1955.tb03765.x>. 98

34 SEEBECK, T. J. Ueber die magnetische polarisation der metalle und erze durch temperaturdifferenz. *Annalen der Physik*, Wiley, v. 82, n. 3, p. 253–286, 1826. Disponível em: <https://doi.org/10.1002/andp.18260820302>. 99

35 KUMAR, S. R. S.; KASIVISWANATHAN, S. A hot probe setup for the measurement of seebeck coefficient of thin wires and thin films using integral method. *Review of Scientific Instruments*, AIP Publishing, v. 79, n. 2, p. 024302, 2008. Disponível em: <https://doi.org/10.1063/1.2869039>. 100

36 BOFFOUÉ, O. et al. Experimental setup for the measurement of the electrical resistivity and thermopower of thin films and bulk materials. *Review of Scientific Instruments*, AIP Publishing, v. 76, n. 5, p. 053907, maio 2005. Disponível em: <https://doi.org/10.1063/1.1912820>. 100

37 SINGH, R.; SHAKOURI, A. Thermostat for high temperature and transient characterization of thin film thermoelectric materials. *Review of Scientific Instruments*, AIP Publishing, v. 80, n. 2, p. 025101, fev. 2009. Disponível em: <https://doi.org/10.1063/1. 3072603>. 100

38 RAVICHANDRAN, J. et al. An apparatus for simultaneous measurement of electrical conductivity and thermopower of thin films in the temperature range of 300–750 k. *Review of Scientific Instruments*, AIP Publishing, v. 82, n. 1, p. 015108, jan. 2011. Disponível em: <https://doi.org/10.1063/1.3529438>. 100

39 KOHLRAUSCH, F. Ueber den stationären temperaturzustand eines elektrisch geheizten leiters. *Annalen der Physik*, Wiley, v. 306, n. 1, p. 132–158, 1900. Disponível em: <https://doi.org/10.1002/andp.19003060107>. 100

40 POIRIER, D. R.; GEIGER, G. H. Conduction of heat in solids. In: *Transport Phenomena in Materials Processing*. Springer International Publishing, 2016. p. 281–327. Disponível em: <https://doi.org/10.1007/978-3-319-48090-9_9>. 100

41   ESTERMANN, I. *Methods in Experimental Physics. Classical Methods.* [S.l.]: Academic Press, New York, 1959. ISBN 978-0-12-475901-5. 100

42   KITTEL, C. *Introduction to Solid State Physics.* 8. ed. Wiley, 2004. ISBN 9780471415268. Disponível em: <http://www.amazon.com/Introduction-Solid-Physics-Charles-Kittel/dp/047141526X/ref=dp_ob_title_bk>. 100

43   KNICKERBOCKER, S. A.; KULKARNI, A. K. Calculation of the figure of merit for indium tin oxide films based on basic theory. *Journal of Vacuum Science & Technology A: Vacuum, Surfaces, and Films*, American Vacuum Society, v. 13, n. 3, p. 1048–1052, maio 1995. Disponível em: <https://doi.org/10.1116/1.579583>. 103

44   HAN, H. et al. Characterization of the physical and electrical properties of indium tin oxide on polyethylene napthalate. *Journal of Applied Physics*, AIP Publishing, v. 98, n. 8, p. 083705, out. 2005. Disponível em: <https://doi.org/10.1063/1.2106013>. 103

45   C.G. Granqvist and A. Hultåker. Transparent and conducting ITO films: new developments and applications. *Thin Solid Films*, 411(1):1–5, May 2002. 103, 106

46   ASHIDA, T. et al. Thermal transport properties of polycrystalline tin-doped indium oxide films. *Journal of Applied Physics*, AIP Publishing, v. 105, n. 7, p. 073709, abr. 2009. Disponível em: <https://doi.org/10.1063/1.3093684>. 103, 104, 105, 106

47   LIU, H. et al. Improving seebeck coefficient of ITO/AZO transparent film thermocouple by ITO (100) preferred orientation. *Sensors and Actuators A: Physical*, Elsevier BV, v. 311, p. 112089, ago. 2020. Disponível em: <https://doi.org/10.1016/j.sna.2020.112089>. 103, 105, 106

48   BRINZARI, V. I. et al. Ultra-low thermal conductivity of nanogranular indium tin oxide films deposited by spray pyrolysis. *Applied Physics Letters*, AIP Publishing, v. 110, n. 7, p. 071904, fev. 2017. Disponível em: <https://doi.org/10.1063/1.4976629>. 104, 105, 106

49   BÉRARDAN, D. et al. :ge, a promising n-type thermoelectric oxide composite. *Solid State Communications*, Elsevier BV, v. 146, n. 1-2, p. 97–101, abr. 2008. Disponível em: <https://doi.org/10.1016/j.ssc.2007.12.033>. 104

50   LAN, J.-L. et al. Enhanced thermoelectric performance of in2o3-based ceramics via nanostructuring and point defect engineering. *Scientific Reports*, Springer Science and Business Media LLC, v. 5, n. 1, jan. 2015. Disponível em: <https://doi.org/10.1038/srep07783>. 104, 105, 106

51 OHTAKI, M. et al. High-temperature thermoelectric properties of in2o3-based mixed oxides and their applicability to thermoelectric power generation. *Journal of Materials Chemistry*, Royal Society of Chemistry (RSC), v. 4, n. 5, p. 653, 1994. Disponível em: <https://doi.org/10.1039/jm9940400653>. 104

52 OHTAKI, M. Recent aspects of oxide thermoelectric materials for power generation from mid-to-high temperature heat source. *Journal of the Ceramic Society of Japan*, Ceramic Society of Japan, v. 119, n. 1395, p. 770–775, 2011. Disponível em: <https://doi.org/10.2109/jcersj2.119.770>. 104

53 CHEN, Z. et al. Fabrication of highly transparent and conductive indium–tin oxide thin films with a high figure of merit via solution processing. *Langmuir*, American Chemical Society (ACS), v. 29, n. 45, p. 13836–13842, out. 2013. Disponível em: <https://doi.org/10.1021/la4033282>. 104

54 MAZUR, M. et al. Influence of thickness on transparency and sheet resistance of ITO thin films. In: *The Eighth International Conference on Advanced Semiconductor Devices and Microsystems*. IEEE, 2010. Disponível em: <https://doi.org/10.1109/asdam.2010.5666348>. 104

6 Preparation and Electrical Characterization of MoS$_2$ pellets

To finalize our study we applied the knowledge already obtained in the study of a material, and this study is still in progress. Below we have the growth of MoS$_2$ pellets and their following electrical characterization by means of our equipment. Other measures and studies are already being carried out and, later, this article will also be submitted to a journal.

Abstract

Molybdenum Disulfide (MoS$_2$) is a very interesting material with numerous applications. This article discusses the preparation and characterization of MoS$_2$ pellets. In the preparation, we subjected the pellets to different temperatures and pressures and analyzed the IV curve with the 4-probe technique obtaining the electrical conductivity. Our best results were obtained for annealing temperature of 700 °C and press load of 20 T.

Keywords

6.1 Introduction

Development of materials with desired properties and characteristics has been a fundamental challenge for decades. One of the most promising materials is Molybdenum Disulfide (MoS$_2$). It is established as multi-utility and multi-functional material due to its capability to display varying properties as it transforms from bulk to nanoscale.

The band gap is one example. When the material is in its bulk form, it has an indirect band gap with 1.23 eV [1]. But, when varying the thickness from bulk to a few monolayers the band gap change its value to 1.8 eV as well as being subject to an indirect-to-direct band-gap transition [2, 3, 4]. The electronic and optical properties can be taylored by band gap tunning due to the quantum confinement effect [21], so this MoS$_2$ characteristics is better suitable for electronic and photonic devices than graphene (zero band-gap).

Bulk MoS_2 crystal structure has a configuration of stacking Mo between six S atoms [20]. It belongs to class of TMD which have three atoms thick layers. In them, neighboring layers are connected by weak Van der Waals forces [19] which enable layers to slide one over other, facilitating shear along the basal plane of crystals. This phenomenon at atomic dimensions which was achieved by ion beam has been studied by [23]. Depending on the stacking sequence and atomic coordination between Mo and S atoms, the crystal structure display rich polytypism [25] with three different polytypes format, namely 1T [24, 26], 2H [27, 28] and 3R [29].

The bulk form is studied in the powder form. The powder needs to be subjected to pressure and heat treatment and from this we can get information regarding its structural and optical properties [14], electrical properties [15], mechanism of lubrication [16], tribological performance [17], wear and frictional behaviour [18] and the thermoelectric characterization [30].

This material was considered as a promising thermoelectric material due to general characteristics such as economic value and non-toxicity and physical properties such as high Seebeck coefficient and low thermal conductivity. However, the low electrical conductivity is a major challenge for achieving suitable performance for such kind of application [30].

In this work we propose a simple method of preparation and electrical characterization of MoS_2 pellets for the desired thermoelectric applications.

6.2   Materials and Methods

To prepare bulk MoS_2 pellets, 99% pure MoS_2 powder was used (Make: Sigma Aldrich, USA). Nine 10 mm diameter pellets were prepared at different pressures and temperatures. All pellets weigh approximately 0.5 g.

We use Pellet Press Die Set for an initial compaction of the powder, pressing for 30 seconds, and the result is shown in Figure 20.

The pellets are vacuum sealed and the next step is to put pressure on them. The pressure, made by weight in a isostatic pressing, was made with the values of 10 T, 15 T and 20 T.

The heat treatment is carried out at three different temperatures: 600 °C, 700 °C e 800 °C. They are heated to temperature and then held for 2 h. The furnace has a continuous flow of Nitrogen and a sulfur-rich atmosphere. The resulting nine pellets are shown in the Figure 21.

The electrical characterization was performed by measuring the IV curves of the pellets. Three IV curves were made for each pellet. The technique used was the 4-probe

Figure 20 – Pellet after being compacted in the Pellet Press Die Set.

Figure 21 – Nine pellets from MoS$_2$ with temperatures ranging from 600 °C to 800 °C and pressures considering a load of 10 T to 20 T.

technique, with equipment presented in [22] and shown in the Figure 22.

6.3 Results and discussions

Figure 23 shows the IV curve for one of the pellets. Three IV curves were made for each of the nine pellets. The noticiable linearity is indicative of ohmic behavior. Through the analysis of these curves we were able to obtain the electrical conductivity of each one.

The equation has a linear form, where the axis y is the current I and the axis x is the voltage V. So, the equation has a form

$$I = \alpha V + \beta \qquad (6.1)$$

where α and β are constants, respectively the angular coefficient and the linear
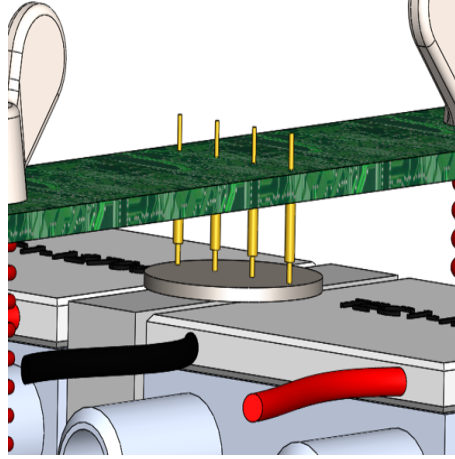
Figure 22 – 4-probe technique used for electrical conductivity measurement of MoS$_2$ pellets.

coefficient. As we know, the Ohm's Law is

$$I = \frac{V}{R} \tag{6.2}$$

where R is the resistance of the material and your inverse, called σ, is the electrical conductivity and is the parameter α. So, the Equation 6.1 has a form

$$I = \sigma V \tag{6.3}$$

Through the linear regression, a machine learning model, we fit the curve and extract the parameters of the curve, obtained the σ for each sample. Table 20 shows the electrical conductivity σ values for each of the pellets. The results show us an interesting behavior. The effect of pressure is more pronounced for the 600 °C annealing temperature for which it almost doubles from lower to higher loads. For the temperatures of 700 °C and 800 °C the effect is almost negligible.

Table 20 – Electrical conductivity measurements (σ) for MoS$_2$ pellets with different pressures and temperatures.

σ $(\Omega^{-1}m^{-1}).10^{-5}$	10 T	15 T	20 T
600 °C	1.20	1.78	2.15
700 °C	3.66	3.48	3.68
800 °C	2.87	2.89	3.04

On the other hand, the temperature of the heat treatment is very important. We noticed a clear increase of σ from 600 °C to 700 °C, and then a drop when evaluated with 800 °C.
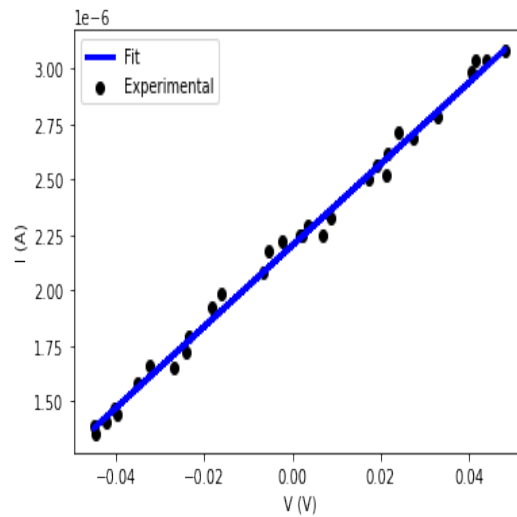
Figure 23 – IV Curve for MoS$_2$ pellet.

This shows us that 700 °C would be the ideal temperature for this heat treatment, and that a higher pressure, 20 T in this case, would also be more indicated.

6.4   Conclusions

In this paper, growth of simple and cost effective method of bulk MoS$_2$ sample by sintering of MoS$_2$ powder is discussed. In the preparation, we subjected the pellets to different temperatures and pressures and analyzed the IV curve with the 4-probe technique obtaining the electrical conductivity.

We show that the best results are achieved for 700 °C and 20 T.

References

1 Kumar, N., He, J., He, D., Wang, Y. & Zhao, H. Charge carrier dynamics in bulk MoS2 crystal studied by transient absorption microscopy. *Journal Of Applied Physics*. **113**, 133702 (2013) 113

2 Splendiani, A., Sun, L., Zhang, Y., Li, T., Kim, J., Chim, C., Galli, G. & Wang, F. Emerging photoluminescence in monolayer MoS2. *Nano Letters*. **10** , 1271-1275 (2010) 113

3 Mak, K., Lee, C., Hone, J., Shan, J. & Heinz, T. Atomically thin MoS2: A new direct-gap semiconductor. *Phys. Rev. Lett.* . **105** pp. 136805 (2010) 113

4 Mak, K., He, K., Shan, J. & Heinz, T. Control of valley polarization in monolayer MoS2 by optical helicity. *Nature Nanotechnology* . **7** , 494-498 (2012) 113

5 Dıez-Pérez, I., Li, Z., Guo, S., Madden, C., Huang, H., Che, Y., Yang, X., Zang, L. & Tao, N. ACS Nano 6, 7044 (2012); E. Ponomarev, I. Gutiérrez-Lezama, N. Ubrig, and AF Morpurgo. *Nano Lett* . **15** pp. 8289 (2015)

6 Li, Y., Pitaevskii, L. & Stringari, S. Quantum tricriticality and phase transitions in spin-orbit coupled Bose-Einstein condensates. *Physical Review Letters* . **108** , 225301 (2012)

7 Fortin, E. & Sears, W. Photovoltaic effect and optical absorption in MoS2. *Journal Of Physics And Chemistry Of Solids* . **43** , 881-884 (1982)

8 Tao, J., Chai, J., Guan, L., Pan, J. & Wang, S. Effect of interfacial coupling on photo-catalytic performance of large scale MoS2/TiO2 hetero-thin films. *Applied Physics Letters* . **106** , 081602 (2015)

9 Liu, G., Shan, W., Yao, Y., Yao, W. & Xiao, D. Three-band tight-binding model for monolayers of group-VIB transition metal dichalcogenides. *Physical Review B* . **88** , 085433 (2013)

10 Sallen, G., Bouet, L., Marie, X., Wang, G., Zhu, C., Han, W., Lu, Y., Tan, P., Amand, T., Liu, B. & Others Robust optical emission polarization in MoS 2 monolayers through selective valley excitation. *Physical Review B* . **86** , 081301 (2012)

11 Mukherjee, B., Guchhait, A., Chan, Y. & Simsek, E. Absorptance of PbS quantum dots thin film deposited on trilayer MoS2. *Adv. Mater. Lett* . **6** (2015)

12 Gomez, A., Poot, M., Steele, G., Zant, H. & Agraıt, N. G. 385 Rubio Bollinger. *Adv. Mater* . **24** pp. 772 (2012)

13 Bertolazzi, S., Brivio, J. & Kis, A. ACS Nano 5 (2011) 9703. *Crossref, ISI* .

14 Pandey, A., Dutta, S., Kumar, A., Raman, R., K Kapoor, A. & Muralidhran, R. Structural and optical properties of bulk MoS2 for 2D layer growth. *Advanced Materials Letters* . **7** , 777-782 (2016)

15 El Beqqali, O., Zorkani, I., Rogemond, F., Chermette, H., Chaabane, R., Gamoudi, M. & Guillaud, G. Electrical properties of molybdenum disulfide MoS2. Experimental study and density functional calculation results. *Synthetic Metals* . **90** , 165-172 (1997) 114

16 Johnson, V. & Vaughn, G. Investigation of the mechanism of MoS2 lubrication in vacuum. *Journal Of Applied Physics* . **27** , 1173-1179 (1956) 114

17 Klenke, C. Tribological performance of MoS2 B2O3 compacts. *Tribology International* . **23** , 23-26 (1990) 114

18 Tanaka, K., Uchiyama, Y., Nakagawa, T. & Matsunaga, M. Wear and frictional behaviour of MoS2 pellets and steel lubricated with MoS2 powder. *Wear* . **74** , 165-175 (1981) 114

19 Wang, Q., Kalantar-Zadeh, K., Kis, A., Coleman, J. & Strano, M. Electronics and optoelectronics of two-dimensional transition metal dichalcogenides. *Nature Nanotechnology* . **7** , 699-712 (2012) 114

20 Low, J., Cao, S., Yu, J. & Wageh, S. Two-dimensional layered composite photocatalysts. *Chemical Communications* . **50** , 10768-10777 (2014) 114

21 Yuan, Y., Lu, H., Yu, Z. & Zou, Z. Noble-metal-free molybdenum disulfide cocatalyst for photocatalytic hydrogen production. *ChemSusChem* . **8** , 4113-4127 (2015) 114

22 Ider, J., Oliveira, A. & Rubinger, R. A Robust System for Thermoelectric Device Characterization. *IEEE Transactions On Instrumentation And Measurement* . **70** pp. 1-7 (2021) 113

23 Oviedo, J., KC, S., Lu, N., Wang, J., Cho, K., Wallace, R. & Kim, M. In situ TEM characterization of shear-stress-induced interlayer sliding in the cross section view of molybdenum disulfide. *ACS Nano* . **9** , 1543-1551 (2015) 115

24 Eda, G., Yamaguchi, H., Voiry, D., Fujita, T., Chen, M. & Chhowalla, M. Photoluminescence from chemically exfoliated MoS2. *Nano Letters* . **11** , 5111-5116 (2011) 114

25 Wilson, J. & Yoffe, A. The transition metal dichalcogenides discussion and interpretation of the observed optical, electrical and structural properties. *Advances In Physics* . **18** , 193-335 (1969) 114

26 Wypych, F., Weber, T. & Prins, R. Scanning tunneling microscopic investigation of 1T-MoS2. *Chemistry Of Materials* . **10** , 723-727 (1998) 114

27 El-Mahalawy, S. & Evans, B. The thermal expansion of 2H-MoS2, 2H-MoSe2 and 2H-WSe2 between 20 and 800 C. *Journal Of Applied Crystallography* . **9** , 403-406 (1976) 114

28 Beal, A. & Hughes, H. Kramers-Kronig analysis of the reflectivity spectra of 2H-MoS2, 2H-MoSe2 and 2H-MoTe2. *Journal Of Physics C: Solid State Physics* . **12** , 881 (1979) 114

29 Strachan, J., Masters, A. & Maschmeyer, T. 3R-MoS2 in review: History, status, and outlook. *ACS Applied Energy Materials* . **4** , 7405-7418 (2021) 114

30 Mao, Y., Fang, Y., Yuan, K. & Huang, F. Effect of vanadium doping on the thermoelectric properties of MoS2. *Journal Of Alloys And Compounds* . pp. 163921 (2022) 114

114

7 Conclusions

In Chapter 2 we have built and analyzed a solar concentration for energy harvesting using TEG technology based on eight Peltier cooler modules and parabolic mirrors. Considering the best temperature gradient of 109 °C we obtained an efficiency of 6.20% as the thermodynamic limit for direct conversion from heat to electric power. The computational method applied to the analysis of three simultaneous equations obtained excellent performance.

In Chapter 3 we have analyzed a CSP using another computational method, CE. The method performed well. The computational time spent to solve the problem was less than that spent by the Genetic Algorithm and considering the best temperature gradient of 109° C we obtained the same efficiency of 6.20%.

In Chapter 4, with the aim of studying the electrical behavior of TEG we develop a new methodology for analyzing thermoelectric generating devices with a new experimental arrangement, which generates and controls temperature gradients with precision, measures such temperatures, and also allow the precise determination of relevant associated electrical quantities. Together with this new experimental arrangement, we applied a method of data analysis through a GA of differential evolution for the first time, which presented excellent results and shows a new powerful tool for the analysis of thermoelectric materials behaved reliably, presenting a good thermal efficiency, from 2.97 % to a temperature gradient of 90 °C.

In Chapter 5 we have developed a single device capable of performing the three measurements necessary for thermoelectric characterization of materials. The presented equipment was designed to performed accurate temperature control leading to stable measurements. The values of electrical resistivity, Seebeck coefficient, thermal conductivity obtained by our robust thermoelectric characterization system will contribute to improve the access to the determination of the Figure of Merit in a simple, fast and reliable form, which will contribute for research on the characterization of thermoelectric materials.

In Chapter 6 we prepare pellets using MoS_2 powder and are performing thermoelectric characterization using our equipment. The data will be treated using GA and CE.

In future works we will perform the growth of thin films of MoS_2 for thermoelectric characterization. The technique applied will be CVD. The application oven has already been developed in the laboratory and the samples are in the preparation phase.

Annex

ANNEX A – Software Registration Certificate

REPÚBLICA FEDERATIVA DO BRASIL
MINISTÉRIO DA ECONOMIA
INSTITUTO NACIONAL DA PROPRIEDADE INDUSTRIAL
DIRETORIA DE PATENTES, PROGRAMAS DE COMPUTADOR E TOPOGRAFIAS DE CIRCUITOS INTEGRADOS

Certificado de Registro de Programa de Computador

Processo Nº: **BR512021001582-7**

O Instituto Nacional da Propriedade Industrial expede o presente certificado de registro de programa de computador, válido por 50 anos a partir de 1° de janeiro subsequente à data de 13/07/2021, em conformidade com o §2°, art. 2° da Lei 9.609, de 19 de Fevereiro de 1998.

Título: Self-Adaptative Differential Evolution method applied to the characterization of thermoelectric devices

Data de publicação: 13/07/2021

Data de criação: 13/05/2021

Titular(es): UNIFEI - UNIVERSIDADE FEDERAL DE ITAJUBÁ

Autor(es): RERO MARQUES RUBINGER; ADHIMAR FLAVIO OLIVEIRA; JOAO IDER SILVA JUNIOR; DAVI MARCELO FEBBA

Linguagem: PYTHON

Campo de aplicação: EN-04

Tipo de programa: SM-01

Algoritmo hash: SHA-256

Resumo digital hash: F9605A9770658A6C8D0351FEE35195F6D82743CBBCB8D27EC9352D1FD7071D46

Expedido em: 20/07/2021

Aprovado por:
Joelson Gomes Pequeno
Chefe Substituto da DIPTO - PORTARIA/INPI/DIRPA Nº 02, DE 10 DE FEVEREIRO DE 2021

Figure 24 – Software Registration Certificate.

ANNEX B – Software Registration Certificate

REPÚBLICA FEDERATIVA DO BRASIL
MINISTÉRIO DA ECONOMIA
INSTITUTO NACIONAL DA PROPRIEDADE INDUSTRIAL
DIRETORIA DE PATENTES, PROGRAMAS DE COMPUTADOR E TOPOGRAFIAS DE CIRCUITOS INTEGRADOS

Certificado de Registro de Programa de Computador

Processo Nº: **BR512021000737-9**

O Instituto Nacional da Propriedade Industrial expede o presente certificado de registro de programa de computador, válido por 50 anos a partir de 1° de janeiro subsequente à data de 12/04/2021, em conformidade com o §2°, art. 2° da Lei 9.609, de 19 de Fevereiro de 1998.

Título: Determinação da Figura de Mérito de Dispositivos Termoelétricos

Data de publicação: 12/04/2021

Data de criação: 12/02/2021

Titular(es): UNIFEI - UNIVERSIDADE FEDERAL DE ITAJUBÁ

Autor(es): ADHIMAR FLÁVIO OLIVEIRA; RERO MARQUES RUBINGER; JOÃO IDER SILVA JÚNIOR

Linguagem: PYTHON

Campo de aplicação: EN-04

Tipo de programa: IT-02

Algoritmo hash: SHA-256

Resumo digital hash: 9165863781E693D7F756588599BED91A01D60C8F102104A23A5C89A86E2128CD

Expedido em: 20/04/2021

Aprovado por:
Carlos Alexandre Fernandes Silva
Chefe da DIPTO

Figure 25 – Software Registration Certificate.

ANNEX C – Characterization system patent for generation devices thermoelectric

Figure 26 – Characterization system patent for generation devices thermoelectric.

ANNEX D – Investigation of electronic transport in InAs/GaAs samples. A study using the metaheuristic self-adaptive differential evolution method

Investigation of electronic transport in InAs/GaAs samples. A study using the metaheuristic self-adaptive differential evolution method

Luiz Henrique Ribeiro [a], João Ider [a], Adhimar Flávio Oliveira [a] ✉, Rero Marques Rubinger [a], Carla Patrícia Lacerda Rubinger [a], Alfredo Gontijo de Oliveira [b]

[a] Universidade Federal de Itajuba, Av BPS, 1303, Pinheirinho, Itajubá, MG 37500-903, Brazil
[b] Universidade Federal de Minas Gerais, Av. Pres. Antônio Carlos, 662, Pampulha, Belo Horizonte, MG 31270-901, Brazil

Figure 27 – Investigation of electronic transport in InAs/GaAs samples. A study using the metaheuristic self-adaptive differential evolution method.

ANNEX E – Preparation and characterization of thermoelectric materials

Figure 28 – Preparation and characterization of thermoelectric materials.

ANNEX F – Concentrating Solar Power (CSP). An approach using Genetic Algorithms and Cross Entropy

Ministério da Educação
Universidade Federal de Itajubá – UNIFEI
Instituto de Física & Química
Curso de Física Bacharelado

CERTIFICADO DE EXTENSÃO UNIVERSITÁRIA

Certifico que **João Ider Silva Júnior**, doutorando do curso de Materiais para Engenharia, da Universidade Federal de Itajubá (UNIFEI), **ministrou o seminário "*Concentrador Solar de Potência (CSP). Uma abordagem utilizando Algoritmo Genético e Entropia Cruzada*"**, para alunos de graduação dos cursos de Física (bacharelado e licenciatura), do Instituto de Física & Química da Universidade Federal de Itajubá (UNIFEI), no dia 26 de Abril de 2022, **com duração de 2 horas**.

Prof. Dr. Gabriel Rodrigues Hickel
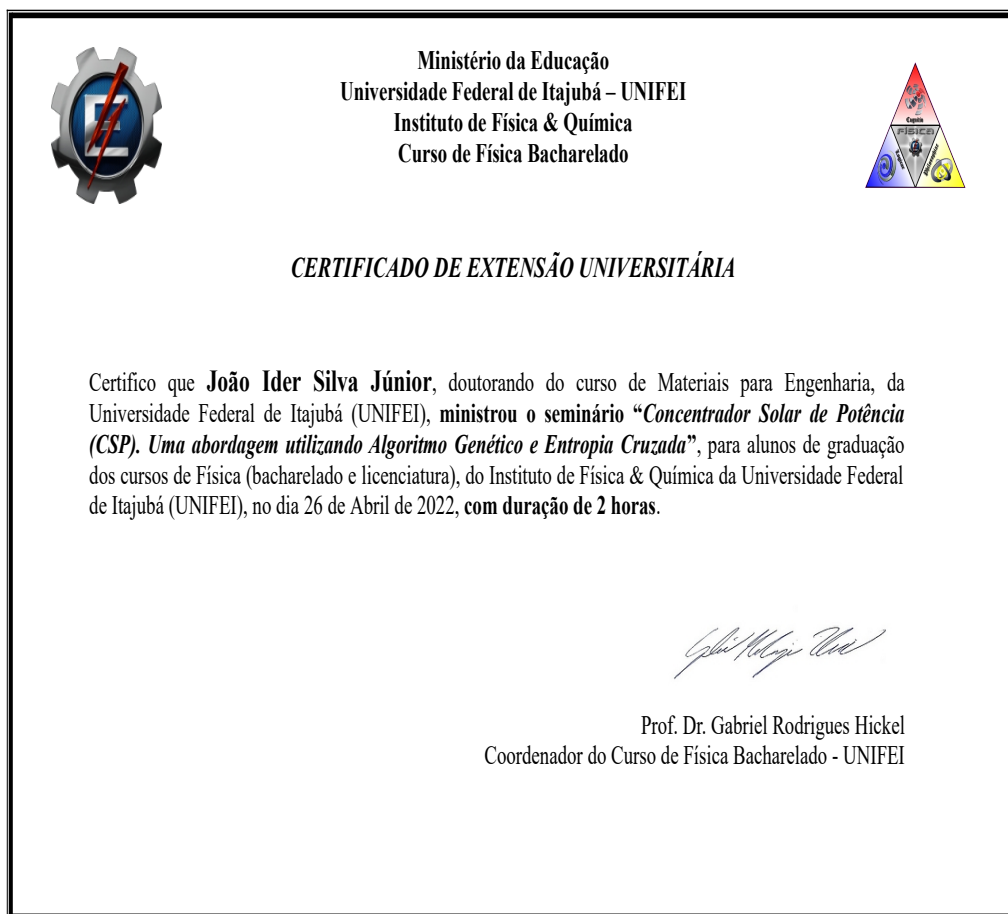Coordenador do Curso de Física Bacharelado - UNIFEI

Figure 29 – Concentrating Solar Power (CSP). An approach using Genetic Algorithms and Cross Entropy.

ANNEX G – A robust system for thermoelectric device characterization

Figure 30 – A robust system for thermoelectric device characterization.